

**Carnegie Mellon University**  
**MELLON COLLEGE OF SCIENCE**

**THESIS**

SUBMITTED IN PARTIAL FULFILLMENT OF THE REQUIREMENTS  
FOR THE DEGREE OF

**DOCTOR OF PHILOSOPHY IN THE FIELD OF PHYSICS**

TITLE: "First principles and Wannier functions based study of two-dimensional  
electronic systems."

PRESENTED BY: Nikhil Sivadas

ACCEPTED BY THE DEPARTMENT OF PHYSICS

DI XIAO 8/25/16  
\_\_\_\_\_  
DI XIAO, CHAIR PROFESSOR DATE

STEPHEN GAROFF 8/25/16  
\_\_\_\_\_  
STEPHEN GAROFF, DEPT HEAD DATE

APPROVED BY THE COLLEGE COUNCIL

REBECCA DOERGE 8/25/16  
\_\_\_\_\_  
REBECCA DOERGE DATE

# First-principles and Wannier-function-based study of two-dimensional electronic systems

by

Nikhil Sivadas

Submitted in partial fulfillment of the  
requirements for the degree of  
Doctor of Philosophy  
at  
Carnegie Mellon University  
Department of Physics  
Pittsburgh, Pennsylvania

Advised by Professor Di Xiao

August 18, 2016



## Abstract

One of the goals in making better devices is to achieve the desired functionality in materials that enable a given application. The strong link between the functional behavior and the physical properties of materials is key to making better devices. This thesis focuses on applications of density functional theory (DFT), a powerful computational tool, for understanding the electronic, magnetic, magneto-optic, topological and thermodynamic properties of two-dimensional electronic systems (2DES). Why are 2DES interesting? Firstly, the reduced dimensionality renders these materials with properties which could be absent in the bulk form. Secondly, from a technological point of view, the desired functionality can be easily controlled externally in these 2DES by the application of a gate voltage or strain. The 2DES considered here could be crucial in beyond-CMOS electronic technologies. The materials considered in this thesis can be broadly categorized into two different classes of systems. The first one is the two-dimensional electron gas observed at the complex oxide interfaces. The discussion will go into the details of the formation of 2DEG in oxides resulting both from polar catastrophe and also due to the presence of vacancies. The second class of materials is two-dimensional (2D) atomic crystals, more specifically, 2D magnets. We not only predict a class of compounds, transition metal trichalcogenides (TMTC), that can exhibit magnetism in the 2D limit, but also demonstrate control of these magnetic degrees of freedom. Finally, we also demonstrate both using symmetry based tight-binding models and first-principles calculations a new way to detect magnetism in the 2D limit, which is applicable to compounds other than TMTC as well.



## Acknowledgments

First and foremost, I would like to express my profound gratitude to my advisor Prof. Di Xiao for his guidance throughout my Ph.D. I have never walked out of his room without learning something new, both from a professional and a personal point of view. He always took an active interest in me life, outside the lab. It is not a hyperbole to say that he has been an integral part of everything good that happened to me in the last 4 years. For that, I thank him sincerely. And, whenever things did go bad, he was always there beside me supporting me. I feel lucky to have him as my advisor. I do not think a simple thank you would do justice to everything he has done for me. Yet, Thank you!

I would like to thank Dr. Satoshi Okamoto for the guidance in various projects. I learnt exchange interactions from him, which was very useful in understanding magnetism in materials. He always had valuable suggestions on how to approach problems that I found very useful. I also would like to thank Prof. Randall Feenstra for mentoring me in the STO (001) project. I learnt a lot about experiments in general, and scanning tunneling spectroscopy in specific from my discussions with him. His guidance was vital in helping me understand configurational coordinate diagrams, and his feedback was crucial in calculating the formation energy of vacancies. I am grateful for his help and guidance.

I also want to thank Dr. Valentino R. Cooper firstly, for providing the computing time that made most of the calculations feasible. I would also like to thank him for inviting me to ORNL as an ASTRO researcher. It was my first exposure to research in a large-scale collaborative environment. What I gained in experience was invaluable. I am also immensely grateful for his guidance during my first project. He was very patient with me and gave clear explanations that laid the foundation for my continued interest in DFT.

On that note, I want to thank Prof. Doron Naveh for introducing me to DFT. I am also grateful to Prof. Wenguang Zhu for all the discussion and guidance. I also want to thank him for sharing some of his scripts with me that made visualizing data easier. Special thanks to Prof. Marek Skowronski, Prof. Michael Widom, Prof. Benjamin Hunt and Prof. Elias Towe for their advice and guidance. I want to also thank Hua Chen, Wenyu Shan, Wattaka Sitaputra, Xiaochuan Wu, Xiaou Zhang, Matthew Daniels, Ran Cheng Jianhui Zhu and Ananth Tenneti for the interesting discussions, and their company.

Finally, I want to thank my parents, my family, and my friends who have always been there for me. Overall, I feel blessed to have people around me who have my best interests in their heart.

# Contents

<b>1</b>	<b>Introduction</b>	<b>1</b>
1.1	Materials and devices . . . . .	1
1.2	Two-dimensional electronic systems . . . . .	2
1.3	Structure of the thesis . . . . .	3
<b>2</b>	<b>Modeling electronic structure: Density Functional Theory</b>	<b>5</b>
2.1	Background . . . . .	5
2.2	Schrödinger equation . . . . .	5
2.3	Hohenberg-Kohn theorem . . . . .	7
2.3.1	Theorem 1 . . . . .	7
2.3.2	Theorem 2 . . . . .	8
2.4	Kohn-Sham auxiliary system . . . . .	8
2.5	Exchange and Correlation Energy . . . . .	9
<b>3</b>	<b>Thickness Dependent Carrier Density at the Surface of SrTiO<sub>3</sub> (111) Slabs</b>	<b>11</b>
3.1	Introduction . . . . .	11
3.2	Methodology . . . . .	13
3.3	Electronic structure . . . . .	14
3.3.1	Ti-termination . . . . .	14
3.3.2	TiO-termination . . . . .	18
3.4	Thermodynamic stability . . . . .	21
3.5	Summary . . . . .	24
<b>4</b>	<b>Oxygen Vacancies on SrTiO<sub>3</sub> (001) surfaces</b>	<b>25</b>
4.1	Introduction . . . . .	25
4.2	Methodology . . . . .	26
4.3	Results and discussion . . . . .	31
4.3.1	Formation energy and defect wavefunction . . . . .	31
4.3.2	Configurational Coordinate diagram and vibronic coupling . . . . .	33
4.4	Summary . . . . .	33

<b>5</b>	<b>Transition metal trichalcogenides for 2D magnets</b>	<b>36</b>
5.1	Introduction . . . . .	36
5.2	Crystal and Magnetic Structure . . . . .	37
5.3	Results and discussion . . . . .	41
5.3.1	Computation details . . . . .	41
5.3.2	Exchange interactions . . . . .	41
5.3.3	Effect of strain . . . . .	46
5.3.4	Bulk magnetic order . . . . .	46
5.4	Summary . . . . .	47
<b>6</b>	<b>Magneto-optic effects in 2D magnets</b>	<b>48</b>
6.1	Introduction . . . . .	48
6.2	Results and discussion . . . . .	49
6.2.1	Symmetries . . . . .	49
6.2.2	Tightbinding model . . . . .	49
6.2.3	Gate-controllable MOKE . . . . .	52
6.3	Summary . . . . .	58
<b>7</b>	<b>Summary and Outlook</b>	<b>59</b>
7.1	Summary . . . . .	59
7.2	Outlook . . . . .	60
	<b>Appendices</b>	<b>63</b>
<b>A</b>	<b>Magneto-optic effects</b>	<b>64</b>
A.1	Derivation of MOKE angle for 2D materials . . . . .	64

# List of Tables

3.1	The unrelaxed cleavage energy, relaxation energy and surface energy in $\text{J}/\text{m}^2$ for different terminations. . . . .	22
5.1	Lattice constant $a$ , magnetic ground state (GS), exchange coupling constants, and magnetic critical temperature for $ABX_3$ studied. Critical temperatures are obtained from classical Monte Carlo simulations.	42

# List of Figures

3.1	Schematic of charge density ( $\rho$ ), electric field ( $E$ ), and electrostatic potential ( $V$ ) profiles for the Ti-terminated STO (111) slabs with (a) charge uncompensated ideal atomic coordinates, (b) charge uncompensated relaxed atomic coordinates, (c) charge compensated ideal atomic coordinates and (d) charge compensated relaxed atomic coordinates. For the relaxed atomic coordinates (b) and (d), the SrO <sub>3</sub> layer (green block) splits into Sr (green line) and O <sub>3</sub> (violet line) layers. $Z$ is the magnitude of the effective charge of each layer. Both polar distortions (b) and charge compensation due to electronic reconstruction (c) can help reduce the divergent electrostatic potential, and the net effect is less than $Ze/2$ electrons transferred between the surfaces (d). . . . .	12
3.2	Layer-by-layer structure of the $n=6$ STO (111) slab. (a) Top and (b) side view of the Ti-terminated STO (111) slab. (c) Top and (d) side view of the TiO-terminated STO (111) surface. Green, Blue and Black represent Sr, Ti and O ions, respectively. The five possibilities for placing the extra O atom on the Ti termination are also labeled in (c), and the energetically favorable position is marked by Red in both (c) and (d). . . . .	15
3.3	(a) Layer-dependent DOS and (b) the electronic band structure for the Ti-terminated STO (111) slab with 6 layers. There are two bands crossing the Fermi level; the top layer conduction band (green) consists mainly of Ti $d$ states, and the bottom layer valence band (red) consists mainly of O $p$ states. . . . .	16
3.4	The total charge transferred between the surfaces as a function of thickness for relaxed (red) and unrelaxed (black) system. . . . .	17
3.5	Polar distortions for the Ti-terminated STO (111) slab for layer thickness $n = 6, 9$ and $12$ , relative to the SrO <sub>3</sub> bottom layer. (a) Split between Sr and O <sub>3</sub> in SrO <sub>3</sub> layers. (b) Off-centering of Ti relative to planes of O anions above and below Ti. Surface Ti off-centering is computed relative to bulk positions. (c) A schematic of the effect of relaxation for the case of Ti-termination with 6 layers of STO. . . . .	19
3.6	The total DOS for 6 layers of the TiO-terminated STO (111) slab. . .	20

3.7	Polar distortions for the TiO-terminated STO (111) slab for layer thickness $n = 6, 9$ and $12$ , relative to the SrO <sub>2</sub> bottom layer. (top) Split between Sr and O <sub>3</sub> in SrO <sub>3</sub> layers. (bottom) Off-centering of Ti relative to planes of O anions above and below Ti. . . . .	20
3.8	Stability diagram of the STO (111) surface. The most stable termination is shown as a function of the chemical potential of O and Sr. . . . .	23
4.1	The average conductance spectra on SrO-terminated cleaved SrTiO <sub>3</sub> acquired (a) before and (b) after segregation of surface oxygen vacancies by moderate-temperature annealing. (c) Comparison between conductance spectra from the annealed SrO-terminated surfaces before (red) and after 10 L of molecular oxygen exposure (green). The sample voltage corresponds to the energy of a state relative to the Fermi level (0 V in the spectra). . . . .	26
4.2	(a) The top view and (b) the side view of SrO-terminated SrTiO <sub>3</sub> surface with an oxygen vacancy (open red circle). A vacuum region more than 15 Å was used. . . . .	27
4.3	The formation energy as a function of Fermi level for different charge configurations for the oxygen vacancy in (a) the bulk, (b) the surface SrO layer, and (c) the surface TiO <sub>2</sub> layer. Insets show the resulting transition levels (Fermi level position at which transitions between charge states occur). For panel (c), the transition between +1 and 0 charge states occurs at a Fermi level position slightly above the CB minimum. . . . .	30
4.4	The majority spin density for the $V_O^0$ , $V_O^{+1}$ and $V_O^{+2}$ in the SrO and TiO <sub>2</sub> surface layer. The isosurfaces (yellow lobes) correspond to 2% of the maximum value in each plot. Green, blue and red balls represent Sr, Ti and O atoms, respectively. Square solid box represents position of the oxygen vacancy. . . . .	32
4.5	Configuration coordinate diagram for the SrO termination for $V_O^0$ and $V_O^{+1}$ for a Fermi energy of (a) 2.3 eV and (b) 2.5 eV. A schematic of the absolute square of harmonic oscillator wavefunctions are shown for both the neutral and + charge states of the vacancy. . . . .	34
5.1	Crystal and magnetic structure of transition metal trichalcogenides $ABX_3$ . The crystal structure (a) and the top view (b) of monolayers of $ABX_3$ . The transition metal $A$ atoms form a honeycomb structure with $B_2X_6$ ligand occupying the interior of the honeycomb. Top view of the different spin configurations: the FM ordered (c), AF-Néel ordered (d), AF-zigzag ordered (e), AF-stripy ordered (f), with only the transition metal ions shown. Up (down) spins are represented by black filled-in (open) circles. The crystal structure is drawn using VESTA [1] . . . .	38

5.2	The ground state magnetic phase diagram for our spin model as a function of $J_1/J_3$ and $J_2/J_3$ . Since our calculation finds $J_3$ to be always AF, only $J_3 > 0$ is considered. Spins are treated as classical degrees of freedom. All compounds studied are located at corresponding parameter values. Open symbols are positions under tensile strains with arrows indicating the change from the unstrained cases. . . . .	39
5.3	The partial density of states (PDOS) of the ground states of $\text{CrSiTe}_3$ (AF-zigzag), $\text{CrGeTe}_3$ (FM) and $\text{MnPS}_3$ (AF-Néel) are shown in (a), (b) and (c) respectively. These are the three unique ground states exhibited by the $ABX_3$ compounds. The PDOS of $A$ , $B$ and $X$ are shown using red lines, broken green lines and dotted blue lines respectively. We observe considerable hybridization between the transition metal ( $A$ ) atoms and the chalcogen ( $X$ ) atoms. . . . .	40
5.4	Top view of monolayer of $ABX_3$ . Blue, violet and yellow represents $A$ , $B$ and $X$ ions respectively. The five possible paths for second NN interaction is show in (a) and the third NN interaction is shown in (b). The two different NN hopping paths between two transition metal atoms at different sites ( $A_1$ and $A_2$ ) are shown in (c) with the direct exchange as a hopping between the transition metal orbitals and the superexchange interaction characterized by hopping between the transition metals through the $X$ atom. . . . .	43
5.5	Main contributions of virtual electron excitations to magnetic interactions. Virtual electron excitations from two $X$ anions to a pair of (a) second NN and (b) third NN $A$ ions. (c) Direct excitations between neighboring TM ions (red dots), resulting in AF $J_1$ . (d) Excitations from two orthogonal orbitals on a $X$ anion (black dots) to a neighboring pair of $A$ ions. Because of the Hund coupling acting in excited states as indicated by a broken circle, this process gives rise to FM $J_1$ . The actual sign of exchange interactions results from the competition between FM and AF contributions for $J_1$ . Numbers indicate the typical order of the first half perturbation processes for each contribution. . . . .	44

6.1	(a) Schematic of a honeycomb lattice with collinear Néel order. Up (down) spins are represented by filled (open) circles. The system possesses combined $\mathcal{TI}$ symmetry although both $\mathcal{T}$ and $\mathcal{I}$ symmetries are individually broken. (b) and (c) Energy bands of the tight-binding model with broken mirror symmetry ( $\lambda_R = 0.05t$ , $\lambda_V = 0$ ) and broken in-plane inversion symmetry ( $\lambda_R = 0$ , $\lambda_V = 0.05t$ ), respectively. In both cases, $\lambda_{SO} = 0.06t$ and $\lambda_M = 0.7t$ . The spin degeneracy of the bands is lifted in both cases. (d) The imaginary part of the optical Hall conductivity ( $\sigma''_{xy}$ ) computed for $\lambda_R = 0.05t$ (black), $\lambda_V = 0.05t$ (red) and $\lambda_V = -0.05t$ (blue). $\sigma''_{xy}$ is zero when only $\lambda_R$ is turned on and becomes non-zero when $\lambda_V \neq 0$ . As the sign of $\lambda_V$ is reversed so is $\sigma''_{xy}$ . The smearing parameter was set to $0.1t$ . . . . .	50
6.2	(a) The crystal structure of monolayers of MnPSe <sub>3</sub> . The transition metal Mn atoms form a honeycomb structure with P <sub>2</sub> Se <sub>6</sub> ligand occupying the center of the honeycomb. (b) The side view of the crystal structure of bilayer MnPSe <sub>3</sub> . The crystal structure is drawn using VESTA [1]. (c) The band structure of the bilayer MnPSe <sub>3</sub> in the absence of an electric field. The insert shows the Mn atoms in the bilayer. (d) The band structure of the bilayer MnPSe <sub>3</sub> in the presence of an electric field (0.4 V/nm) along the $z$ -direction. The insert shows the lifting of the spin degeneracy of the bands due to the $\mathcal{TI}$ symmetry breaking by the field. . . . .	53
6.3	(a) The real part of $\sigma_{xy}$ , (b) the imaginary part of $\sigma_{xy}$ , and (c) the real part of $\sigma_{xx}$ of bilayer MnPSe <sub>3</sub> at zero field (black) and a field with strength 0.4 V/nm (red). The smearing parameter was set to 0.2 eV. The corresponding (d) Kerr rotation angle and (e) ellipticity angle computed as a function of photon energy $\hbar\omega$ for bilayer MnPSe <sub>3</sub> on a wedged SiO <sub>2</sub> substrate. The zero point of the energy corresponds to the top of valence band. (f) A schematic of a magneto-optic device made from layered antiferromagnets. S, D, and G stand for source, drain and gate respectively. In the incident and the reflected light, an arrow shows the direction of the polarization direction. On reflection from the antiferromagnets, the plane of polarization of light can be rotated (from green to red arrow), and an ellipticity is induced, depending on the gate voltages. . . . .	54
6.4	$\sigma'_{xy}$ for monolayer (black) and bilayer (red) MnPSe <sub>3</sub> under an electric field of 0.4 V/nm. The electric field is ineffective in breaking the $\mathcal{TI}$ symmetry for monolayer MnPSe <sub>3</sub> . . . . .	57
7.1	2D lego blocks as proposed by Geim <i>et al.</i> [2], now modified to include 2D magnet lego blocks. . . . .	62

A.1 A schematic of the MOKE setup. Assuming perpendicular incidence of a monochromatic light, we have an incident beam, a reflected beam and a transmitted beam. The thin sample (orange) of thickness  $d$  is kept on an infinite substrate (grey) labeled as  $II$ , which has a refractive index  $n$ . The air-sample is taken as  $z = 0$ . . . . .

# Chapter 1

## Introduction

### 1.1 Materials and devices

Manipulating material properties to suit a variety of needs has been one of the cornerstones of human civilization. In fact, the history of the earth can be tracked by tracking the evolution of materials. For example, the Stone-Age culture was characterized by the use of rocks that were locally available. The innovation of smelting and casting metals in the Bronze Age introduced the idea of reshaping native metals both for tools and weapons. 4<sup>th</sup> millennium BC marked the first production of alloy bronze. Through each small step, the world has evolved into its shape we see today. Of them, one step of immense significance came with the formulation of quantum mechanics. Soon, quantum mechanics was applied to understand atoms at first, and later to understand crystalline compounds. The understanding of the electronic properties of rigid matter, or solids, directly led to the development of the transistors in 1947 [3, 4]. Soon, the junction transistor replaced vacuum tubes, and eventually spawned the microchip revolution. 1953 marked the first successful attempt in using Silicon as transistor material by Morris Tanenbaum at Bell Laboratories. Since then, Silicon has dominated the market of semiconductor industry. It would not be a hyperbole to call the period we live in as the Silicon Age.

In 1965, Gordon E. Moore, the co-founder of Intel, was asked to predict what was going to happen in the semiconductor components industry over the next ten years. His answer was that the number of transistors in a dense integrated circuit would double approximately every two years. Although this prediction was meant for a decade, it proved to be accurate for over 45 years, giving it the name “Moore’s law”. But, Moore’s law has already started to fail. With the size of the device becoming smaller and smaller, and approaching quantum regime, new problems, such as, tunneling effects need to be addressed. Therefore, both researchers and manufacturers are on the constant lookout for new materials that can tackle these issues, thereby providing improved device functionality.

## 1.2 Two-dimensional electronic systems

In this thesis, I have focused on first-principles studies of two-dimensional electronic systems (2DES) within density functional theory. Why are 2DES interesting? For starters, the ultimate confinement of electron motion in the vertical direction often leads to spectacular quantum phenomena. In fact, some phenomena, such as the quantum Hall effect, are absent in higher dimensions. Furthermore, from a technological point of view, 2DES are interesting because their physical properties can be easily tuned by external controls. As such, it is widely believed that novel 2DES will play a central role in post-Silicon FinFET technologies.

This thesis will cover my research in two different 2DES. The first one is the two-dimensional electron gas (2DEG) experimentally observed at the complex oxide interfaces. Since the initial discovery of a 2DEG at the  $\text{LaAlO}_3/\text{SrTiO}_3$  interface [5, 6], oxide heterostructures have attracted a lot of attention in the rapidly growing field of oxide electronics. The initial interest was primarily because both  $\text{LaAlO}_3$  and  $\text{SrTiO}_3$  are wide-band gap semiconductors with a band gap of 5.6 eV and 3.2 eV, respectively. It was fascinating to see that on epitaxial growth of these bulk-insulating heterostructures, the interface could become conducting. In fact, the carrier densities reported were high, reaching  $\sim 3 \times 10^{14} / \text{cm}^2$  [7], with mobilities as high as  $10^4 \text{ cm}^2/(\text{V}\cdot\text{s})$  [5]. Later, this 2DEG was also found to host a wide variety of electronic phenomena, including superconductivity [8], magnetism [9], and Rashba spin-orbit coupling [10, 11]. These phenomena, together with the demonstrated tunability of interface conductivity through electric [12, 13], chemical and photosensitive means [14], offer promising potential for device applications with novel functionality [15, 16]. But to understand these fascinating phenomena and to fully explore the application potential of oxide heterostructures, it is imperative to understand the nature and the origin of this 2DEG.

There has been a lot of debate on the various mechanisms responsible for the formation of this 2DEG. A leading interpretation for this interfacial conductivity is based on the polar catastrophe mechanism [5, 6]. A second mechanism involves vacancy formation of donor-type defects. In this regard, oxygen vacancies are most commonly studied [17–19]. In the case of heterostructures, atomic intermixing at the interface between materials has also been suggested as a possible source of these high-density electrons [20, 21]. Other mechanisms include surface adsorbates and atomic reconstruction. This thesis will focus on the electronic reconstruction resulting from a polar instability, and autoionization of the oxygen vacancy. Identifying the underlying mechanisms will give us more control in tuning this high-density 2DEG.

The second class of 2DES discussed here is two-dimensional (2D) atomic crystals. These are made from layered materials by exfoliation, and are only one or a few atomic layers thick. Recent years have seen a surge of interest in 2D crystals due to their highly tunable physical properties [22–26]. The ultra-thin nature of these materials has been exploited in the field of flexible, thin and scalable electronics [27, 28]. But

what makes these materials even more interesting is the ease in which one can control various optical, electronic and topological properties through external means, for example, by gating or by applying strain [29–35].

The family of 2D crystals has grown considerably since the initial discovery of graphene, with new additions such as boron nitride and transition metal dichalcogenides. The emergence of transition metal compounds in the landscape of 2D crystals is particularly advantageous as it opens the door to many physical properties not available in graphene [2, 36–39]. For example, in monolayer MoS<sub>2</sub> the large spin-orbit interaction leads to a unique spin-valley coupling which might be useful for spintronic applications [40–44]. Geim *et al.* [2] proposed the idea of thinking of each of these 2D materials as a lego block, and by stacking different lego blocks on top of each other, one can either enhance already existing properties or produce new properties absent in the individual lego units. But one ‘lego block’ that is still missing in the current line-up of 2D materials is the spin-lego block, i.e. 2D magnets. Once we have 2D magnets, we can control the time-reversal symmetry-breaking in these other lego blocks by integrating 2D magnets into the heterostructure. Hence, finding good 2D magnetic semiconducting materials are imperative for the advancement of 2D spintronics.

### 1.3 Structure of the thesis

This thesis contains 7 chapters. After giving a brief introduction to density functional theory in chapter 2, I will discuss 2DEG in transition metal oxides in chapter 3 and 4. By studying SrTiO<sub>3</sub> without any overlayer, we can study the contributions of electronic reconstruction and also oxygen vacancies, in the formation of 2DEG. In an attempt to understand the polarization effects, we investigated the surface electronic structure of STO (111) slabs using first-principles methods [45]. We predicted the existence of the 2DEG on the (111) surface and elucidated the important role of polar distortion in its formation. It turns out that the existence of the 2DEG results from a delicate balance between local chemistry and lattice charge screening. This is discussed in chapter 3.

Chapter 4 will discuss oxygen vacancies as another source of conducting electrons [46]. Using experimental inputs from scanning tunneling microscopy (STM), we have identified characteristic peaks associated with these vacancies, which are explained based on formation energy calculations. The developed theory based on the symmetry of the wavefunction of the vacancy states not only explained the observed STM spectrum but also fits well within the findings of other experiments.

Chapters 5 and 6 will discuss magnetism in the two-dimensional limit. Two questions immediately come to mind. Is it possible to make 2D magnetic semiconductors? And how can we control the magnetism? To address the first question, we have studied transition metal trichalcogenides (TMTC), which will be discussed in chapter 5. These compounds are magnetic in their bulk form. It was recently shown that they

could be chemically exfoliated into single layers. Therefore, they make ideal candidates to potentially host 2D magnetism. Interestingly, we found that in the single layer limit not only does the magnetism survive, but it also becomes stronger [47]. By using first-principles calculations together with statistical mechanical models, we were able to understand the origin of the underlying magnetic exchange interactions and the magnetic phase diagram of these materials. From the insight we obtained, We showed that the magnetic ground state could be tuned by the application of an experimentally realizable strain. Some of our findings were corroborated through a series of experiments that followed.

Are these 2D magnets useful? Recently, we demonstrated gate-controllable magneto-optical (MO) effects in layered antiferromagnets (AFM) [48], which are discussed in chapter 6. Even though MO effects are traditionally associated with ferromagnets (FM), via a thorough symmetry analysis, we showed that the MO effects could also exist in AFM. The key idea is that in AFM, the MO effects are controlled not only by the magnetic order but also by crystal symmetry. By breaking the inversion symmetry, one can turn on the MO effects. To verify this idea, I performed first-principles calculations for realistic materials and found that in bilayer  $\text{MnPSe}_3$ , an Néel AFM, the gate controlled MO effects can be as large as that in conventional itinerant FM, such as Fe and Co. The appearance of magneto-optic effects in AFM is of intrinsic interest since it would allow direct detection of the magnetic order, and therefore, could be useful for antiferromagnets-based memory devices. Finally, I will summarize my finding and comment about what the future holds in chapter 7.

# Chapter 2

## Modeling electronic structure: Density Functional Theory

### 2.1 Background

Electrons form the “quantum glue” that holds together the nuclei in matter [49]. Understanding material behavior heavily relies on the understanding of its electronic structure. Often, the first step in understanding the electronic properties of a material is by calculating its band structure. This relies on computing efficiently the energy of each band in the material in the reciprocal space, which hinges invariably on solving a “Schrödinger-like equation”. Depending on the material properties of interest and scalability, this can be done with different complexity. In this chapter, I will discuss density functional theory (DFT), one of the most popular and versatile tools used for this purpose. The basic idea of DFT is to regard the total particle density as the primary quantity from which properties of the system can be calculated.

### 2.2 Schrödinger equation

The starting point for calculating the energies of multi-electron systems in different external potentials is the time independent Schrödinger equation, which is the eigenvalue equation for the energy operator. For electrons in a solid the Schrödinger equation can be written in terms of the many-body wavefunction  $\psi$  as

$$\hat{H}\psi = E\psi \tag{2.1}$$

where  $E$  the energy of the system and  $\hat{H}$  the Hamiltonian of the system. The Hamiltonian is made up of five parts: the kinetic energy of the nuclei ( $T_N$ ), the kinetic

---

The field of density functional theory is vast and well developed. The following discussion is only a brief overview of the basic ideas behind the methodology. For a more detailed treatment I refer the reader to excellent textbooks Ref. [49, 50].

energy of the electrons ( $T_e$ ), the internal repulsive potential energy between the different electrons ( $V_{ee}$ ), the external potential energy of the electrons-nuclei interaction ( $V_{eN}$ ) and the potential energy of the nuclei-nuclei interaction ( $V_{NN}$ ). These different terms can be written explicitly as:

$$\begin{aligned}
T_N &= - \sum_{i=1}^N \frac{\hbar^2 \nabla_{\mathbf{R}_i}^2}{2M_i}, \\
T_e &= - \sum_{j=1}^{N_e} \frac{\hbar^2 \nabla_{\mathbf{r}_j}^2}{2m_j}, \\
V_{ee} &= \sum_{i<j}^{N_e} \sum_j^{N_e} \frac{e^2}{|\mathbf{r}_i - \mathbf{r}_j|}, \\
V_{eN} &= - \sum_i^N \sum_j^{N_e} \frac{Z_i e^2}{|\mathbf{R}_i - \mathbf{r}_j|}, \\
V_{NN} &= - \sum_{i<j}^N \sum_j^N \frac{Z_i Z_j e^2}{|\mathbf{R}_i - \mathbf{R}_j|},
\end{aligned} \tag{2.2}$$

where  $\nabla_{\mathbf{R}_i}^2$  is the Laplacian operator on the  $i^{th}$  nucleus at  $\mathbf{R}_i$ , which has mass  $M_i$  and a nuclear charge  $Z_i$ ,  $N$  the total number of nuclei,  $N_e$  the total number of electrons and  $\nabla_{\mathbf{r}_i}^2$  is the Laplacian operator on the  $i^{th}$  electron at  $\mathbf{r}_i$ . Since the mass of the nucleus is much larger than that of the mass of the electron, we can approximate that the nucleus is stationary when solving for the electronic motion. This is called the Born-Oppenheimer approximation [51].

Factoring out the kinetic and potential energies of the nucleus and treating them classically, the electronic Hamiltonian  $\hat{H} = \hat{T}_e + \hat{V}_{ee} + \hat{V}_{eN}$ .  $V_{eN}$  is treated as the external potential. It is important to remember that two Hamiltonians with the same number of electrons can differ only in the external potential. Typically in quantum mechanics, we take the approach of solving the Schrödinger equation for the given external potential, and then calculating the values of the relevant observables from the wavefunctions. The total energy can thus be calculated taking the expectation value of the Hamiltonian. But solving for  $3N_e$  variables becomes cumbersome when dealing with systems with large number of electrons.

The electron density  $n(\mathbf{r})$  on the other hand, can be written as

$$n(\mathbf{r}) = \sum_i^{N_e} \langle \psi | \delta(\mathbf{r} - \mathbf{r}_i) | \psi \rangle = N_e \int \int \dots \int |\psi(\mathbf{r}_1, \mathbf{r}_2, \dots, \mathbf{r}_{N_e})|^2 \delta(\mathbf{r} - \mathbf{r}_1) d\mathbf{r}_1 d\mathbf{r}_2 \dots d\mathbf{r}_{N_e}, \tag{2.3}$$

and therefore, is a function of just 3 variables. Hence, one would like to express the energy in terms of the electron density  $n(\mathbf{r})$  instead of the wavefunctions.

## 2.3 Hohenberg-Kohn theorem

In 1964, Hohenberg and Kohn proved two theorems that paved the foundation to the modern density functional theory [52]. They first proved that the ground state electron density  $n(\mathbf{r})$  uniquely determines the potential of a system,  $V_{eN}$  up to an additive constant. Later, in their classic paper, they were able to show that the ground-state energy of a quantum system can be determined by minimizing the energy as a functional of the density, in much the same way as, in standard quantum mechanics where one can determine the energy by minimizing the expectation value of the Hamiltonian with respect to the wavefunction. The basic idea of DFT is to describe the system in terms of the electronic density without explicit reference to the many-body wavefunction, hence depending on 3 variables instead of  $3N_e$  variables, and thus tractable numerically.

### 2.3.1 Theorem 1

The first theorem states that, for any system of interacting particles the external potential  $V_{ext}(\mathbf{r})$ , and therefore all the properties of the system, is a unique functional of the electron density  $n(\mathbf{r})$ , up to an overall constant.

Proof: Let us start by assuming that we have two different system potentials  $V_{ext}^1(\mathbf{r})$  and  $V_{ext}^2(\mathbf{r})$  that differs by more than a constant that leads to the same ground state density,  $n_0(\mathbf{r})$ . The two external potentials clearly lead to two different Hamiltonians,  $\hat{H}^1$  and  $\hat{H}^2$ , give rise to two different ground state wavefunctions,  $\psi_1$  and  $\psi_2$ . Let us assume that these states are non-degenerate and that they give the same electronic density. Then it follows that

$$E_1 < \langle \psi_2 | \hat{H}^1 | \psi_2 \rangle = \langle \psi_2 | \hat{H}^2 | \psi_2 \rangle + \int d\mathbf{r} n_0(\mathbf{r}) (V_{ext}^1(\mathbf{r}) - V_{ext}^2(\mathbf{r})). \quad (2.4)$$

The first inequality in Eq. 2.4 comes from the fact that  $\psi_2$  is not the ground state of  $\hat{H}^1$ . The equality comes from the remembering that two Hamiltonians with the same number of electrons can differ only in the external potential.

Similarly, by switching 1 and 2 labels, we can write,

$$E_2 < \langle \psi_1 | \hat{H}^2 | \psi_1 \rangle = \langle \psi_1 | \hat{H}^1 | \psi_1 \rangle + \int d\mathbf{r} n_0(\mathbf{r}) (V_{ext}^2(\mathbf{r}) - V_{ext}^1(\mathbf{r})). \quad (2.5)$$

Adding Eq. 2.4 and Eq. 2.5, we get

$$E_1 + E_2 < E_2 + E_1, \quad (2.6)$$

which is a contradiction. Thus it can be concluded that for systems without degenerate ground states, two different potentials cannot give the same ground state electron density. Because the Hamiltonian is fully determined from the ground state density, it follows that the many-body wavefunction ( $\psi[n_0(\mathbf{r})]$ ), and thus, all properties of the system is fully determined. The proof can be extended to degenerate cases as well. [53]

### 2.3.2 Theorem 2

A universal functional for the electron energy  $E[n]$  in terms of the electron density  $n(\mathbf{r})$  can be defined. For any given  $V_{ext}(\mathbf{r})$ , the electron density  $n(\mathbf{r})$  that minimizes function  $E[n]$  will correspond to the ground state electron density  $n_0(\mathbf{r})$ .

Proof: Let us redefine the potential term so that,

$$\begin{aligned} V[n] &= \int d\mathbf{r} V_{ext}(\mathbf{r})n(\mathbf{r}), \\ F[n] &= \langle \psi | T_e + V_{ee} | \psi \rangle, \\ E[n] &= F[n] + V[n] \end{aligned} \tag{2.7}$$

and defining  $\psi \rightarrow n$  as the set of all wavefunctions that corresponds to a certain electron density  $n(\mathbf{r})$ . From variational principles, the ground state energy of the system is defined as

$$\begin{aligned} E_0 &= \min_{\psi} \{ \langle \psi | T_e + V_{ee} + V_{ext} | \psi \rangle \} \\ &= \min_n \{ \min_{\psi \rightarrow n} \{ \langle \psi | T_e + V_{ee} + V_{ext} | \psi \rangle \} \} \\ &= \min_n \{ F[n] + V[n] \} = E[n_0]. \end{aligned} \tag{2.8}$$

Therefore, one can find the exact ground state density and energies by minimizing the total energy of the system with respect to the variations in density, as long as we know  $F[n]$ .

## 2.4 Kohn-Sham auxiliary system

Minimizing the energy functional can be nontrivial for real system. Kohn and Sham devised a simple method for carrying out DFT calculations [54]. In this method, an ansatz is employed whereby the full interacting system with the real potential is mapped to a fictitious non-interacting system where the electrons feel an effective single particle potential,  $V_{KS}(\mathbf{r})$ . Thus the Hamiltonian for the auxiliary system has the form,

$$\hat{H}_{KS} = -\frac{\hbar^2 \nabla^2}{2m} + V_{KS}(\mathbf{r}) \tag{2.9}$$

The corresponding independent particle electron density is given by

$$n(\mathbf{r}) = \sum_i^{N_e} |\phi_i^{KS}|^2, \tag{2.10}$$

where  $\phi_i^{KS}$  is the  $i^{th}$  single-electron wavefunction of the auxiliary system. The independent particle kinetic energy  $T_{KS}$  is written as

$$T_{KS} = -\frac{\hbar^2}{2m} \sum_i^{N_e} \langle \phi_i^{KS} | \nabla^2 | \phi_i^{KS} \rangle = -\frac{\hbar^2}{2m} \sum_i^{N_e} \int d\mathbf{r} |\nabla \phi_i^{KS}|^2. \tag{2.11}$$

Defining the Hartree energy function that is the Coulomb interaction energy of the electron density with itself as

$$U_{Hartree}[n] = \frac{e^2}{2} \int d\mathbf{r} d\mathbf{r}' \frac{n(\mathbf{r})n(\mathbf{r}')}{|\mathbf{r} - \mathbf{r}'|}, \quad (2.12)$$

we can write the ground state energy functional in Eq. 2.7 as

$$E_{KS}[n] = T_{KS}[n] + V[n] + U_{Hartree} + E_{xc}[n], \quad (2.13)$$

where all the many-body effects of exchange and correlation have been massed in  $E_{xc}[n]$ , the exchange-correlation functional, that is calculated using the results from a homogeneous electron gas. This Kohn-Sham auxiliary system can be solved by minimizing the energy functional in Eq. 2.13 with respect to the density in Eq. 2.10, leading to the Schrödinger-like equations,

$$\hat{H}_{KS}\phi_i^{KS} = \epsilon_i^{KS}\phi_i^{KS}, \quad (2.14)$$

where  $\epsilon_i^{KS}$  is the energy of the  $i^{th}$  electron in the Kohn-Sham potential,  $V_{KS}$  given by,

$$V_{KS} = V_{ext}(\mathbf{r}) + \int d\mathbf{r}' \frac{e^2 n(\mathbf{r}')}{|\mathbf{r} - \mathbf{r}'|} + V_{XC}, \quad (2.15)$$

where

$$V_{XC} = \frac{\delta E_{XC}[n]}{\delta n(\mathbf{r})} \quad (2.16)$$

The potential and density must be self-consistently found. This Kohn-Sham equation does not depend on any approximation. If the universal functional for  $E_{XC}$  were known, then one can obtain the exact ground state energy of the many-body system.

## 2.5 Exchange and Correlation Energy

As the exact form of  $E_{XC}[n]$  is not known, one has to employ approximations in the actual calculations. Because the exchange and correlation energy,  $E_{XC}[n]$  is a non-local quantity, we can introduce  $\epsilon_{XC}([n], \mathbf{r})$  as the exchange-correlation energy per electron, which we assume to be somewhat local. The most commonly employed approximation is the local-density approximation (LDA) [54]. Within the LDA, the contribution to the exchange-correlation energy from each infinitesimal volume in space,  $d\mathbf{r}$ , is taken to be the value it would have if the whole of space were filled with a homogeneous electron gas with the same density as is found in  $d\mathbf{r}$ . Therefore,

$$E_{XC}^{LDA}[n] = \int d\mathbf{r} \epsilon_{XC}^{LDA}(n(\mathbf{r}))n(\mathbf{r}). \quad (2.17)$$

We can further divide the exchange-correlation energy per electron into individual exchange and correlation energies as,

$$\epsilon_{XC}^{LDA}(n) = \epsilon_X^{LDA}(n) + \epsilon_C^{LDA}(n). \quad (2.18)$$

Within LDA, exchange part is known analytically as we are treating the Kohn-Sham electrons as free electrons in a uniform positive background. It can be derived to be [54, 55],

$$\epsilon_X^{LDA}(n) = -e^2 \left( \frac{3n(\mathbf{r})}{\pi} \right)^{1/3} \quad (2.19)$$

The correlation part is not known exactly. But there are accurate Quantum Monte Carlo calculations, by Ceperley and Alder [56], which has been parameterized by various authors, and is implemented in most DFT packages [57–59].

There are other approximations for the exchange-correlation energy that might be more suitable for other materials. Generalized gradient approximation (GGA) is another popular approximation. It assumes that the exchange-correlation energy,  $\epsilon_{XC}([n], \mathbf{r})$ , depends not only on  $n(\mathbf{r})$  but also on its gradient,  $\nabla n(\mathbf{r})$ . In other words,

$$E_{XC}^{GGA} = \int d\mathbf{r} \epsilon_{XC}^{GGA}(n(\mathbf{r}), |\nabla n(\mathbf{r})|) n(\mathbf{r}). \quad (2.20)$$

In practice, the Kohn-Sham equations are solved in a self-consistent loop. After starting with an initial guess for the electron density, the effective potentials and the Hamiltonian is calculated. After solving the secular equation, the orbitals are used to update the initial guess for the electron density. This process is repeated till sufficient convergence is reached. In this thesis, I have primarily used Vienna *ab initio* Simulation Package (VASP) [60] and QUANTUM ESPRESSO [61] for atomic scale material modeling.

# Chapter 3

## Thickness Dependent Carrier Density at the Surface of SrTiO<sub>3</sub> (111) Slabs

### 3.1 Introduction

The perovskite structure ABO<sub>3</sub> can be considered as an alternate stacking of AO and BO<sub>2</sub> layers along the [001] direction. SrTiO<sub>3</sub> (STO) is one of the most commonly studied perovskite materials, and is usually considered as a substrate material to grow other perovskites. STO is made up of charge neutral layers of SrO and TiO<sub>2</sub> along the (001) direction. In the LaAlO<sub>3</sub>/STO system along the (001) direction, it is now generally accepted that the *intrinsic* 2DEG behavior is driven by the polarization discontinuity between the non-polar STO substrate and the polar LaAlO<sub>3</sub> film [5, 21, 62–67]. Along the [001] direction, the LaAlO<sub>3</sub> film consists of alternating layers of (LaO)<sup>+</sup> and (AlO<sub>2</sub>)<sup>-</sup>, which leads to a divergent electrostatic potential, i.e., the so-called polar catastrophe. Electronic reconstruction [62, 68–73], which is facilitated by the presence of transition metal ions, and polar distortions [63, 69, 70, 74, 75], are the two main competing mechanisms that counter this divergent potential. While polar distortions screen the electrons at the interface or surface, thereby partially compensating for the polar catastrophe, electronic reconstruction cancels the divergent potential through a transfer of charge between the interface and the surface, with the excess charge partially occupying the Ti 3*d* states, giving rise to a 2DEG. As such, a fundamental understanding of how these two effects compete with each other is important for tuning the properties of 2DEGs at oxide heterointerfaces.

Motivated by the above question, we investigated the surface electronic structure of STO (111) slabs. Along the [111] direction, a STO slab consists of alternating stacks of nominally charged (Ti)<sup>4+</sup> and (SrO<sub>3</sub>)<sup>4-</sup> layers, which already lead to a

---

This chapter is adapted from N. Sivadas, H. Dixit, V.R. Cooper and Di Xiao, Physical Review B **89**, 075303 (2014). Copyright © 2014 American Physical Society.

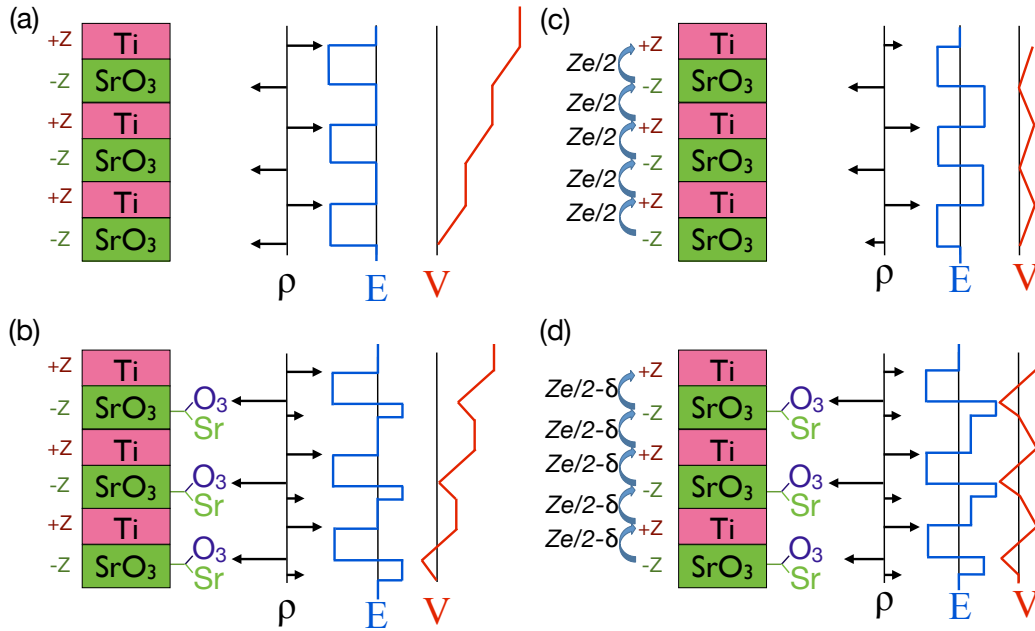


Figure 3.1: Schematic of charge density ( $\rho$ ), electric field ( $E$ ), and electrostatic potential ( $V$ ) profiles for the Ti-terminated STO (111) slabs with (a) charge uncompensated ideal atomic coordinates, (b) charge uncompensated relaxed atomic coordinates, (c) charge compensated ideal atomic coordinates and (d) charge compensated relaxed atomic coordinates. For the relaxed atomic coordinates (b) and (d), the SrO<sub>3</sub> layer (green block) splits into Sr (green line) and O<sub>3</sub> (violet line) layers.  $Z$  is the magnitude of the effective charge of each layer. Both polar distortions (b) and charge compensation due to electronic reconstruction (c) can help reduce the divergent electrostatic potential, and the net effect is less than  $Ze/2$  electrons transferred between the surfaces (d).

divergent electrostatic potential, even in the absence of a LAO overlayer (Fig. 3.1). This is in sharp contrast to a STO (001) slab, which consists of alternating charge neutral layers of SrO and TiO<sub>2</sub>. Furthermore, the presence of multivalent transition metal ions (Ti) suggests that electronic reconstruction can also take place in STO (111). Hence, STO (111) slabs offer us a unique opportunity for studying both the polar distortion and electronic reconstruction in a chemically homogeneous system.

Our work is also relevant to the recent experimental and theoretical progress on oxide (111) interfaces and surfaces. Experimental studies have reported the growth of Ti-rich STO (111) surface [76] and the creation of 2DEGs at (111) interfaces in the LAO/STO system, with carrier densities comparable to the [001] direction [77–79]. Theoretically, exotic topological phases such as the quantum spin Hall state have also been predicted for cubic perovskite (111) bilayers [80–83]. Understanding the surface electronic properties of the STO (111) slabs will have important implications for these phenomena as well.

Using density functional theory (DFT), we study STO (111) slabs of various thicknesses and different surface terminations. We show that for Ti-terminated STO slabs (Figs. 3.2a and 3.2b) it is indeed possible to create a 2DEG. However, the carrier density of the 2DEG displays strong thickness dependence due to the competition between electronic reconstruction and polar distortion. Our calculations suggest that relatively thick slabs ( $\gg 12$  layers) are required to reach the ideal carrier density (2 electrons/surface unit cell) expected from the nominal charge counting argument. In contrast, we find that the TiO-terminated slab (Figs. 3.2c and 3.2d) exhibits no charge transfer to the surface. This is because the surface oxygen functions to nullify any potential that could develop across the STO slab. A thermodynamic stability analysis shows that the Ti-terminated STO slab can be stable, albeit within a very narrow region of phase space. Our results show that both electronic reconstruction and polar distortions must be taken into account when analyzing the 2DEG behavior for (111) and (110) interfaces [77].

## 3.2 Methodology

In this work we examine STO (111) slabs with various thickness and two surface terminations: Ti (top)/SrO<sub>3</sub> (bottom)-terminated (referred to as Ti-terminated) and TiO(top)/SrO<sub>2</sub>(bottom) terminated (referred to as TiO-terminated). Both are depicted in Fig. 3.2.

The electronic ground-state calculations were performed using DFT with the local density approximation (LDA) for exchange and correlation as implemented in the QUANTUM ESPRESSO simulation package [61]. We employ ultrasoft pseudopotentials[84] including semicore electrons for O ( $2s2p$ ), Sr ( $4s4p5s$ ) and Ti ( $3s3p4s3d$ ). To account for strong electronic correlations we use a Hubbard  $U$  term (LDA+ $U$ ) [85]. For all calculations, a Hubbard  $U = 5$  eV for Ti  $d$  states was found to be appropriate. For each slab a  $1 \times 1$  in-plane periodicity with a vacuum region of  $\sim 15$  Å was used. A

cutoff energy of 80 Ry and a Monkhorst-Pack special  $k$ -point mesh of  $8 \times 8 \times 1$  for the Brillouin zone integration was found to be sufficient to obtain less than 10 meV/atom convergence. We applied a dipole correction[86, 87] to set the electric field in the vacuum region to zero. Structural optimizations were performed by fixing the in-plane lattice constant to that of the theoretical bulk STO lattice constant ( $a_0 = 3.85 \text{ \AA}$ ). All ions were then relaxed until the Hellmann-Feynman forces were less than 10 meV/ $\text{\AA}$ .

To analyze the thermodynamic stability of different surface terminations, we adopt a symmetric slab approach, i.e., the same termination on both sides. The thermodynamic analysis was performed using the generalized gradient approximations (GGA), as it usually gives more accurate formation energies, relative to experiments, than LDA.

### 3.3 Electronic structure

#### 3.3.1 Ti-termination

We first consider the ideal Ti-terminated STO (111) slab, which consists of alternating stacks of Ti and  $\text{SrO}_3$  layers with nominal charges of +4 and  $-4$ , respectively. Figure 3.3a shows the typical layer-projected DOS for a slab with 6 layers of  $\text{SrTiO}_3$  unit. We observe the occurrence of a surface metallic state for the top surface layer (Ti surface). This is similar to the results for the STO (110) surface [88] and with previous semi-empirical Hartree-Fock calculations for the STO (111) surface [89, 90]. The atomic projected DOS indicates that these surface states are comprised mainly of Ti  $s$  and  $d$  orbitals. The excess electrons are derived from the depletion of the valence band of the bottom layer due to the depopulation of O  $p$  orbitals. This can be clearly seen from the orbital dependent electronic band structure, shown in Fig. 3.3b. The dispersive energy bands clearly indicate that those excess charges are mobile carriers.

The number of excess electrons (holes) at the surface is obtained by performing an integration of the layer-averaged orbital projected DOS in a small neighborhood below (above) the Fermi level (N.B. this typically underestimates the electron count relative to the total DOS by  $\sim 0.1 e^-$ ) [65]. For the 6-layer slab, we found a total transfer of 0.7 electrons per surface unit cell. However, if electronic reconstruction is the only working mechanism, nominal charge counting dictates that there should be two electrons per unit cell transferred from the  $\text{SrO}_3$  surface to the Ti surface (Fig. 3.1c). This is a strong indication of the vital role polar distortions [69, 70, 74] play in avoiding the polar catastrophe in oxide heterostructures [21, 63].

To analyze the effect of the polar distortions, we have calculated the total transferred charge between the surface layers for different layer thicknesses for both the relaxed and the unrelaxed systems (Fig. 3.4). There are two main features. First, there is a critical thickness (3 layers) above which electronic reconstruction between the surfaces takes place, as indicated by the appearance of a 2DEG. Second, we observe a smooth increase in transferred charge with a thickness dependence for the

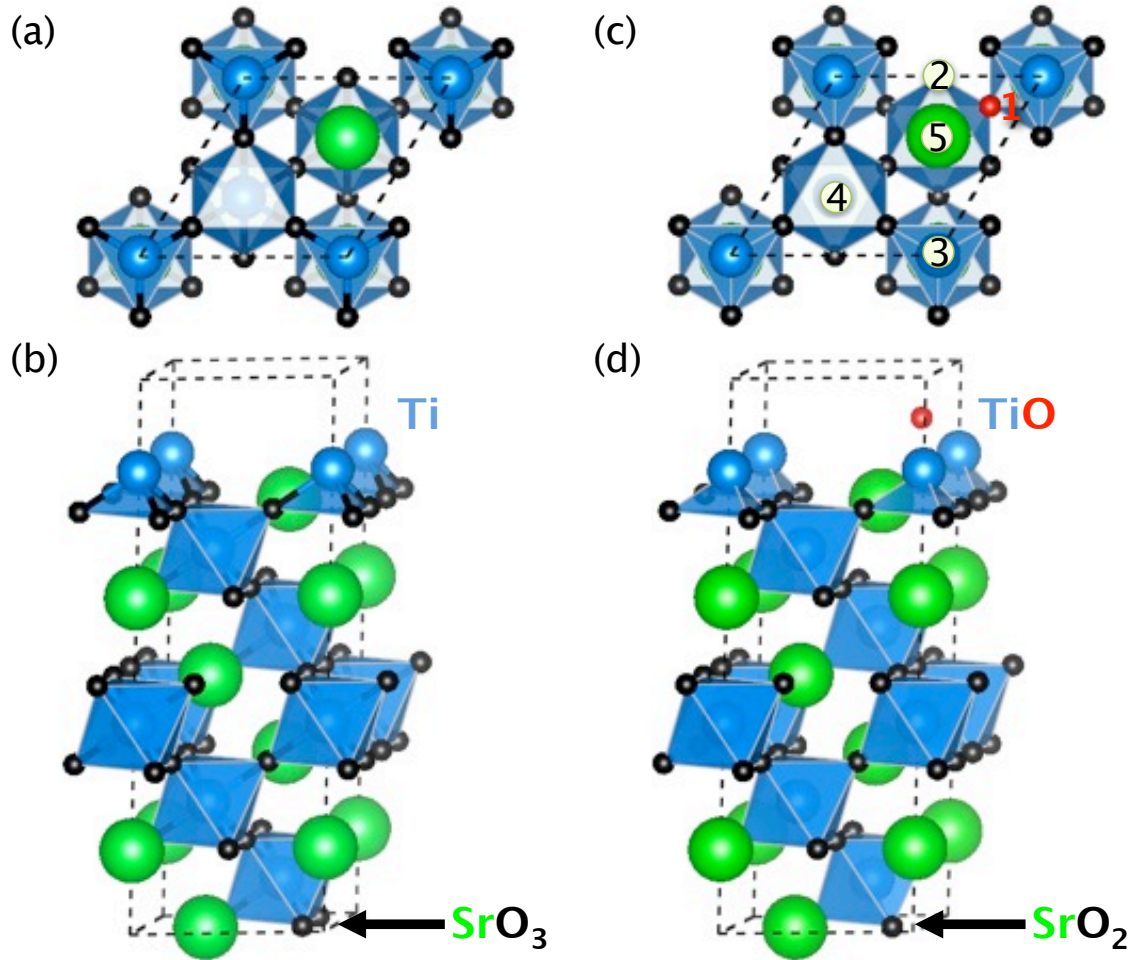


Figure 3.2: Layer-by-layer structure of the  $n=6$  STO (111) slab. (a) Top and (b) side view of the Ti-terminated STO (111) slab. (c) Top and (d) side view of the TiO-terminated STO (111) surface. Green, Blue and Black represent Sr, Ti and O ions, respectively. The five possibilities for placing the extra O atom on the Ti termination are also labeled in (c), and the energetically favorable position is marked by Red in both (c) and (d).

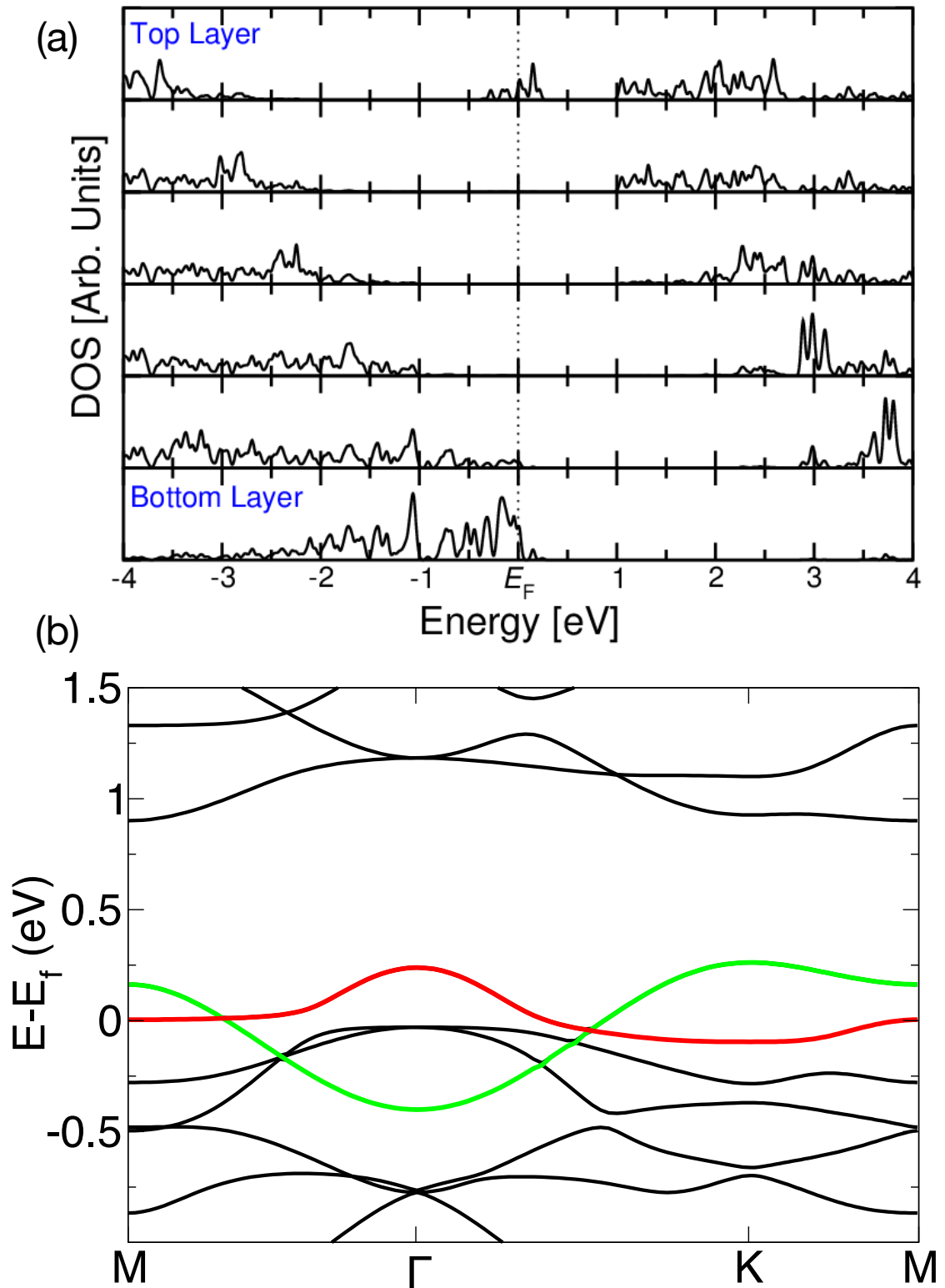


Figure 3.3: (a) Layer-dependent DOS and (b) the electronic band structure for the Ti-terminated STO (111) slab with 6 layers. There are two bands crossing the Fermi level; the top layer conduction band (green) consists mainly of Ti  $d$  states, and the bottom layer valence band (red) consists mainly of O  $p$  states.

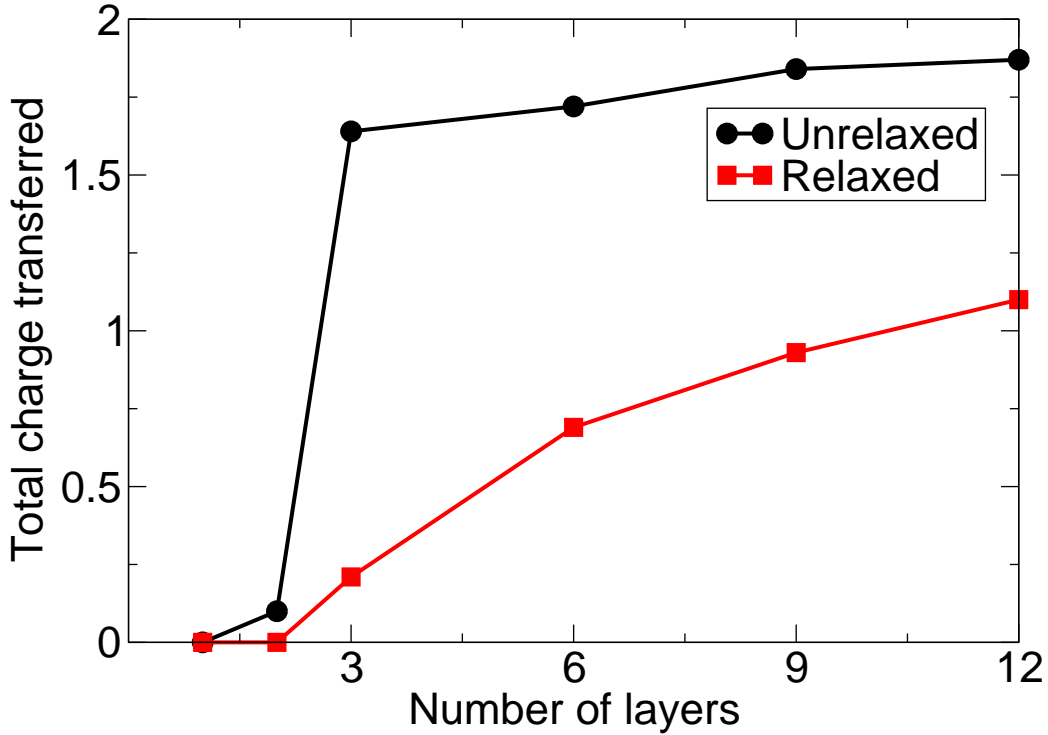


Figure 3.4: The total charge transferred between the surfaces as a function of thickness for relaxed (red) and unrelaxed (black) system.

relaxed system, which is in sharp contrast to the abrupt increase of transferred charge with very little thickness dependence for the unrelaxed system. We also note that for the unrelaxed structure, the transferred charge is very close to 2 electrons per unit cell.

The origin of the critical thickness can be explained by comparing this situation to the LAO/STO (001) heterostructure counterpart. It is well established that for these systems above an overlayer thickness of 3 layers, there is an occurrence of a 2DEG [12]. There the polar catastrophe is built up in the LAO overlayer and electronic reconstruction occurs when the divergent potential exceeds the band gap of STO. A similar effect occurs for the STO (111) slab. When the slab is thick enough to make the divergence in potential comparable to the band gap an electronic reconstruction occurs. This is clearly seen in our results for the unrelaxed surfaces (Fig. 3.4). In these systems, we observe a transfer of two electrons between the surfaces once the layer thickness is beyond a critical thickness of 2 layers. This is very abrupt and as immediate as the closing of the band gap and is a consequence

of the fact that the electronic reconstruction is the only mechanism available for countering the polar catastrophe in the unrelaxed slabs.

More interestingly, the thickness dependence of the magnitude of the charge transfer can be attributed to the effect of polar distortions. Figures 3.5a and 3.5b depict the layer-by-layer off-center (polar) distortions,  $\Delta z$ , of Sr and Ti atoms, respectively, for Ti-terminated slabs of varying STO thicknesses. As can be seen from Fig. 3.5, the net effect of the (111) surface geometry and the Ti-termination is to polarize the individual layers of SrO<sub>3</sub> and Ti layers relative to their respective oxygen cages. For all slab thicknesses, we find that in the middle of the slab there is a nearly constant shift of Ti and Sr relative to their corresponding oxygen layers, with the magnitude of the displacements decreasing with slab thickness. More important are the large off-center displacements for the surface Ti cations. Figure 3.5c shows a schematic of the effect of relaxation for 6 layers of the Ti-terminated STO slab with the percentage relaxation calculated which emphasizes the large surface distortions (N.B. these large relaxations are similar to other oxides).

The net effect of such surface dipoles is to counter the divergent potential across the slab. As the thickness of the slabs increase, however, we observe a decrease in the magnitude of these distortions. Below three layers the polar distortions are able to completely cancel out the polar catastrophe. As the thickness is increased, it becomes more energetically favorable to have an increase in the transferred charge and a decrease in polar distortion. We infer from the trend in Fig. 3.4 that for very thick STO slabs, the total amount of transferred electrons will converge to two electrons per unit cell after relaxation, just like in the case of the unrelaxed system. The competition between the electronic reconstruction and polar distortion is illustrated in Fig. 3.1.

### 3.3.2 TiO-termination

Next we consider the TiO-termination of the STO (111) slab, which is made by transferring one O atom from the bottom SrO<sub>3</sub> terminated surface to the top Ti terminated surface, as shown in Figs. 3.2c and d. When we remove one O atom from the SrO<sub>3</sub> layer, the 6 identical O sites around the Sr atom are broken into a group of 4 identical sites and 2 identical O “vacant” sites. To identify the most stable location for placing the O atom on the Ti termination, we compared the energies of 5 possible high symmetry sites as shown in Fig. 3.2c, and found that the O vacant site (1) is the preferred site.

We are interested in this situation because according to the polar catastrophe argument, one should not expect any significant electron transfer between the surfaces as the transfer of one O atom between the surfaces should stabilize the system. An analysis of the total DOS (see total DOS for 6 layers of STO in Fig. 3.6) confirms that the system is indeed insulating for all STO layer thicknesses studied ( $n = 6, 9, 12$ ).

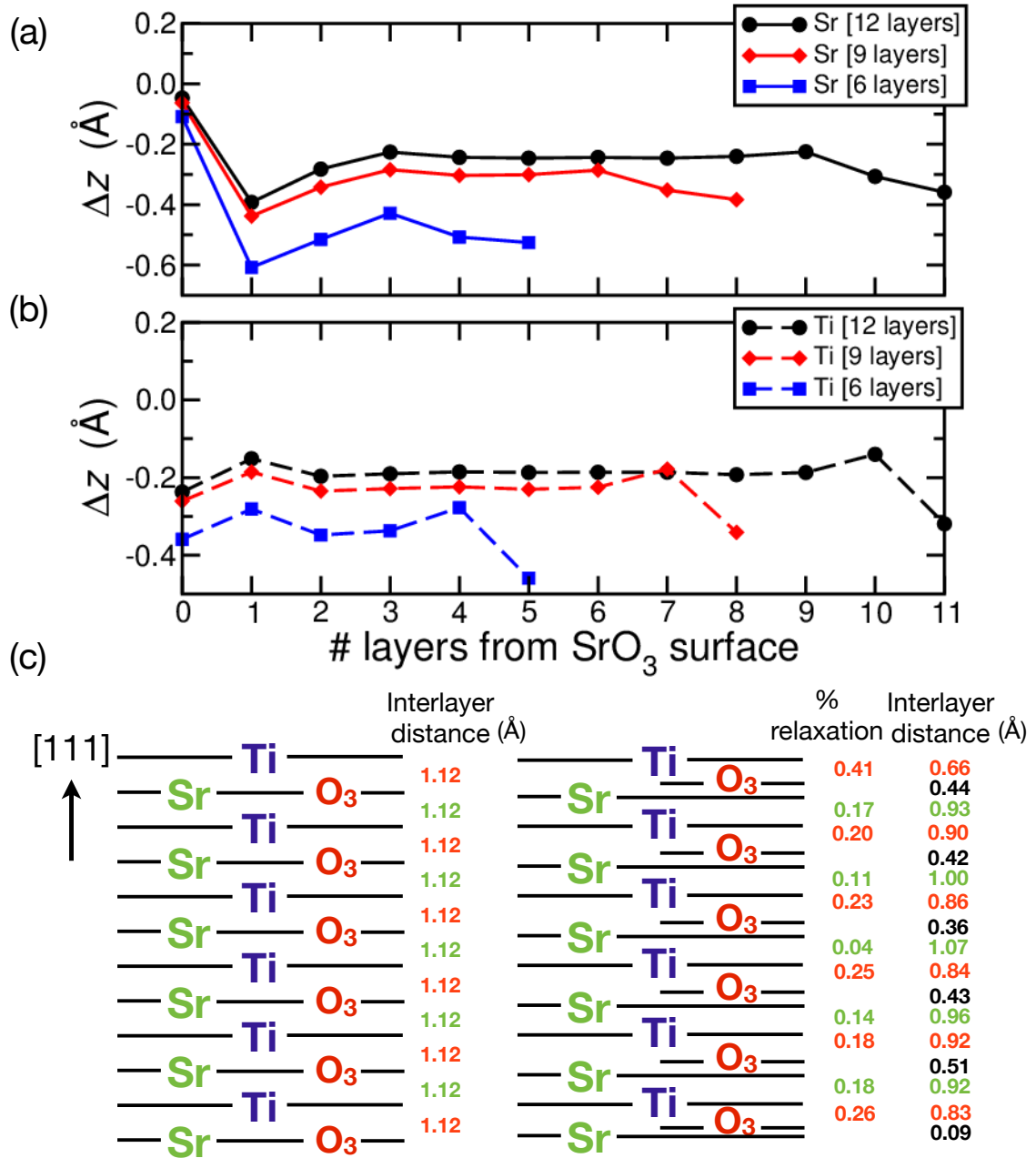


Figure 3.5: Polar distortions for the Ti-terminated STO (111) slab for layer thickness  $n = 6, 9$  and 12, relative to the  $\text{SrO}_3$  bottom layer. (a) Split between Sr and  $\text{O}_3$  in  $\text{SrO}_3$  layers. (b) Off-centering of Ti relative to planes of O anions above and below Ti. Surface Ti off-centering is computed relative to bulk positions. (c) A schematic of the effect of relaxation for the case of Ti-termination with 6 layers of STO.

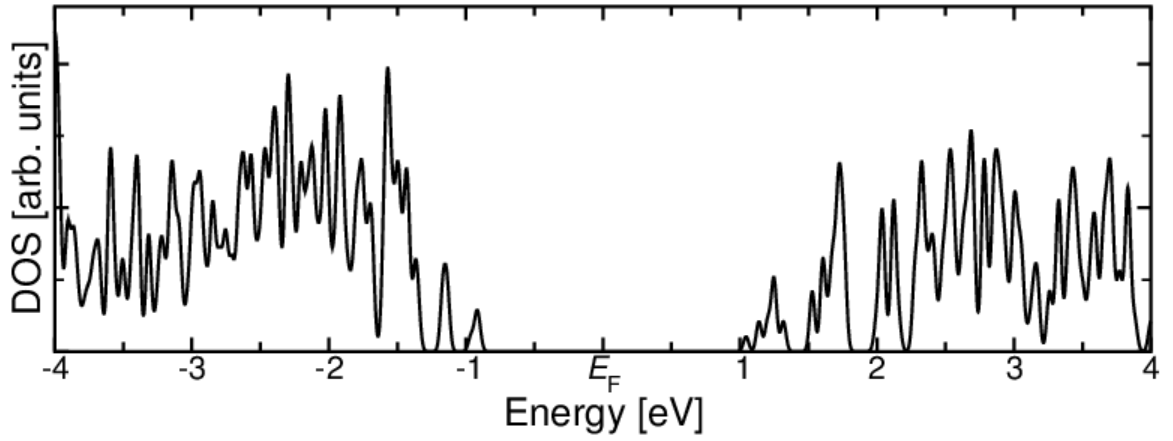


Figure 3.6: The total DOS for 6 layers of the TiO-terminated STO (111) slab.

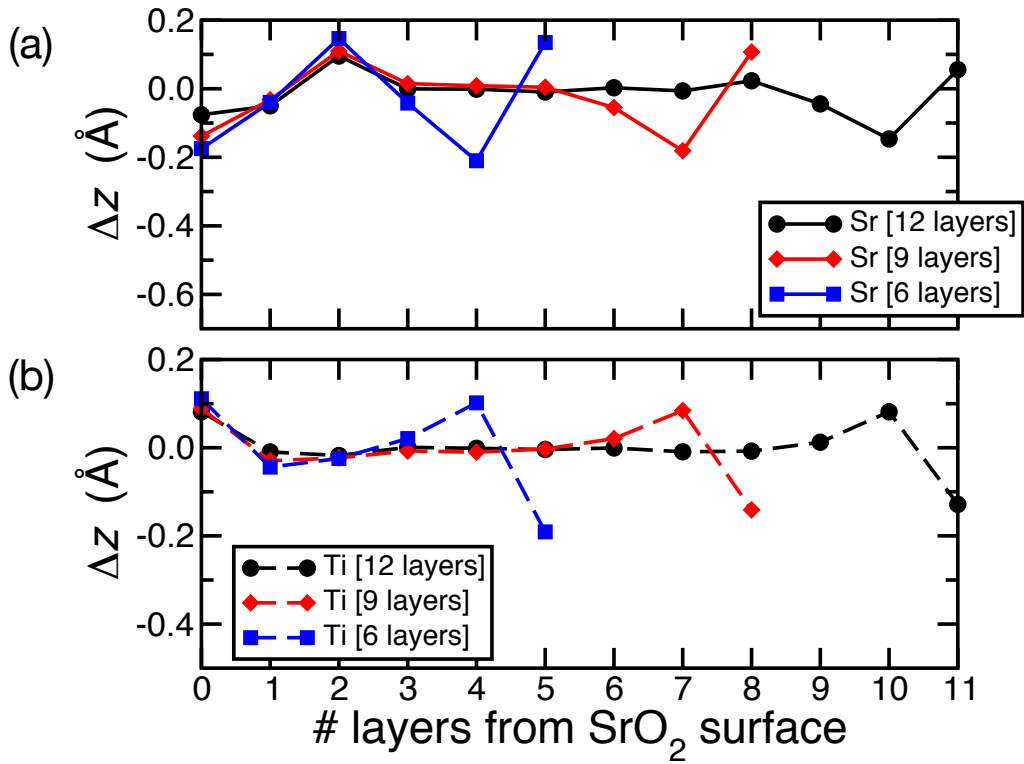


Figure 3.7: Polar distortions for the TiO-terminated STO (111) slab for layer thickness  $n = 6, 9$  and  $12$ , relative to the  $\text{SrO}_2$  bottom layer. (top) Split between Sr and  $\text{O}_3$  in  $\text{SrO}_3$  layers. (bottom) Off-centering of Ti relative to planes of O anions above and below Ti.

From this we note that there is no charge transfer between any bulk layers, similar to the Ti-terminated case. Nevertheless, we find a striking difference between the TiO- and Ti-terminated surfaces. In particular, in the case of the TiO-terminated surfaces there are no electrons transferred between the surface layers. Here, the polar catastrophe is avoided without any contribution from electronic reconstruction, unlike the case of the Ti-termination.

The atomic relaxation for each STO layer for different layer thickness of STO for the TiO-termination is shown in Fig. 3.7. Here we see that, unlike the Ti-terminated slabs, the bulk Ti and Sr cations exhibit negligible off-center displacements. Such displacements are indicative of having a reduced electric potential across the slab. However a larger polar distortion develops on the topmost plane of Ti ions, which is a local relaxation effect. To conclude, the effect of polar distortion in this case is much less compared to the Ti-termination (Fig. 3.5) as the transfer of one oxygen atom is effective in screening the polarization, with the help of some local relaxation. This is in agreement with the observation of the lack of charge transfer for different thicknesses for this system.

### 3.4 Thermodynamic stability

The imminent question is the relative thermodynamic stability of these different surface terminations. In this section we analyze the thermodynamic stability of the various terminations of the STO (111) surface, following the formalism proposed by F. Bottin *et.al.* [88] The energy required to split a crystal in half with complementary surfaces is called the cleavage energy. The cleavage energy ( $E_{\text{cl}}$ ) per surface area for the unrelaxed Ti/SrO<sub>3</sub> terminations and unrelaxed TiO/SrO<sub>2</sub> terminations respectively are defined in the following

$$\begin{aligned} E_{\text{cl}}^{\text{Ti/SrO}_3} &= \frac{1}{2S} (E_{\text{slab}}^{\text{Ti}} + E_{\text{slab}}^{\text{SrO}_3} - nE_{\text{bulk}}), \\ E_{\text{cl}}^{\text{TiO/SrO}_2} &= \frac{1}{2S} (E_{\text{slab}}^{\text{TiO}} + E_{\text{slab}}^{\text{SrO}_2} - nE_{\text{bulk}}), \end{aligned} \quad (3.1)$$

where  $E_{\text{bulk}}$  stands for the total energy of the bulk STO system,  $n$  the total number of STO layers and  $S$  denotes the surface area. Here  $E_{\text{slab}}^\lambda$  is the energy of  $\lambda$  termination, with  $\lambda$  being either Ti, SrO<sub>3</sub>, TiO or SrO<sub>2</sub>.

Since the cleavage energy does not distinguish between the two complementary surfaces, we define the surface energy,  $\Phi_\lambda$ , which is a measure of the stability of the surface with respect to bulk as:

$$\begin{aligned} \Phi_\lambda &= \frac{1}{2S} [E_{\text{slab}}^\lambda - N_{\text{Ti}}E_{\text{bulk}} - E_{\text{O}_2}^{\text{mol}}/2(N_{\text{O}} - 3N_{\text{Ti}}) \\ &\quad - E_{\text{Sr}}^{\text{bulk}}(N_{\text{Sr}} - N_{\text{Ti}})]. \end{aligned} \quad (3.2)$$

Table 3.1 shows the cleavage energy, relaxation energy and the surface energy for different terminations. The values for cleavage energy are in good agreement with previous first-principles calculations for STO (111) surfaces [91].

Table 3.1: The unrelaxed cleavage energy, relaxation energy and surface energy in J/m<sup>2</sup> for different terminations.

	SrO <sub>3</sub>	Ti	SrO <sub>2</sub>	TiO
$E_{cl}$	6.62	6.62	4.58	4.58
$E_{rel}$	-0.27	-1.45	-1.54	-1.69
$\Phi_\lambda$	6.36	5.17	3.04	2.89

However this definition of surface energy excludes the possibility of contact with matter reservoir. Hence we compute the surface grand potential,

$$\Omega_\lambda = \frac{1}{2S} [E_{slab}^\lambda - N_{Ti}\mu_{Ti} - N_{Sr}\mu_{Sr} - N_O\mu_O], \quad (3.3)$$

which is a measure of the excess energy of a symmetric system exposing a termination of a given composition, to a reservoir. The quantities  $\mu_{Ti}$ ,  $\mu_{Sr}$ ,  $\mu_O$  in Eq. (3.3) are the chemical potentials of the Ti, Sr and O atomic species, respectively, and  $N_{Ti}$ ,  $N_{Sr}$ ,  $N_O$  are the number of Ti, Sr and O atoms in the slab. The chemical potential of the bulk STO system ( $\mu_{SrTiO_3}$ ) can be written as the sum of chemical potentials of individual species in the crystal:

$$\mu_{SrTiO_3} = \mu_{Sr} + \mu_{Ti} + 3\mu_O. \quad (3.4)$$

When the surface is in equilibrium with the bulk, we have  $\mu_{SrTiO_3} = E_{bulk}$ . Using this and Eq. (3.4) we can rewrite the surface grand potential in Eq. (3.3) as:

$$\Omega_\lambda = \frac{1}{2S} [E_{slab}^\lambda - N_{Ti}E_{bulk} - \mu_O(N_O - 3N_{Ti}) - \mu_{Sr}(N_{Sr} - N_{Ti})]. \quad (3.5)$$

From this we observe that the range of accessible values for the surface grand potential depends on the maximum and minimum values of  $\mu_{Sr}$  and  $\mu_O$  chemical potentials. The possible variations in  $\mu$  reflect the experimental growth conditions. Under the O rich condition  $\mu_O = E_{O_2}^{molecule}/2$  and for the Sr rich condition  $\mu_{Sr} = E_{Sr}^{bulk}$ . Defining  $\Delta\mu_O = \mu_O^{SrTiO_3} - E_{O_2}^{molecule}/2$  and  $\Delta\mu_{Sr} = \mu_{Sr}^{SrTiO_3} - E_{Sr}^{bulk}$  we obtain

$$\Omega_\lambda = \Phi_\lambda - \frac{1}{2S} [\Delta\mu_O(N_O - 3N_{Ti}) + \Delta\mu_{Sr}(N_{Sr} - N_{Ti})]. \quad (3.6)$$

The ranges of the two independent parameters,  $\Delta\mu_O$  and  $\Delta\mu_{Sr}$  can be determined using the following set of conditions. In order to avoid the elements precipitating into

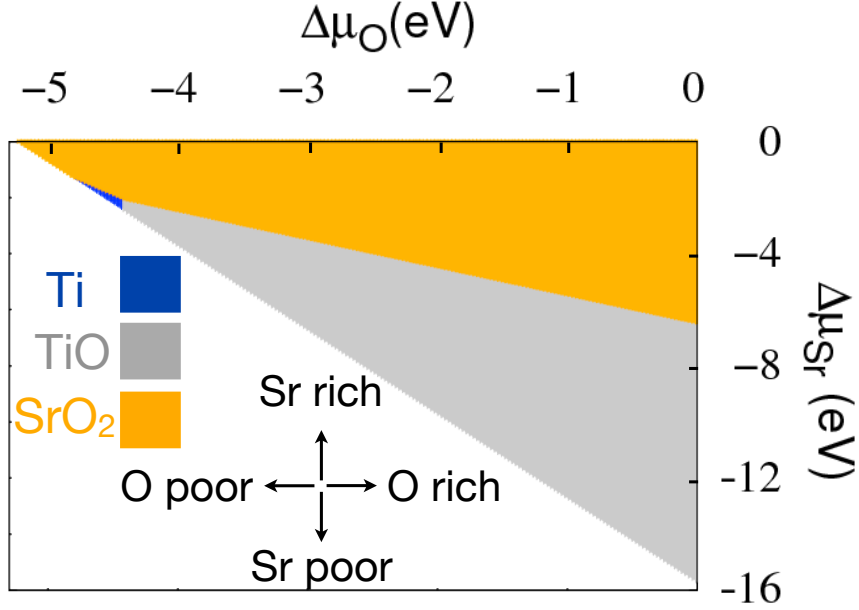


Figure 3.8: Stability diagram of the STO (111) surface. The most stable termination is shown as a function of the chemical potential of O and Sr.

Sr bulk, Ti bulk and oxygen gas, the upper bounds are set by  $\Delta\mu_{\text{Sr}}, \Delta\mu_{\text{Ti}}$  &  $\Delta\mu_{\text{O}} \leq 0$ . The lower bounds are obtained using:

$$\Delta\mu_{\text{Sr}} + 3\Delta\mu_{\text{O}} > -E_{\text{SrTiO}_3}^f, \quad (3.7)$$

where the formation energy ( $E_{\text{SrTiO}_3}^f$ ) is defined as

$$-E_{\text{SrTiO}_3}^f = E_{\text{SrTiO}_3}^{\text{bulk}} - E_{\text{Ti}}^{\text{bulk}} - E_{\text{Sr}}^{\text{bulk}} - \frac{3}{2}E_{\text{O}_2}^{\text{molecule}}. \quad (3.8)$$

Figure 3.8 shows the relative stability of different terminations in the  $(\Delta\mu_{\text{O}}, \Delta\mu_{\text{Sr}})$  plane after computing  $\Omega$ . The shaded area shows the region in the chemical potential phase space where a particular termination is most stable. We observe that the SrO<sub>2</sub>-SrO<sub>2</sub> termination is most stable under O and Sr rich condition. When  $\mu_{\text{Sr}}$  is lowered, the TiO-TiO termination becomes the most stable surface. However for low oxygen pressure, there is also a region where the Ti termination is stable, which implies that it is possible to observe the effect of electronic reconstruction by tuning the experimental conditions for STO (111) surface. It should be noted that for the STO (111) surface a stable Ti-rich surface has already been observed (albeit without any knowledge of

O content) [76]. Nevertheless, these results highlight the possibility of creating the Ti-terminated surface and may have specific consequences for the electronic states that could be created at a heterostructure interface.

### 3.5 Summary

In summary, we have studied STO (111) slabs of various thicknesses and different surface terminations using density functional theory. We observe that for the Ti-SrO<sub>3</sub> terminated STO (111) slab there is charge redistribution which is dominated by the transfer of electrons from the SrO<sub>3</sub> terminated surface to the Ti surface, giving rise to a metallic surface states for this configuration. The carrier density of the 2DEGs display a strong thickness dependence due to the competition between electronic reconstruction and polar distortions. In comparison, for the TiO-terminated surface, no such surface states exist and the compensation mechanism is dominated by the new surface boundary conditions created by the transfer of an O ion from one surface to the other. By studying the relative stability of these different terminations we observe that the Ti termination can indeed be stabilized depending upon the experimental conditions. Naturally, the ability to tune the magnitude of charge transfer/compensation at an oxide surface/interface has consequences on numerous applications including surface catalysis and oxide electronics as well as important implications for novel phenomena such superconductivity and magnetism in confined dimensions.

# Chapter 4

## Oxygen Vacancies on SrTiO<sub>3</sub> (001) surfaces

### 4.1 Introduction

Even after a decade since its discovery, the actual driving force behind 2DEG formation is still not well understood. Apart from polarization effects, a second mechanism that has been believed to form 2DEG is due to surface oxygen vacancies. In fact, even the non-polar (001) surface of SrTiO<sub>3</sub> exhibits this behavior [14, 92, 93]. It was found that by exposing a low temperature, vacuum-cleaved surface of SrTiO<sub>3</sub> (001) to strong ultraviolet light, a defect level at 1.3 eV below the Fermi level was created together with the formation of 2DEG [14]. Intriguingly, this well-known oxygen vacancy state [14, 94–98] lies too deep below the conduction band to provide carriers and form the 2DEG. The role of the oxygen vacancy state in the formation of 2DEG is still not clear.

The theoretical calculations were primarily motivated by the room temperature scanning tunneling spectroscopy (STS) on STO (001) surfaces. In the experiments, both cleaved and homoepitaxially grown surfaces were studied. In both cases, oxygen deficient environment was experimentally ensured. STS was performed at room temperature with Pt/Ir tips. In order to obtain a higher sensitivity, the tip-sample separation was varied as a function of applied bias [99, 100]. Experiments using STS can selectively probe different terminations of the SrTiO<sub>3</sub> (001) surface, i.e. SrO and TiO<sub>2</sub> terminations.

This study of their electronic structures revealed that the presence of an in-gap level in the SrO-terminated side (see Fig. 4.1). This feature was attributed to oxygen vacancies as the density of centers responsible for this level was found to increase with surface segregation of oxygen vacancies through annealing (Fig. 4.1 (b)) and decrease with exposure to molecular oxygen (Fig. 4.1 (c)).

---

This chapter is adapted from W Sitaputra, N Sivadas, M Skowronski, D Xiao and RM Feenstra, Physical Review B **91**, 205408 (2015). Copyright © 2015 American Physical Society.

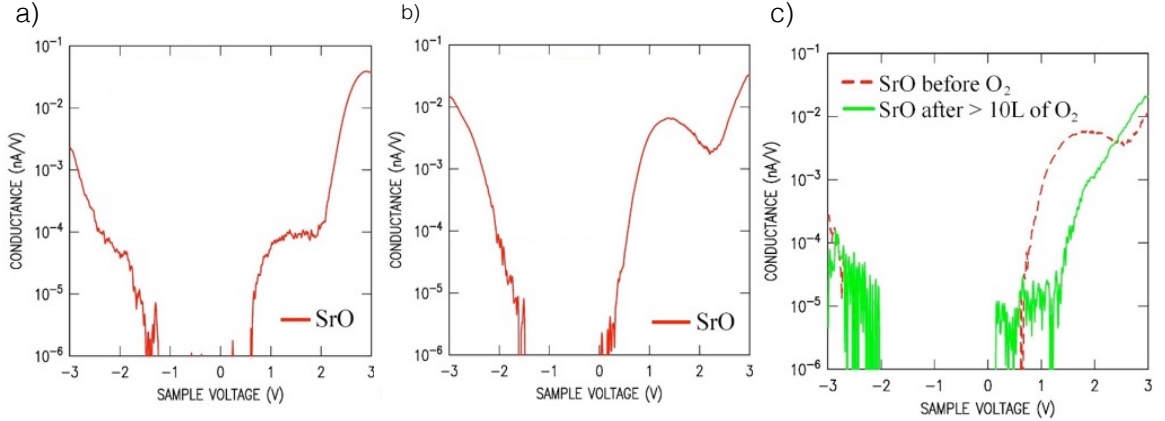


Figure 4.1: The average conductance spectra on SrO-terminated cleaved SrTiO<sub>3</sub> acquired (a) before and (b) after segregation of surface oxygen vacancies by moderate-temperature annealing. (c) Comparison between conductance spectra from the annealed SrO-terminated surfaces before (red) and after 10 L of molecular oxygen exposure (green). The sample voltage corresponds to the energy of a state relative to the Fermi level (0 V in the spectra).

The position of this level with respect to the Fermi energy was found to vary with a roughness of the surface, signifying the presence of coexisting disorder-induced surface states. On the other hand, no such level is observed for a vacancy on a surface TiO<sub>2</sub> plane. To explain the experimental observations, we employ first-principles predictions of the oxygen vacancy electronic structure, using the LSDA + U method. The results show different positions of the transition levels for different terminating planes. For the SrO termination, we predict a donor level, i.e. (0/+) transition level, in approximate agreement with our experimental observations. For the TiO<sub>2</sub> termination, we predict a donor level that is resonant with the conduction band, in agreement with prior theory and experiment [14, 92, 101]. For both terminations, we also predict in-gap levels for the double donor, i.e. (+/++) transition level. These levels were also observed in some of the scanning tunneling spectra obtained on the TiO<sub>2</sub>-terminated surfaces.

## 4.2 Methodology

Prior theoretical studies have shown the relevance of oxygen vacancies to observed in-gap states [102]. Most of the previous works have focused on the Kohn-Sham gap states of neutral vacancies [102–105]. However, the experimentally observed gap-feature must be accompanied by a charge transition level from the oxygen vacancy for it to be correctly associated with theoretical calculations. We examined SrTiO<sub>3</sub> (001) slabs with one oxygen vacancy per simulation cell, as shown in Figure. 4.2. We

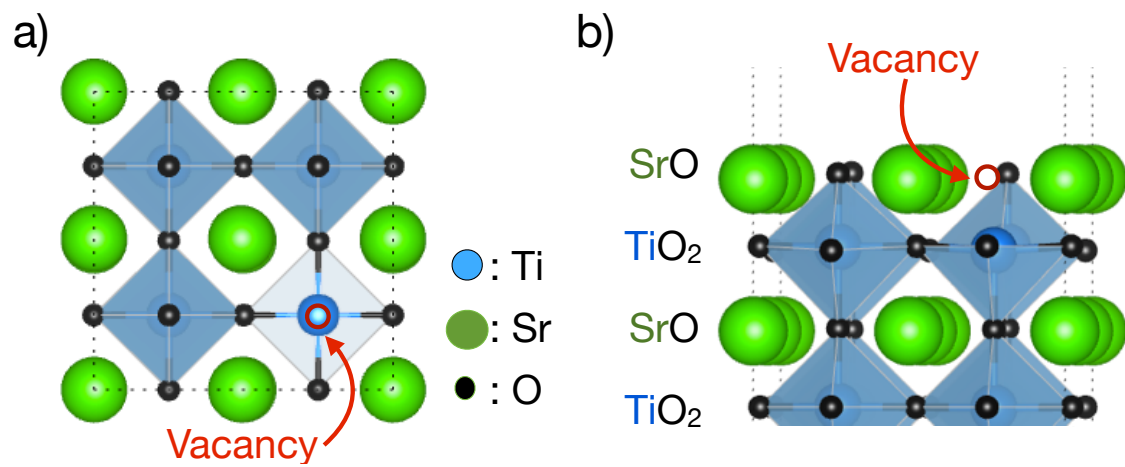


Figure 4.2: (a) The top view and (b) the side view of SrO-terminated SrTiO<sub>3</sub> surface with an oxygen vacancy (open red circle). A vacuum region more than 15 Å was used.

analyze the relative energetics of an oxygen vacancy, in various charge states, as a function of its position relative to the surface. The electronic ground-state calculations for the neutral ( $V_O^0$ ), +1 charged ( $V_O^{+1}$ ) and +2 charged ( $V_O^{+2}$ ) oxygen vacancies were performed using DFT with the local spin density approximation (LSDA+U) for exchange and correlation as implemented in the QUANTUM ESPRESSO simulation package [106]. To account for strong electronic correlations we use a Hubbard U term [85] and a spin polarized calculation was employed because of the magnetic nature of the oxygen vacancies [107]. Our results reported here utilize  $U = 5$  eV for Ti d states, although the qualitative trends in our results (e.g. resonant state for  $\text{TiO}_2$  termination vs. in-gap state for  $\text{SrO}$  termination) are consistent with values of  $U$  in the range 4 to 5 eV [108, 109]. We employ ultra-soft pseudopotentials [84] including semicore electrons for O ( $2s2p$ ), Sr ( $4s4p5s$ ) and Ti ( $3s3p4s3d$ ). For each slab a  $2 \times 2$  in-plane periodicity and 4  $\text{SrTiO}_3$  layers along the z-direction was used, along with a vacuum region of  $\sim 15$  Å. A cutoff energy of 80 Ry and a Monkhorst-Pack special k-point mesh of  $4 \times 4 \times 1$  for the Brillouin zone integration was found to be sufficient to obtain better than 10 meV/atom convergence. Structural optimizations were performed by fixing the in-plane lattice constant of one  $\text{SrTiO}_3$  unit to that of the theoretical bulk  $\text{SrTiO}_3$  lattice constant ( $a_0 = 3.85$  Å). All ions were then relaxed until the Hellmann-Feynman forces were less than 10 meV/Å.

Under thermodynamic equilibrium, in the dilute limit (negligible defect-defect interaction), the concentration of the defects dependent on the formation energy as [110],

$$C = N_V e^{-\frac{E_{form}}{k_B T}}, \quad (4.1)$$

where  $N_V$  is the number of vacancies,  $E_{form}$  is the formation energy,  $k_B$  the Boltzmann constant and  $T$  the temperature. Thus, the defects with higher formation energy have a lower concentration. In fact, the formation energy of point defects depends on growth conditions. For charged vacancies, the formation energy further depends on the Fermi level ( $E_F$ ), which is the energy of the electron reservoir. Thus, the formation energy of  $\text{SrTiO}_3$  with one oxygen vacancy can be expressed as

$$E_{form}[V_O^q] = E_{tot}[V_O^q] - E_{tot}[\text{SrTiO}_3] + \mu_O + q(E_F + \Delta_q) \quad (4.2)$$

where  $E_{tot}[V_O^q]$  is the total energy of supercell containing oxygen vacancy in a charge state  $q$ ,  $E_{tot}[\text{SrTiO}_3]$  is the total energy of a  $\text{SrTiO}_3$  perfect crystal in the same supercell, and  $\mu_O$  is the oxygen chemical potential which captures the growth conditions. The Fermi level  $E_F$  is referenced with respect to the valence-band maximum. The charge-state dependent constant  $\Delta_q$  is added to correct the formation energies of the charged defects and is discussed below.

Calculating the formation energy of charged defects in bulk has been addressed in detail in Walle *et.al.* [111]. But treating the formation energies of charged defects on surfaces pose a considerable challenge. In the first-principles step, a compensating background charge is added to maintain overall charge neutrality and also to avoid

the divergence of the electrostatic energy. In bulk defects this approach is tractable. But in the case of charged defects on surfaces this produces an unphysical situation where the compensating charge is in the vacuum region as well. On top of that, the absence of a dielectric medium hampers the convergence of the total energy with respect to the size of the supercell.

Using the dipole-correction implemented in most first-principles packages, we can partially correct for the spurious change in the vacuum region. But the artificial defect-defect interaction and the compensating charge-defect interactions still remains because of its long-range nature. So, to correctly calculate the formation energies one needs to perform convergence study with respect to both vacuum thickness and supercell size. This is computationally challenging for large systems. Therefore, some post-processing schemes have been developed to circumvent this problem [112–115]. All of them try to correct the formation energy in Eq. 4.2 through the  $q$ -dependent correction term ( $\Delta_q$ ). As the Fermi-level is referenced to the bulk valance band maximum (VBM), the correction comes through the alignment of the electrostatic potential of the defect system to the bulk system. Here, we have calculated  $\Delta_q$  by aligning the core levels (Sr 3s) far away from the defect [114]. Although, this procedure has the shortcoming of assuming that the VBM is unaffected by the charged defect. A more rigorous approach by Komsa *et al.* [115] correctly accounted for the long-range nature of the Coulomb potential.

Further, even with LDA+U, the band gap is underestimated and it needs to be scaled to the experimental value. While correcting the band gap, the formation energy obtained for a specific value of U also needs to be corrected. In this procedure, the formation energy of  $V_O^{+2}$  is not affected as we vary U (i.e. change the band gap), since for  $V_O^{+2}$  the Kohn-Sham gap state is empty and hence the total energy is unaffected as we vary both the band gap and the associated position of the Kohn-Sham gap state. For the  $V_O^{+1}$  and  $V_O^0$  cases, the formation energies are corrected assuming that the Kohn-Sham gap feature shifts with the conduction band (CB), since the gap feature exhibits CB orbital character (85 % for  $V_O^0$  and 80% for  $V_O^{+1}$ , respectively). This approximation is known to work well for conventional semiconductors where the gap feature has predominantly CB character [111, 116–118]. Hence, we add  $(E_{g,exp} - E_{g,LDA+U(5)})n$  to the formation energy, where  $E_{g,exp}$  is the experimental band gap,  $E_{g,LDA+U(5)}$  is the band gap obtained from DFT calculation and  $n$  the occupation of the Kohn-Sham gap state. To verify the accuracy of this correction and the choice of U, the transition levels thus obtained were evaluated for a bulk vacancy (Fig. 4.3(a)), yielding (+/++) and (0/+) levels located right at the CB minimum and 0.3 eV above the CB minimum, respectively. These results agree within a few tenths of an eV with those obtained by Janotti *et al.* [101], using a more accurate hybrid functional.

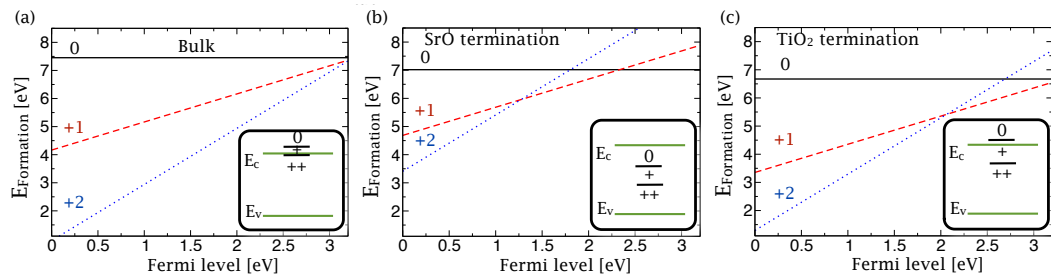


Figure 4.3: The formation energy as a function of Fermi level for different charge configurations for the oxygen vacancy in (a) the bulk, (b) the surface SrO layer, and (c) the surface TiO<sub>2</sub> layer. Insets show the resulting transition levels (Fermi level position at which transitions between charge states occur). For panel (c), the transition between +1 and 0 charge states occurs at a Fermi level position slightly above the CB minimum.

## 4.3 Results and discussion

### 4.3.1 Formation energy and defect wavefunction

Figures 4.3(a)-(c) show the vacancy formation energies as a function of the Fermi level for the bulk, the SrO termination and the TiO<sub>2</sub> termination, respectively. For the SrO termination, we predict two transition levels, between +1 and +2 charge states (+/+), and between 0 and +1 charge states (0/+), when the Fermi level is 1.3 eV and 2.3 eV above the valence band maximum (VBM), respectively. The position of the (0/+) level approximately matches the gap feature that we observed experimentally on the SrO termination. However, the lower (+/+) level was not observed in the STM experiments. The disorder-induced states on the surface would likely have pinned the Fermi level in between the two levels, such that only (0/+) level is empty but the (+/+) level is filled. In that case, the absence of (+/+) level can be attributed to a limited transport capability for in-gap states below the Fermi level of n-type material [119]. For in-gap surface states above the Fermi level (positive voltages), electrons tunneling into the states can tunnel through the depletion region into CB states, and observable current is thus achieved. However, for in-gap surface states below the Fermi level (small or moderate negative voltages), there are no bulk states available for the carriers to tunnel into, and thus their conductance is poor. Only when the density of surface states is large enough to allow lateral transport across the surface can these states be observed [120].

For TiO<sub>2</sub> termination, our calculation predicts a (+/+) level at 2.1 eV above the VBM, which in principle should be observable in the conductance spectra. However, no such discrete state was observed in the spectra. In some of the cleaved samples, a weak, discrete feature was occasionally observed in the upper half of the band gap for TiO<sub>2</sub>-terminated surfaces after annealing. To further investigate the nature of the states on the different terminations, we compute the spin density of the in-gap state in its various charge states, as shown in Fig. 4.4(a)-(f). In the bulk, the oxygen ion has two nearest neighbor Ti ions. The wavefunctions of the vacancy in either  $V_O^{+1}$  or  $V_O^0$  states are mostly made of Ti 3d orbitals pointing at the vacancy. On the SrO-terminated surface, the oxygen vacancy has only one Ti neighbor directly underneath. Therefore, the in-gap state is mostly made up of  $d_{z^2}$  orbitals, which point towards the vacancy as clearly seen in Fig. 4.4(a)-(b). For the case of  $V_O$  and  $V_O^+$  at the TiO<sub>2</sub> surface, the orbital character is dominated by the  $d_{x^2-y^2}$  and  $d_{zy}$  orbitals pointing towards the vacancy, as shown in Fig. 4.4 (d) - (e). This difference in orbital characteristic for the oxygen vacancy state at different terminations has a direct consequence for the sensitivity of the STS. The tunnel current is more sensitive to an orbital that points out in the direction perpendicular to the surface, since it has greater overlap with the wavefunctions of the tip. Therefore, it should be easier to detect the oxygen vacancy states on the SrO-terminated surface due to their dominant out-of-plane  $d_{z^2}$  orbital characteristics. Detecting the oxygen vacancy states on TiO<sub>2</sub>-

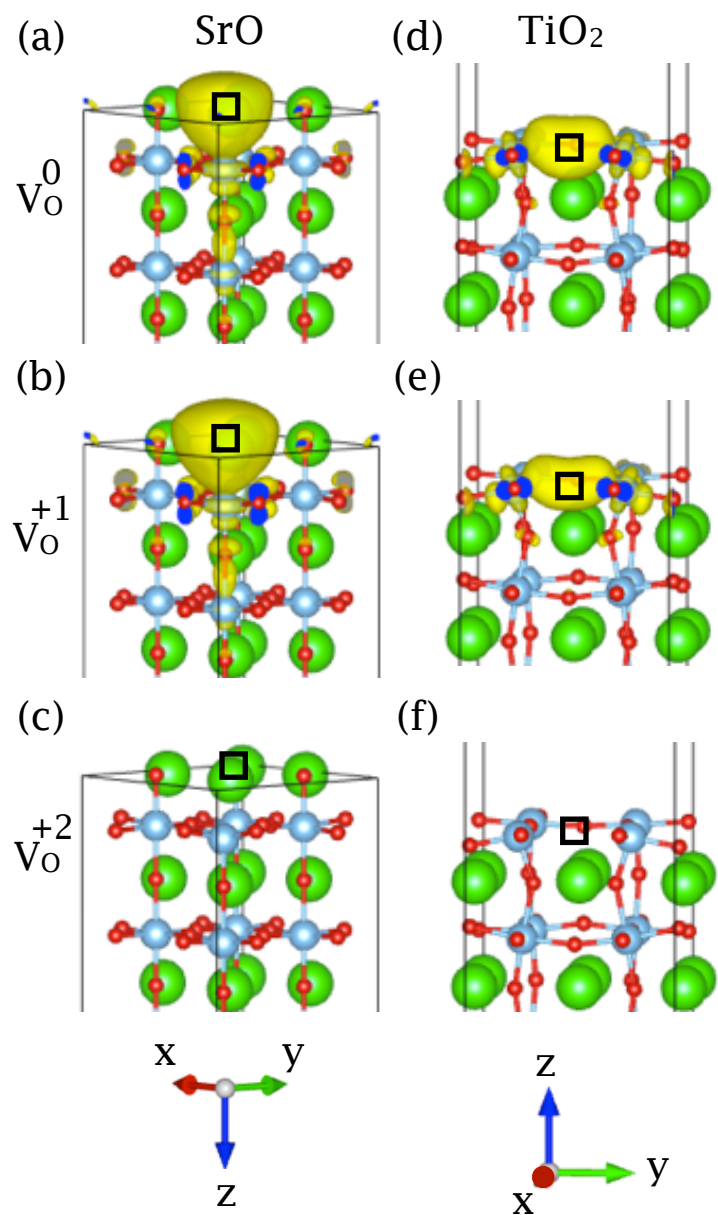


Figure 4.4: The majority spin density for the  $V_O^0$ ,  $V_O^{+1}$  and  $V_O^{+2}$  in the SrO and TiO<sub>2</sub> surface layer. The isosurfaces (yellow lobes) correspond to 2% of the maximum value in each plot. Green, blue and red balls represent Sr, Ti and O atoms, respectively. Square solid box represents position of the oxygen vacancy.

terminated surface, on the other hand, is relatively difficult because the wavefunctions extend mostly along the surface. This characteristic of the wavefunction provides an explanation for the absence of any discrete in-gap state for the  $\text{TiO}_2$  termination in our experiments.

Concerning the predicted (0/+) level on the  $\text{TiO}_2$ -terminated surface, in sharp contrast to the SrO-terminated case, it appears as a resonant level in the conduction band. Such a resonant level will autoionize with the electron transferred to the conduction band. The resulting positively charged vacancies will cause downward band bending, leading to the formation of a 2DEG. This is the mechanism responsible for 2DEG formation on  $\text{SrTiO}_3$  surface, as elucidated in some prior publications [121–127]. In contrast, for our surfaces produced experimentally, there apparently is always a sufficient number of disorder-induced states to accept electrons from the oxygen vacancies and thereby inhibit for 2DEG formation.

### 4.3.2 Configurational Coordinate diagram and vibronic coupling

Regarding the observed position of the (0/+) on the SrO termination from STS, the breadth of the spectral feature is quite large indicating a possible electron-phonon coupling. To evaluate such coupling, we calculated configuration coordinate (CC) diagrams [128], together with the square of the vibronic (harmonic oscillator) wavefunction for the  $V_O^0$  vacancy and the  $V_O^{+1}$  vacancy for the SrO termination (Fig. 4.5(a) and (b)). When the Fermi energy is 2.3 eV, the  $V_O^{+1}$  vacancy together with one electron has the same energy as the  $V_O^0$  vacancy, but there is minimal overlap between their vibronic states and hence there is very little tunneling. On the other hand, when the Fermi energy is changed to 2.5 eV (by adjusting the applied tunneling sample-tip bias voltage), the  $V_O^{+1}$  vacancy level moves up such that the minimum of its CC curve intersects the CC curve of the  $V_O^0$  vacancy. At this value of Fermi energy (sample-tip bias) there is maximal overlap between the  $V_O^{+1}$  and  $V_O^0$  vibronic states, which corresponds to the peak observed in the  $dI/dV$  spectrum. With this vibronic coupling taken into account, the actual position of the surface oxygen vacancy feature in STS is theoretically predicted to be at 2.5 eV above the VBM. This value is reasonably close to the transition energy found experimentally for the (0/+) transition level of the SrO-terminated surface.

## 4.4 Summary

Thus, to summarize, we have used first-principles methods to calculate the formation energies of charged oxygen vacancies on STO (001) surfaces. We find that a transition level above the CB edge is formed by vacancies in the outermost plane of  $\text{TiO}_2$ -terminated surfaces (this result is essentially the same as believed to occur

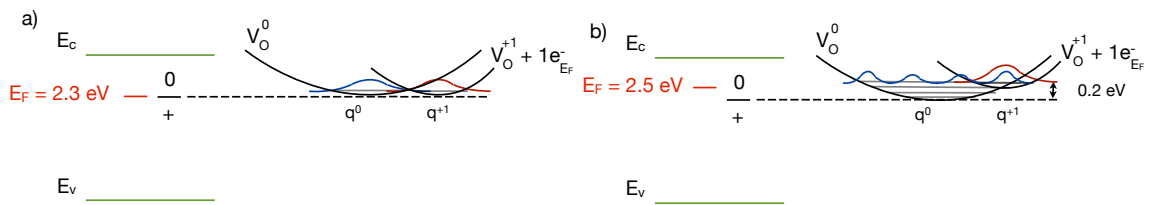


Figure 4.5: Configuration coordinate diagram for the SrO termination for  $V_O^0$  and  $V_O^{+1}$  for a Fermi energy of (a) 2.3 eV and (b) 2.5 eV. A schematic of the absolute square of harmonic oscillator wavefunctions are shown for both the neutral and + charge states of the vacancy.

for vacancies in bulk SrTiO<sub>3</sub>) [101]. This resonant level will produce a 2DEG, so long as compensating acceptor levels are not present. The in-gap levels, on the other hand, were produced by vacancies on either surface termination (and they also form for vacancies in the bulk, i.e. as the second donor level, when polaronic effects are included) [101]. The in-gap spectral feature commonly observed using photoemission spectroscopy [96, 129], a technique which has a large probing area and a finite probing depth ( $\sim 20 \text{ \AA}$ ), likely is formed by a combination of these surface and bulk states. Also, by analyzing the nature of the wavefunction, we were also able to explain the absence of certain levels in the scanning tunneling spectrum.

# Chapter 5

## Transition metal trichalcogenides for 2D magnets

### 5.1 Introduction

Magnetism is one property still missing in the current line-up of 2D crystals. Most of the research towards this goal has tried to engineer magnetism in already existing 2D materials by external means, for example, doping and vacancies [130, 131]. But, as this magnetism is extrinsic in nature. Hence, the critical temperatures obtained are very small. Secondly, introducing defects and vacancies compromise the quality of the sample. To overcome these limitations, we started searching for 2D magnets. We explored the possibility of materials that are already magnetic in the bulk form, which can be made into 2D materials. In this regard, transition metal trichalcogenides (TMTC) such as  $\text{MnPS}_3$  represents a rather attractive material family. They have the chemical formula  $ABX_3$ , similar to the perovskites. But, in this case,  $A$  is the magnetic transition metal atom. Similar to dichalcogenides, these are layered compounds with weak interlayer Van der Waals interactions. Furthermore, these materials are known to exhibit a large variety of magnetic phases [132–137], making them ideal candidates for exfoliated 2D magnets. The successful fabrication of a truly 2D magnet would also significantly advance our understanding of low-dimensional magnetism.

Despite the obvious interest and more than three decades of experimental studies of bulk TMTC, magnetism in these materials remains to be fully understood. In particular, even though the spin wave measurement by inelastic neutron scattering has pointed out the importance of exchange interactions beyond nearest-neighbor (NN) spins [132, 138], relatively little is known about the nature of these interactions and their effect on the magnetic ground state. Additionally, the 2D confinement of electrons upon exfoliation often leads to properties quite different from the bulk crystals. It is thus interesting to ask whether there is any change of the magnetic

---

This chapter is adapted from N. Sivadas, M. W. Daniels, R. H. Swendsen, S. Okamoto, and Di Xiao, Physical Review B **91**, 235425 (2015). Copyright © 2015 American Physical Society.

ground state when these materials are thinned down to monolayers.

With these questions in mind, we investigate the magnetic ground states of monolayers of Mn- and Cr-based semiconducting TMTC, using first-principles calculations within the framework of density functional theory (DFT). The Mn-compounds (MnPS<sub>3</sub> and MnPSe<sub>3</sub>) are known to exhibit antiferromagnetic (AF) Néel order in their bulk form [132, 139], and are chosen here as benchmark for our calculations due to the extensively available experimental data. Interesting properties such as coupled spin and valley degrees of freedom have also been predicted for monolayers of these materials [140]. The Cr-compounds (CrSiTe<sub>3</sub> and CrGeTe<sub>3</sub>), on the other hand, are reported to be ferromagnetic (FM) in bulk [141–143], thus present a highly interesting system to realize 2D ferromagnets. One of the motivations of the present work is to provide some quantitative understanding of magnetism in these compounds.

Our main findings are summarized below. The majority of the chapter is focused on monolayers. We show that the second and third NN exchange interactions ( $J_2$  and  $J_3$ ) mediated through the  $p$  states of chalcogen anions are crucial in determining the magnetic ground state. Specifically, we find that monolayer CrSiTe<sub>3</sub> is an antiferromagnet with a zigzag spin texture due to significant contribution from  $J_3$ , whereas CrGeTe<sub>3</sub> a ferromagnet with a Curie temperature of 106 K. This result is in sharp contrast with previous theoretical studies in which only the NN exchange interaction ( $J_1$ ) was considered [144, 145]. We discuss the physical origin of various exchange interactions, and demonstrate that strain can be an effective knob for tuning the magnetic properties. A uniform in-plane tensile strain of  $\sim 3\%$  can tune the magnetic ground state of CrSiTe<sub>3</sub> from zigzag to ferromagnet, with a critical temperature of 111 K. We also find that in bulk CrSiTe<sub>3</sub>, the intralayer magnetic ordering is very sensitive to the out-of-plane lattice constant. For the experimental out-of-plane lattice constant (21.0 Å), the intralayer magnetic ordering is FM in nature. However, the interlayer coupling favors AF over FM coupling. This is in contradiction with experimental results. [141, 142] One possible reason for this discrepancy is discussed, but the actual mechanism for ferromagnetism in bulk CrSiTe<sub>3</sub> remains an open question.

## 5.2 Crystal and Magnetic Structure

Transition metal trichalcogenides with the chemical formula  $ABX_3$  are layered compounds with the structural space group of  $R\bar{3}$ , except MnPS<sub>3</sub>, which forms monoclinic crystals with the  $C2/m$  space group. In all compounds, the different layers are held together by weak van der Waals force. It has been predicted that the monolayer form of these materials are indeed stable [144, 146], making them attractive candidates for 2D magnets. Figure 5.1(a) and (b) show the crystal structure of TMTC monolayers. The magnetic ions ( $A$ ) form a honeycomb lattice within each layer, and each of them is octahedrally coordinated by six  $X$  atoms from its three neighboring ( $B_2X_6$ ) ligands, with the centers of the hexagons occupied by the  $B_2$  groups.

Similar to the crystal structure, the magnetic structure of bulk TMTC also shows

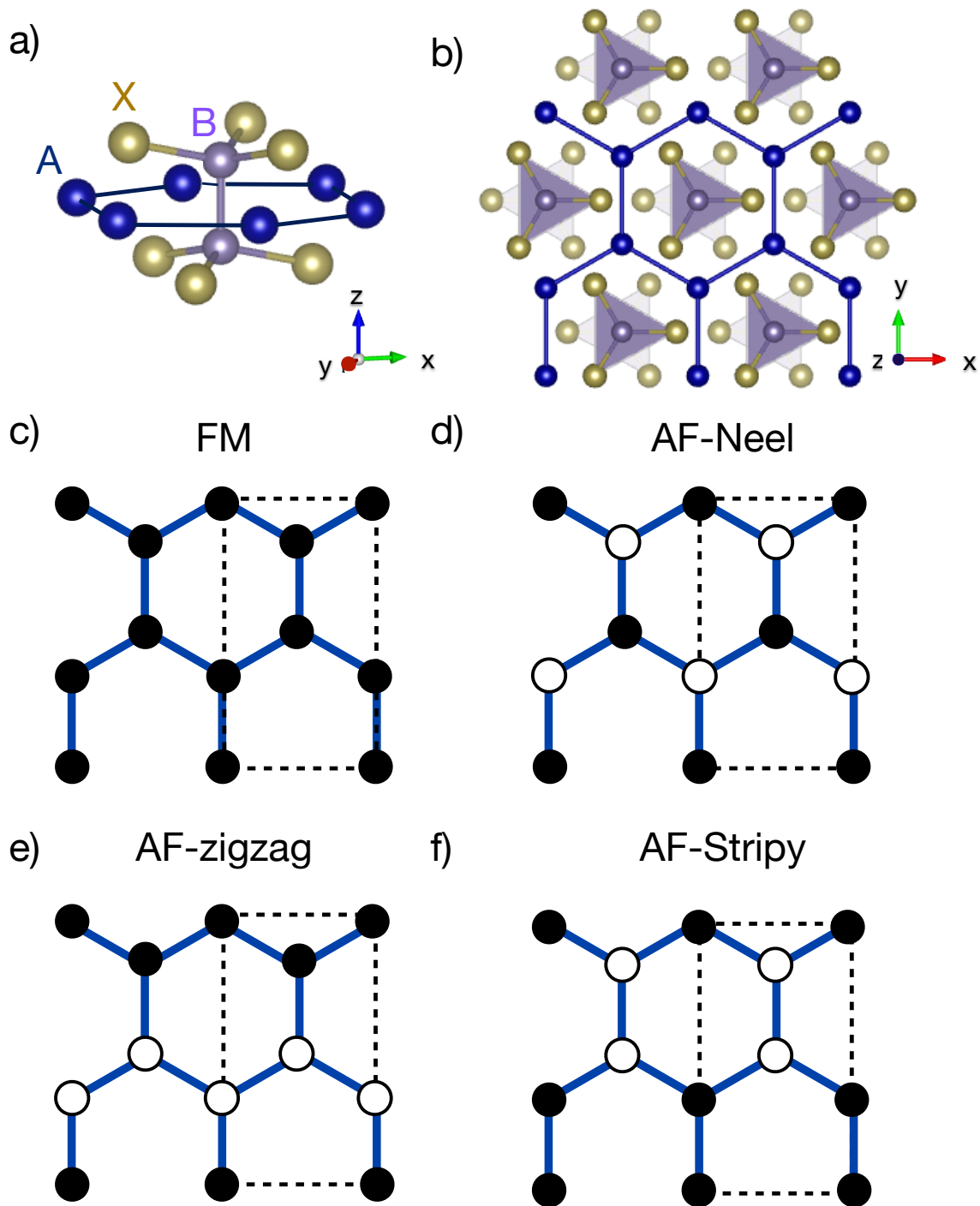


Figure 5.1: Crystal and magnetic structure of transition metal trichalcogenides  $ABX_3$ . The crystal structure (a) and the top view (b) of monolayers of  $ABX_3$ . The transition metal  $A$  atoms form a honeycomb structure with  $B_2X_6$  ligand occupying the interior of the honeycomb. Top view of the different spin configurations: the FM ordered (c), AF-Néel ordered (d), AF-zigzag ordered (e), AF-stripy ordered (f), with only the transition metal ions shown. Up (down) spins are represented by black filled-in (open) circles. The crystal structure is drawn using VESTA [1]

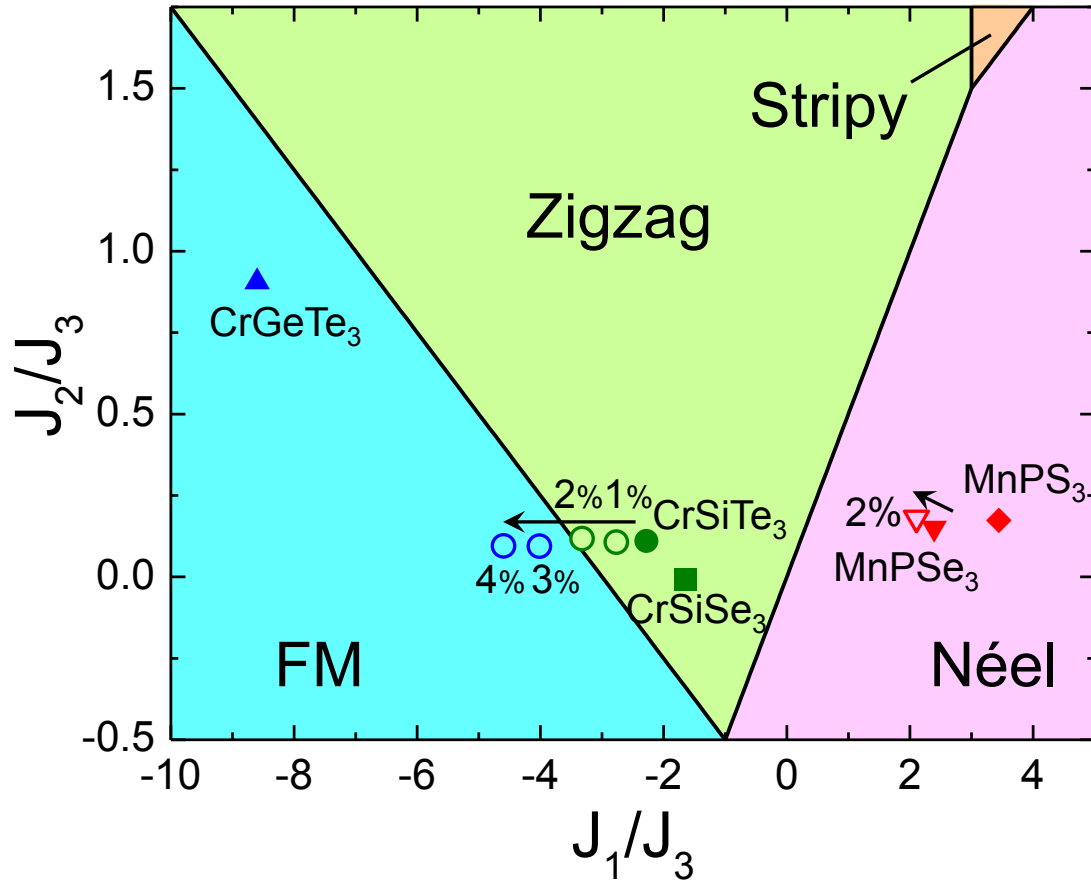


Figure 5.2: The ground state magnetic phase diagram for our spin model as a function of  $J_1/J_3$  and  $J_2/J_3$ . Since our calculation finds  $J_3$  to be always AF, only  $J_3 > 0$  is considered. Spins are treated as classical degrees of freedom. All compounds studied are located at corresponding parameter values. Open symbols are positions under tensile strains with arrows indicating the change from the unstrained cases.

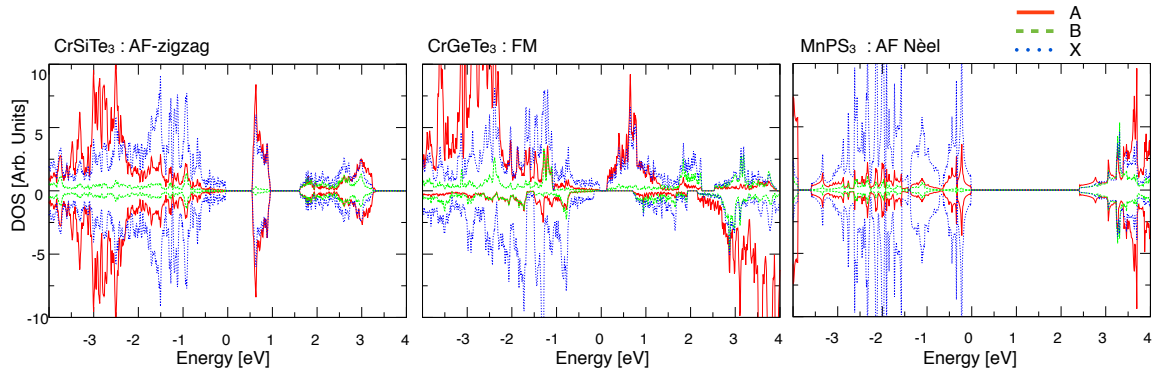


Figure 5.3: The partial density of states (PDOS) of the ground states of  $CrSiTe_3$  (AF-zigzag),  $CrGeTe_3$  (FM) and  $MnPS_3$  (AF-Néel) are shown in (a), (b) and (c) respectively. These are the three unique ground states exhibited by the  $ABX_3$  compounds. The PDOS of  $A$ ,  $B$  and  $X$  are shown using red lines, broken green lines and dotted blue lines respectively. We observe considerable hybridization between the transition metal ( $A$ ) atoms and the chalcogen ( $X$ ) atoms.

2D characteristics. It can be understood as FM or AF coupled 2D magnetic layers. To describe the 2D magnetic structure, we consider the Heisenberg model on a honeycomb lattice,

$$H = \sum_{\langle ij \rangle} J_1 \vec{S}_i \cdot \vec{S}_j + \sum_{\langle\langle ij \rangle\rangle} J_2 \vec{S}_i \cdot \vec{S}_j + \sum_{\langle\langle\langle ij \rangle\rangle\rangle} J_3 \vec{S}_i \cdot \vec{S}_j . \quad (5.1)$$

where  $J_{1,2,3}$  are the exchange interactions between NN, second NN, and third NN spins. Previous studies have shown that it is necessary to include both  $J_2$  and  $J_3$  to fit the spin wave dispersion from inelastic neutron scattering data [132, 138]. In addition, considering only  $J_1$  would yield either FM or AF-Néel order, while other magnetic ground states have been found experimentally. To compute the exchange interactions, we consider the following four possible magnetic ground state: FM, AF-Néel, AF-zigzag, and AF-stripy, as shown in Fig. 5.1 (c)-(f). The ground-state phase diagram for our model in Eq. (1) is shown in Fig. 5.2 as a function of  $J_1/J_3$  and  $J_2/J_3$ . Here  $J_3$  is assumed to be positive, as it turns out to be the case for all the compounds we studied. It is clear that not only  $J_1$ , but also  $J_2$  and  $J_3$  play an important role in deciding the magnetic ground state.

## 5.3 Results and discussion

### 5.3.1 Computation details

With the above observation, the magnetic ground states of  $ABX_3$  compounds are examined using DFT employing the projector augmented wave[60, 147, 148] method encoded in Vienna *ab initio* simulation package [60] with the generalized gradient approximation in the parameterization of Perdew, Burke and Enzerhof [149, 150]. We use Hubbard  $U$  terms (4 eV for Cr and 5 eV for Mn) [151, 152] to account for strong electronic correlations as suggested by Dudarev *et al.* [153]. Our results were qualitatively insensitive to the different  $U$ 's chosen (2 eV, 4 eV) for the Cr-compounds. For each slab a vacuum region more than 15 Å was used. A cutoff energy of 400 eV and a Monkhorst-Pack special  $k$ -point mesh of  $24 \times 14 \times 1$  for the Brillouin zone integration was found to be sufficient to obtain the convergence. Structural optimizations were performed by fixing the in-plane lattice constants to that of the theoretical bulk lattice constants (see Table I). All ions were then relaxed with the relaxation of the electronic degrees of freedom accurate to up to  $10^{-6}$  eV.

### 5.3.2 Exchange interactions

For each compound, we optimize the crystal structure for all four spin configurations [see Fig. 5.1 (c)-(f)] to find the lowest-energy state. Figure 5.3 shows the partial density of states (DOS) of three representative ground states: AF-zigzag (CrSiTe<sub>3</sub>),

Table 5.1: Lattice constant  $a$ , magnetic ground state (GS), exchange coupling constants, and magnetic critical temperature for  $ABX_3$  studied. Critical temperatures are obtained from classical Monte Carlo simulations.

	$a$ (Å)	GS	$J_1$ (meV)	$J_2$ (meV)	$J_3$ (meV)	$T_c$ (K)
MnPS <sub>3</sub> (exp) [132]	5.88	Néel	0.77	0.07	0.18	164
MnPS <sub>3</sub>	5.88	Néel	0.79	0.04	0.23	231
MnPSe <sub>3</sub>	6.27	Néel	0.46	0.03	0.19	147
MnPSe <sub>3</sub> (2% strain)	6.40	Néel	0.33	0.03	0.16	115
CrSiSe <sub>3</sub>	6.29	Zigzag	-0.74	0.0	0.43	92
CrSiTe <sub>3</sub>	6.84	Zigzag	-1.63	0.08	0.71	160
CrSiTe <sub>3</sub> (1% strain)	6.91	Zigzag	-1.82	0.07	0.66	130
CrSiTe <sub>3</sub> (2% strain)	6.98	Zigzag	-1.99	0.07	0.60	72
CrSiTe <sub>3</sub> (3% strain)	7.04	FM	-2.16	0.05	0.54	111
CrSiTe <sub>3</sub> (4% strain)	7.11	FM	-2.29	0.05	0.50	158
CrGeTe <sub>3</sub>	6.91	FM	-1.88	0.20	0.22	106

FM (CrGeTe<sub>3</sub>) and AF-Néel (MnPS<sub>3</sub>). It is evident that there is considerable hybridization between the chalcogen  $p$  states and the transition metal  $d$  states, further confirming the necessity to include the second and the third NN interaction into consideration. By integrating the partial DOS in the transition metal atoms for the lowest energy spin configuration we obtain  $S_i = 2.45$  for Mn-compounds and 2.10 for Cr-compounds, with the spins having a variation less than 0.01 between the different spin configurations.

To further extract the  $J$ 's, we chose to fix the lattice to that of the most energetically favorable spin configuration and computed the energies for different spin configurations. The exchange coupling constants were derived by mapping the DFT energies to the Heisenberg spin Hamiltonian (5.1),

$$\begin{aligned}
 E_{\text{FM/Néel}} &= E_0 + (\pm 3J_1 + 6J_2 \pm 3J_3) |\vec{S}|^2, \\
 E_{\text{AF-zigzag/stripy}} &= E_0 + (\pm J_1 - 2J_2 \mp 3J_3) |\vec{S}|^2,
 \end{aligned}
 \tag{5.2}$$

where  $E_0$  is the ground state energy independent of the spin configuration. Using these  $J$ 's, we also calculated the critical temperature by performing a Monte Carlo simulation of an Ising model on the 2D honeycomb lattice [154].

The magnetic ground state, the computed  $J$ 's, along with the critical temperature for each compound are listed in Table I. The locations of the ground state of all the compounds studied are labeled in the phase diagram in Fig. 5.2. We see that both MnPS<sub>3</sub> and MnPSe<sub>3</sub> are deep inside the AF-Néel phase. The calculated values of  $J_{1,2,3}$  for monolayer MnPS<sub>3</sub> agree excellently with the experimental data for the bulk system [132], which validates our calculation. We also find that both CrSiTe<sub>3</sub>

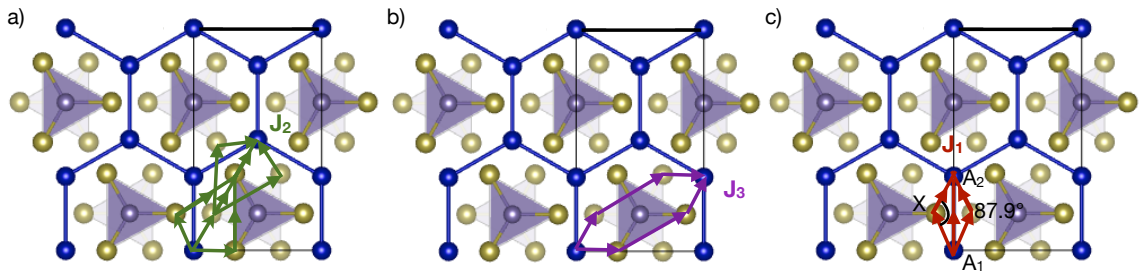


Figure 5.4: Top view of monolayer of  $ABX_3$ . Blue, violet and yellow represents  $A$ ,  $B$  and  $X$  ions respectively. The five possible paths for second NN interaction is show in (a) and the third NN interaction is shown in (b). The two different NN hopping paths between two transition metal atoms at different sites ( $A_1$  and  $A_2$ ) are shown in (c) with the direct exchange as a hopping between the transition metal orbitals and the superexchange interaction characterized by hopping between the transition metals through the  $X$  atom.

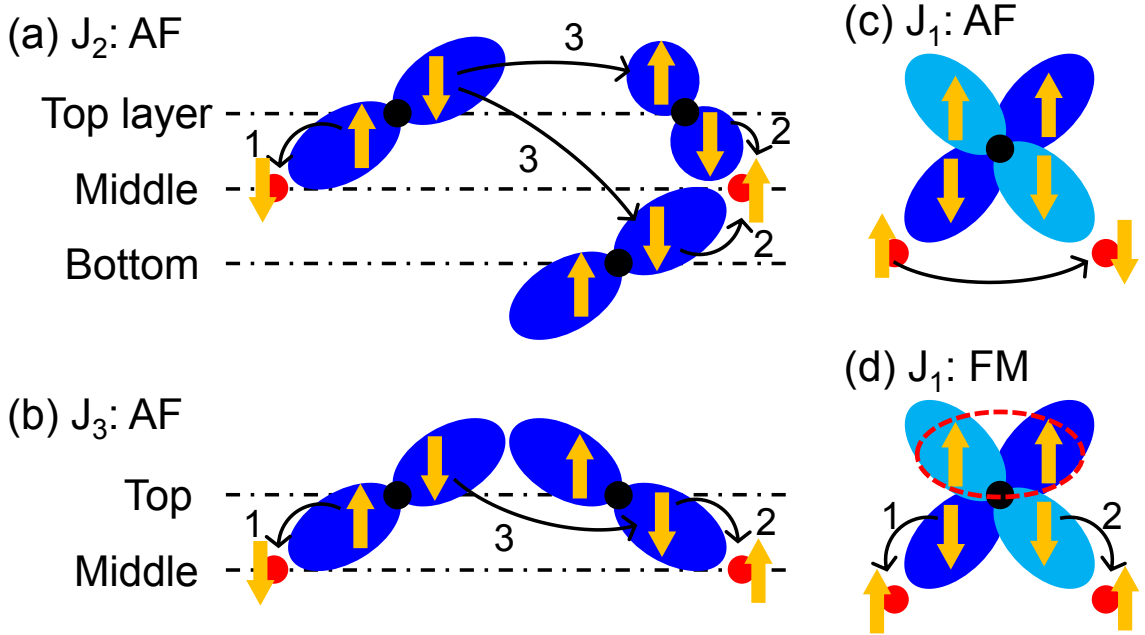


Figure 5.5: Main contributions of virtual electron excitations to magnetic interactions. Virtual electron excitations from two  $X$  anions to a pair of (a) second NN and (b) third NN  $A$  ions. (c) Direct excitations between neighboring TM ions (red dots), resulting in AF  $J_1$ . (d) Excitations from two orthogonal orbitals on a  $X$  anion (black dots) to a neighboring pair of  $A$  ions. Because of the Hund coupling acting in excited states as indicated by a broken circle, this process gives rise to FM  $J_1$ . The actual sign of exchange interactions results from the competition between FM and AF contributions for  $J_1$ . Numbers indicate the typical order of the first half perturbation processes for each contribution.

and  $\text{CrSiSe}_3$  are in the AF-zigzag phase with the former lying close to the boundary of AF-zigzag and FM phase. This is different from the FM ground state reported for bulk  $\text{CrSiTe}_3$  [141, 142], which will be addressed later. Finally, of all the compounds studied,  $\text{CrGeTe}_3$  is the only one that has a FM ground state in its unstrained monolayer form.

We note that  $J_3$  is significantly large. This corroborates the decision to include more than just the NN interaction. Ignoring it (and  $J_2$ ) had previously yielded a different ground state (FM) for  $\text{CrSiTe}_3$  monolayers in previous studies [144, 145]. In our calculation for monolayer  $\text{CrSiTe}_3$ , FM is indeed lower in energy than AF-Néel. The energy difference between the two magnetic states was found to be similar to what was reported in Li *et al.* [144], when the same  $U$  was chosen. But crucially, we find that AF-zigzag is even lower in energy than FM, and hence is the magnetic ground state.

Now that we have shown that the interactions have to be included up to the third NN not only to interpret the neutron diffraction data, but also to get the correct magnetic ground state, the imminent task is to understand the microscopic origin of the different  $J$ 's. We first note that  $J_2$  and  $J_3$  are always AF. Furthermore, the value of  $J_2$  is found to be smaller than  $J_3$ . Both of these findings are consistent with previous reports on MnPS<sub>3</sub> and its Fe derivative, FePS<sub>3</sub> [132, 138]. These observations can be understood by analyzing the crystal structure. Figure 6.3 shows the possible hybridization paths connecting  $A$  site ions. For the second NN and the third NN  $A$  site pairs, electrons hop through two  $X$  anions [Fig. 6.3 (a) and (b)]. For this reason,  $J_2$  and  $J_3$  might be regarded as super-superexchange interactions. Based on the geometry and the  $X$  anion  $p$  states, we expect  $J_2$  to be weakly AF because it involves small  $X$ - $X$  hybridizations [Fig. 5.5 (a)]. On the other hand,  $J_3$  involves two  $X$  anions on the same plane, either top layer or bottom layer. Hence, there is strong hybridization of the  $p$  states [Fig. 5.5 (b)], resulting in a strongly AF  $J_3$ .

The NN exchange  $J_1$ , on the other hand, shows a large variation from compound to compound. The variation is so large that it even changes the sign going from the Mn compounds to the Cr compounds (see Table I). This behavior comes from a unique crystal structure, which naturally gives rise to two competing interactions, i.e., the direct exchange and superexchange. The direct exchange originates from direct electron hopping between the NN  $A$  sites [see Figs. 6.3 (c) and 5.5 (c)]. For the Mn compounds, this exchange is robustly AF as the Mn ions are in the half-filled high-spin  $d^5$  state. For the Cr compounds, the AF direct exchange is weakened by a FM component as Cr ions have partially-filled  $d$  shell [155]. The superexchange interaction is mediated through the  $X$  ions [see Fig. 6.3 (c)]. As the  $A_1$ - $X$ - $A_2$  angle is close to  $90^\circ$ , this interaction is FM [156, 157]. It is important to note that for the superexchange interaction two electrons must excite from  $X$  anion  $p$  states to neighboring  $A$   $d$  states [see Fig. 5.5 (d)]. Since the electron excitation energy is large for the Mn compounds [Fig.5.3(c)], reflecting closed  $d$  shell on Mn ions, the superexchange is expected to play a minor role compared with the direct exchange. On the other hand for the Cr compounds, the superexchange could play a dominant role.

To confirm the distinct role of the superexchange mechanism's contribution to  $J_1$ , we examine the magnetization of a chalcogen ion between two ferromagnetically coupled transition metal ions as its magnitude is a good indication of the strength of the superexchange interaction [158]. Our DFT calculation for the Cr compounds in the FM metastable state showed the total magnetization of the chalcogen ions is  $\sim 0.6 \mu_B$  per unit cell and hence significant. On the other hand, for the Mn compounds, the magnetization of the chalcogen ions are an order of magnitude smaller, which is consistent with our finding of an AF  $J_1$ , and the presence of a large electron excitation energy from  $X$   $p$  to Mn  $d$ . The net result is that  $J_1$  becomes AF for Mn compounds because of the dominance of AF direct exchange over the FM superexchange, while the FM superexchange wins over the AF direct exchange making  $J_1$  strongly FM for

Cr compounds (see Table I). Hence, depending on the transition metal ions involved, a significant competition is expected between FM and AF components, which could lead to a plethora of magnetic states.

### 5.3.3 Effect of strain

This competition is further verified by applying a uniform tensile strain on MnPSe<sub>3</sub> and CrSiTe<sub>3</sub>. It is important to note that both direct exchange and superexchange do not change sign as we strain the system, but the former decreases more rapidly than the latter as the atomic distances increase by a tensile strain. As a consequence,  $|J_1|$  for MnPSe<sub>3</sub> decreases with strain, where as  $|J_1|$  for CrSiTe<sub>3</sub> increases with strain (see Table I). This confirmed the presence of competing exchange interactions.

This result immediately suggests the possibility of tuning the magnetic ground state using strain. Here, we consider monolayer CrSiTe<sub>3</sub> as our prototype system and use strain as a knob to change the different  $J$ 's. CrSiTe<sub>3</sub> is an ideal candidate for this study as it lies close to the FM and AF-zigzag phase boundary. With a tensile strain,  $J_2$  and  $J_3$  are both expected to decrease in magnitude as the atomic distances are increased. While the effect of strain on  $J_1$  is subtler, it is expected to increase in magnitude for small strains. Not surprisingly, an application of  $\sim 3\%$  strain leads to a magnetic phase transition with ferromagnetism becomes the magnetic ground state (see Fig. 5.2). Strain also has a direct impact on the critical temperatures. Once the FM ground state is realized, the critical temperature  $T_c$  can be further enhanced with strain. As shown in Table I,  $T_c$  goes up to 158 K for  $\sim 4\%$  strain. With this strong dependence of critical temperature on the applied strain, it might be even possible to engineer room temperature ferromagnetic behavior, for large values of strain [145].

### 5.3.4 Bulk magnetic order

So far we have only considered the magnetic properties of monolayer TMTCs. One of the important finding is that monolayer of CrSiTe<sub>3</sub> has an AF-zigzag ground state, whereas in bulk it is reported to be FM from neutron scattering experiments [141, 142]. To understand this change in magnetic structure when we go from monolayer to bulk, we calculated the magnetic ground state of bulk CrSiTe<sub>3</sub>. We find that for the experimental out-of-plane lattice constant (21.0 Å), the intralayer magnetic ordering is FM in nature and not AF-zigzag. This switching of the intralayer magnetic ordering from AF-zigzag to FM as we go from monolayer to bulk is very sensitive to the out-of-plane lattice constant of the bulk system. If we increase the out-of-plane lattice constant to 22.8 Å, the intralayer coupling prefers AF-zigzag. This is because bulk CrSiTe<sub>3</sub> has *ABC* stacking, thus an in-plane AF-zigzag spin configuration costs more energy compared to a FM spin configuration when the interlayer exchange interaction becomes strong.

However, we also find that in bulk, AF interlayer coupling is preferred over FM

interlayer coupling by 10.6 meV per Cr atom. Analyzing the interlayer interactions between the Cr atoms, it is dominated by super-superexchange. Based on the geometry and because of the presence of large chalcogen atoms, we expect this interaction to be comparable to  $J_3$  and hence significant. As the mechanism for interlayer super-superexchange coupling is similar to that of the intralayer super-superexchange coupling previously discussed for  $J_2$  and  $J_3$ , it is not surprising that these interactions are AF in nature. But this contradicts experimental findings of bulk ferromagnetism in CrSiTe<sub>3</sub> [141, 142].

One possible source for this discrepancy is the absence of the dipole-dipole interaction in DFT calculations, as discussed previously [159, 160]. By introducing the spin-orbit coupling, we have confirmed that there is an out-of-plane easy axis anisotropy, in accordance with experiments [141, 142]. With this easy axis, the interlayer FM arrangement can become energetically more favorable than the AF arrangement, because of the dipole-dipole interaction [160]. We also note that for MnPS<sub>3</sub> the dipole-dipole interaction is negligible due to the AF ordering within each plane. This could explain why our DFT results show excellent agreement with the bulk experimental results for the Mn compounds. Nonetheless, the actual mechanism for ferromagnetism in bulk CrSiTe<sub>3</sub> remains an open question.

## 5.4 Summary

In this chapter, we studied the magnetic properties of monolayers of van der Waals transition-metal trichalcogenides  $ABX_3$  using density functional theory. In order to understand the rich magnetic behavior observed in these systems, we derived local spin models using the DFT energy of the magnetic ground state and metastable excited states. Because of the extended nature of the  $p$  state of the chalcogen atoms, second nearest-neighbor and third nearest-neighbor interactions are found to play significant roles. Specifically, we find that monolayer CrSiTe<sub>3</sub> is an antiferromagnet with a zigzag spin texture due to significant contribution from  $J_3$ , whereas CrGeTe<sub>3</sub> is a ferromagnet with a Curie temperature of 106 K. Detailed analyses on the magnetic interactions led us to predict that monolayers CrSiTe<sub>3</sub> can be made ferromagnetic with the application of a moderate uniform in-plane tensile strain of 3%, which is experimentally feasible. Our studies demonstrate transition-metal trichalcogenides  $ABX_3$  are possible candidates for spintronic applications; especially CrGeTe<sub>3</sub> and strained CrSiTe<sub>3</sub> are promising for two-dimensional ferromagnetic semiconductors. The magnetic ordering of bulk CrSiTe<sub>3</sub>, however, remains an open question.

# Chapter 6

## Magneto-optic effects in 2D magnets

### 6.1 Introduction

Magneto-optic effects are one of the defining features of time-reversal ( $\mathcal{T}$ ) symmetry breaking in matter. Usually, the  $\mathcal{T}$  symmetry is broken either by an external magnetic field, or by the spontaneous appearance of a macroscopic magnetization such as in ferromagnets. Similar to their ferromagnetic counterparts, the  $\mathcal{T}$  symmetry is also broken in antiferromagnets. However, because of their vanishing net magnetization one would naively expect an absence of magneto-optic effects in antiferromagnets. This assumption has been recently challenged by the theoretical demonstration of a rather large magneto-optic Kerr effect (MOKE) in certain non-collinear antiferromagnets with zero net magnetization [161]. This effect is closely related to the anomalous Hall effect predicted in the same class of materials [162, 163], both of which are dictated by the absence of certain crystal symmetries. The appearance of magneto-optic effects in antiferromagnets is of intrinsic interest, since it would allow direct detection of the magnetic order and therefore could be useful for antiferromagnets-based memory devices [164].

While non-collinear antiferromagnets have been the focus of recent interest [161–163], we show that magneto-optic effects can also exist in the more commonly available collinear antiferromagnets. We start by analyzing the general symmetry requirements for magneto-optic effects, and demonstrate the symmetry principles by constructing a tight-binding model with a collinear Néel type order. We show that, contrary to the general belief, lifting the spin degeneracy of the energy bands is not a sufficient condition to generate magneto-optic effects; it is the crystal symmetry that actually controls these effects.

Based on this understanding, we predict that a perpendicular electric field can

---

This chapter is adapted from N. Sivadas, S. Okamoto, and Di Xiao, arXiv:1607.02156

be used to generate and control the MOKE in layered antiferromagnets using first-principles calculations. Recent theoretical and experimental progress has identified several layered compounds as promising candidates to host magnetism in their thin-film limit [47, 140, 165–168]. One of them is MnPSe<sub>3</sub>, a semiconductor with collinear antiferromagnetic order within each layer. We show that the field-induced inversion ( $\mathcal{I}$ ) symmetry breaking in bilayer MnPSe<sub>3</sub> gives rise to a MOKE whose direction of rotation can be switched by the reversal of the gate voltage. For field strength of 0.4 V/nm, the MOKE rotation angle is found to be as large as 4 mrad. Our result indicates that layered antiferromagnets would provide a very promising platform to explore gate-controllable magneto-optic effects.

## 6.2 Results and discussion

### 6.2.1 Symmetries

As symmetries play an important role in magneto-optic effects [169], we begin our discussion with a general symmetry analysis. Magneto-optic effects are closely related to the AC Hall effect [see Eq. (6.5) below], which refers to the appearance of a transverse AC current in response to an optical field in the longitudinal direction. Therefore, we can use the following pseudo-vector

$$\mathbf{n} = \mathbf{j} \times \mathbf{E} \quad (6.1)$$

to characterize magneto-optic effects. If the material possesses  $\mathcal{T}$  symmetry,  $\mathbf{n}$  is clearly constrained to be zero. Both ferromagnets and antiferromagnets break  $\mathcal{T}$  symmetry. However, it is possible that the material might have a combined symmetry of  $\mathcal{T}$  and some crystal symmetry  $\mathcal{O}$ , which can force  $\mathbf{n}$  to be zero even if  $\mathcal{T}$  symmetry is broken. To elucidate this, consider an antiferromagnets with  $\mathcal{TI}$  symmetry. One such example is shown in Fig. 6.1(a). Under  $\mathcal{TI}$  symmetry,  $\mathbf{j}$  is unaffected, whereas  $\mathbf{E}$  changes sign. It then follows from Eq. (6.1) that  $\mathbf{n}$  changes sign under the  $\mathcal{TI}$  symmetry operation. This forces  $\mathbf{n}$  to be zero and suppresses any magneto-optic effects. Using a similar analysis, it is straightforward to show that for two-dimensional systems both  $\mathcal{TM}_z$  symmetry and  $\mathcal{TC}_2$  symmetry also suppress magneto-optic effects, where  $\mathcal{M}_z$  is the mirror reflection perpendicular to the  $\mathbf{j}$ - $\mathbf{E}$  plane, and  $\mathcal{C}_2$  is the in-plane inversion symmetry. Thus, by breaking these crystal symmetries, magneto-optic effects can be generated in antiferromagnets. This is the key to our gate controllable MOKE.

### 6.2.2 Tightbinding model

Armed with the above insight, we now consider a specific example, a honeycomb lattice with a collinear Néel type order, as shown in Fig. 6.1(a). The Hamiltonian is

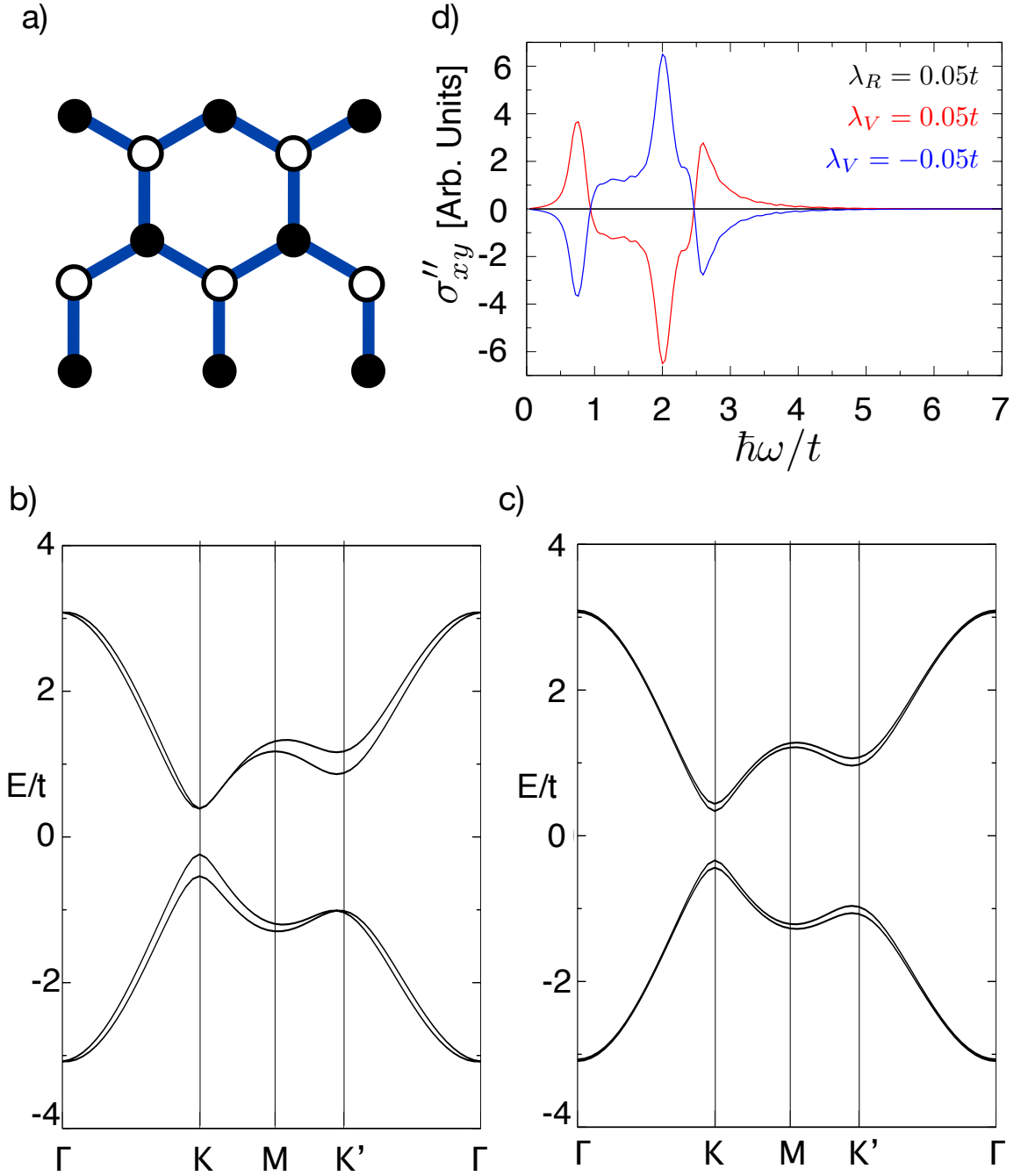


Figure 6.1: (a) Schematic of a honeycomb lattice with collinear Néel order. Up (down) spins are represented by filled (open) circles. The system possesses combined  $\mathcal{TI}$  symmetry although both  $\mathcal{T}$  and  $\mathcal{I}$  symmetries are individually broken. (b) and (c) Energy bands of the tight-binding model with broken mirror symmetry ( $\lambda_R = 0.05t$ ,  $\lambda_V = 0$ ) and broken in-plane inversion symmetry ( $\lambda_R = 0$ ,  $\lambda_V = 0.05t$ ), respectively. In both cases,  $\lambda_{SO} = 0.06t$  and  $\lambda_M = 0.7t$ . The spin degeneracy of the bands is lifted in both cases. (d) The imaginary part of the optical Hall conductivity ( $\sigma''_{xy}$ ) computed for  $\lambda_R = 0.05t$  (black),  $\lambda_V = 0.05t$  (red) and  $\lambda_V = -0.05t$  (blue).  $\sigma''_{xy}$  is zero when only  $\lambda_R$  is turned on and becomes non-zero when  $\lambda_V \neq 0$ . As the sign of  $\lambda_V$  is reversed so is  $\sigma''_{xy}$ . The smearing parameter was set to  $0.1t$ .

given by

$$H = t \sum_{\langle ij \rangle} c_i^\dagger c_j + i\lambda_{SO} \sum_{\langle\langle ij \rangle\rangle} \nu_{ij} c_i^\dagger s^z c_j + \sum_i (-1)^i \lambda_M c_i^\dagger s^z c_i. \quad (6.2)$$

The first term is the nearest neighbor hopping. The second term is the intrinsic spin-orbit coupling (SOC), which is needed for any magneto-optic effects. Here,  $\nu_{ij} = (2/\sqrt{3})(\hat{\mathbf{d}}_1 \times \hat{\mathbf{d}}_2)_z = \pm 1$ , where  $\hat{\mathbf{d}}_1$  and  $\hat{\mathbf{d}}_2$  are the unit vectors of the two bonds connecting site  $i$  to  $j$ , and  $s^z$  is the spin Pauli matrix. Along with preserving the  $\mathcal{M}_z$  symmetry, this term also preserves both  $\mathcal{T}$  and  $\mathcal{I}$  symmetries. The third term breaks  $\mathcal{T}$  symmetry via a staggered Zeeman field, mimicking the Néel order with an out-of-plane easy axis. We note that this term can be dynamically generated by local interactions,  $\sum_i U n_{i,\uparrow} n_{i,\downarrow}$  [170, 171]. Within the mean-field approximation,  $U$  and  $\lambda_M$  are related by  $\lambda_M = \frac{m}{2}U$  where  $m = \langle n_{i,\uparrow} - n_{i,\downarrow} \rangle$  is the spontaneous magnetic moment. Thus, our results are also valid for interacting systems with robust magnetic ordering. One can verify that the system is invariant under the  $\mathcal{T}\mathcal{I}$  symmetry. This Hamiltonian is identical to the one proposed by Kane and Mele for the quantum spin Hall effect [172], except the  $\lambda_M$  term. As we are interested in the properties of a topologically trivial antiferromagnetic insulator, we will work in the strong exchange limit where the band gap is dominated by  $\lambda_M$  ( $\lambda_M \gg 3\sqrt{3}\lambda_{SO}$ ).

To analyze the role of crystal symmetries, we add two symmetry breaking terms to the Hamiltonian

$$H' = i\lambda_R \sum_{\langle ij \rangle} c_i^\dagger (\mathbf{s} \times \hat{\mathbf{d}}_{ij})_z c_j + \lambda_V \sum_i (-1)^i c_i^\dagger c_i. \quad (6.3)$$

The Rashba SOC term ( $\lambda_R$ ) breaks the  $\mathcal{M}_z$  symmetry, and the staggered sublattice potential ( $\lambda_V$ ) breaks the in-plane inversion symmetry. Figure 6.1(b) and (c) show the energy bands obtained for two representative cases where the  $\mathcal{T}\mathcal{I}$  symmetry is broken. In cases I we switch on only the Rashba term ( $\lambda_R \neq 0$ ), whereas in case II only the staggered sublattice potential is turned on ( $\lambda_V \neq 0$ ). It is clear that the effect of these  $\mathcal{T}\mathcal{I}$  symmetry breaking terms is to lift the spin degeneracy of the bands. We also note that  $K$  and  $K'$  valleys are no longer degenerate. This is not a consequence of  $\mathcal{T}\mathcal{I}$  symmetry breaking, and in fact, they remain non-degenerate even when the symmetry breaking terms are removed. The breaking of the valley degeneracy arises from the interaction of the antiferromagnetic order and the intrinsic SOC [140].

Next, we calculated the optical Hall conductivity  $\sigma_{xy}(\omega)$  using the Kubo-Greenwood formula [173, 174],

$$\begin{aligned} \sigma_{xy}(\omega) = & \hbar e^2 \int \frac{d^2k}{(2\pi)^2} \sum_{n \neq m} (f_{m\mathbf{k}} - f_{n\mathbf{k}}) \\ & \times \frac{\text{Im} \langle \psi_{n\mathbf{k}} | v_x | \psi_{m\mathbf{k}} \rangle \langle \psi_{m\mathbf{k}} | v_y | \psi_{n\mathbf{k}} \rangle}{(\varepsilon_{m\mathbf{k}} - \varepsilon_{n\mathbf{k}})^2 - (\hbar\omega + i\eta)^2}, \end{aligned} \quad (6.4)$$

where  $f_{m\mathbf{k}}$  is the Fermi-Dirac distribution function,  $\varepsilon_{m\mathbf{k}}$  is the energy of the  $m$ th band,  $\hbar\omega$  is the photon energy, and  $\eta$  is an adjustable smearing parameter with units

of energy. For detailed derivation, refer to Ref. [55]. Figure 6.1(d) shows the imaginary part of  $\sigma_{xy}$ , denoted by  $\sigma''_{xy}$ . Even though the bands are spin-split in both cases, we can see that  $\sigma''_{xy}$  is identically zero for case I and is non-zero only for case II. To understand this we further analyze the symmetry properties of the system. We note that even though the system is invariant under  $\mathcal{TI}$ , the  $\mathcal{TM}_z$  symmetry is already broken by the out-of-plane magnetic order. In case I, although the Rashba term breaks  $\mathcal{M}_z$  symmetry, the system still possesses  $\mathcal{TC}_2$  symmetry. As we discussed before, it suppresses any magneto-optic effects. This shows that even though the bands are spin-split, the underlying crystal symmetries can force the magneto-optic effects to vanish. In case II, the staggered sublattice potential breaks both  $\mathcal{TI}$  and  $\mathcal{TC}_2$  symmetries, it therefore lifts all symmetry constraints on magneto-optic effects, making it non-zero.

In addition, we also find that upon the reversal of the staggered sublattice potential,  $\sigma''_{xy}$  changes its sign. It can be verified that the process of reversing the sign of the staggered sublattice potential is equivalent to switching the sublattices and reversing the spins. This operation is nothing but the  $\mathcal{TI}$  symmetry operation. However, we have already discussed that  $\mathcal{TI}$  symmetry operation reverses the sign of  $\sigma_{xy}$ , which is indeed what we find. On the other hand, if natural birefringence also exist in the system, their contribution would not flip sign upon the reversal of the sublattice potential. This property can be used to distinguish between magneto-optical effects and natural birefringence.

While crystal symmetries are difficult to control in bulk materials, it has been demonstrated that gating can be an effective tool to break the inversion symmetry in 2D materials [29–33]. In the following we demonstrate the idea of gate-controllable MOKE using bilayer MnPSe<sub>3</sub> as an example.

### 6.2.3 Gate-controllable MOKE

#### Methodology

The calculations for the first-principles part was performed using the projector augmented wave [60, 147, 148] method encoded in Vienna *ab initio* simulation package (VASP) [60] with the generalized gradient approximation in the parameterization of Perdew, Burke and Enzerhof [149, 150]. We use Hubbard  $U$  terms 5 eV for Mn [151, 152] to account for strong electronic correlations as suggested by Dudarev *et al* [153]. The shell configuration of [Ar]  $3d^6 4s^1$ , [Ne]  $3s^2 3p^3$ , and [Ar]  $4s^2 4p^4$  were used for Mn, P and Se, respectively. Structural optimization was performed by fixing the in-plane lattice constants to that of the theoretical bulk lattice constants. A vacuum region more than 15 Å was used in all cases. All the ions were then relaxed with the Mn-Mn interlayer distance kept fixed. We do not expect this to alter our conclusions.

The effect of an external electric field in the slab geometry was calculated self-consistently at the first-principles step, using the EFIELD-tag in VASP. This adds

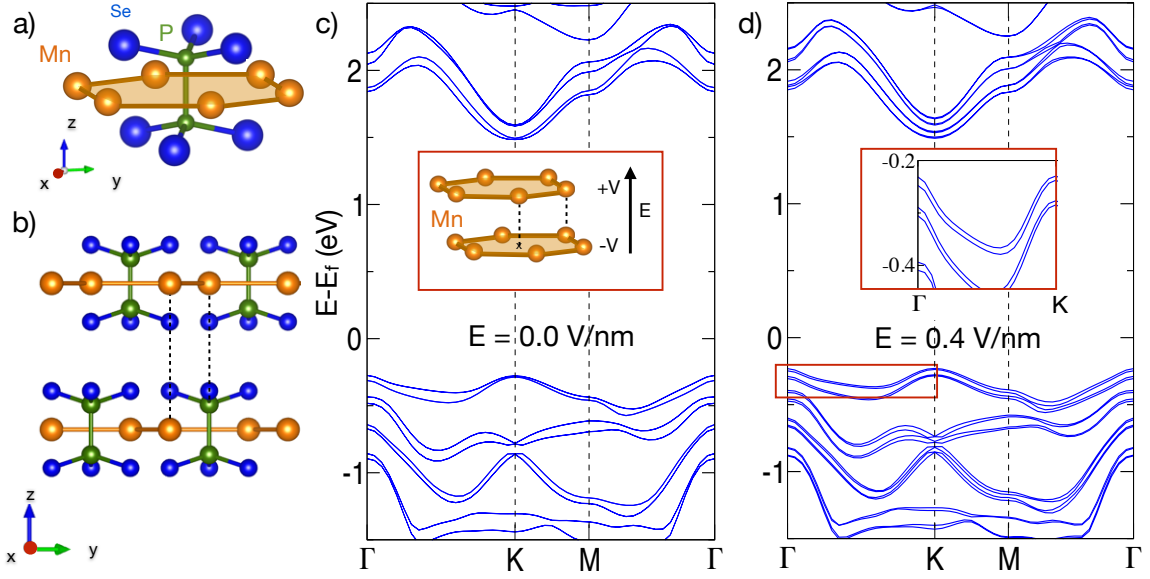


Figure 6.2: (a) The crystal structure of monolayers of MnPSe<sub>3</sub>. The transition metal Mn atoms form a honeycomb structure with P<sub>2</sub>Se<sub>6</sub> ligand occupying the center of the honeycomb. (b) The side view of the crystal structure of bilayer MnPSe<sub>3</sub>. The crystal structure is drawn using VESTA [1]. (c) The band structure of the bilayer MnPSe<sub>3</sub> in the absence of an electric field. The insert shows the Mn atoms in the bilayer. (d) The band structure of the bilayer MnPSe<sub>3</sub> in the presence of an electric field (0.4 V/nm) along the  $z$ -direction. The insert shows the lifting of the spin degeneracy of the bands due to the  $\mathcal{TI}$  symmetry breaking by the field.

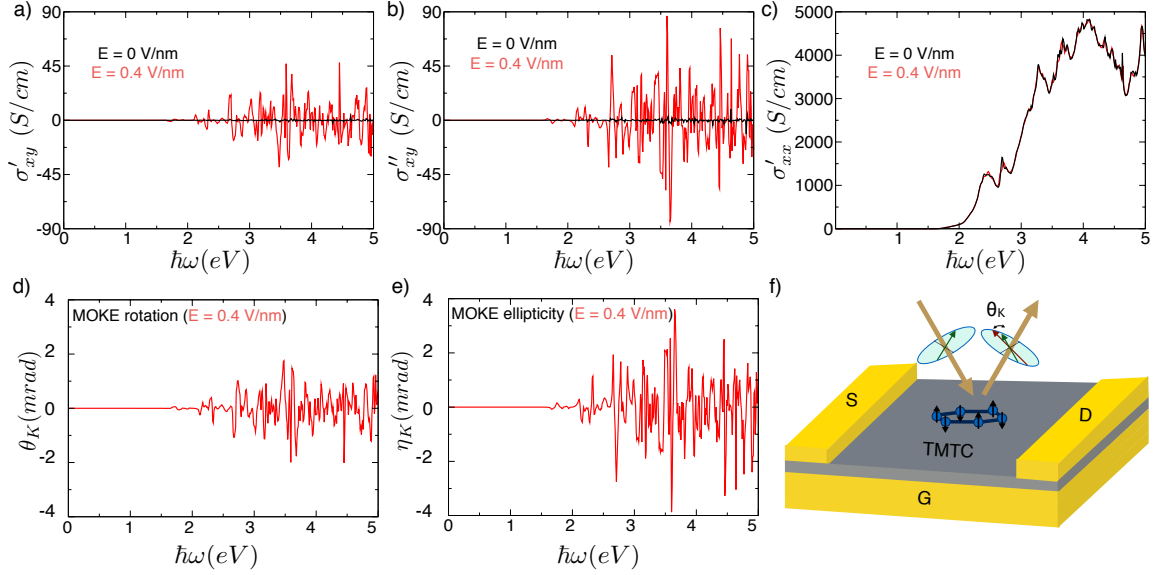


Figure 6.3: (a) The real part of  $\sigma_{xy}$ , (b) the imaginary part of  $\sigma_{xy}$ , and (c) the real part of  $\sigma_{xx}$  of bilayer MnPSe<sub>3</sub> at zero field (black) and a field with strength 0.4 V/nm (red). The smearing parameter was set to 0.2 eV. The corresponding (d) Kerr rotation angle and (e) ellipticity angle computed as a function of photon energy  $\hbar\omega$  for bilayer MnPSe<sub>3</sub> on a wedged SiO<sub>2</sub> substrate. The zero point of the energy corresponds to the top of valence band. (f) A schematic of a magneto-optic device made from layered antiferromagnets. S, D, and G stand for source, drain and gate respectively. In the incident and the reflected light, an arrow shows the direction of the polarization direction. On reflection from the antiferromagnets, the plane of polarization of light can be rotated (from green to red arrow), and an ellipticity is induced, depending on the gate voltages.

an electrostatic field to local potential [175–177]. A dipole correction was included to avoid spurious interactions between the periodically repeated images [175, 176]. The atomic structure was fixed to the relaxed case without any electric field. We find that the additional force on each atom due to the electric field compared to the relaxed structure is negligible.

After obtaining the *ab initio* wavefunctions with and without electric field from a self-consistent calculation with a regular  $16 \times 16 \times 1$  Monkhorst-Pack grid, the optical conductivity tensors were calculated utilizing the Wannier interpolation approach [178–180]. We included 256 bands at each k-point. The additional empty bands were helpful not only to localize the Wannier functions but also to calculate for a large photon energy. The maximally-localized Wannier functions were constructed from the *ab initio* wavefunctions using the Wannier90 package. We chose 176 Wannier functions per unit cell, which included all the valance *s* and *d*, *s* and *p*, and *s* and *p* orbitals for Mn, P, and Se respectively. The inner window used in the disentanglement process is from the bottom of the valence band to 5.5 eV above the Fermi level. The spread in the wannierization process was converged to  $10^{-7} \text{Å}^2$ . The optical conductivity was calculated using the Kubo formula as implemented in the Wannier90 package [181, 182]. The adjustable gaussian smearing parameter was set to 0.2 eV. We used a k-point mesh of  $240 \times 240 \times 1$  to carry out the Brillouin zone integration of the optical conductivity tensor.

### Bilayer MnPSe<sub>3</sub>

In its bulk form, MnPSe<sub>3</sub> is a layered compound with weak interlayer Van der Waals interaction. The crystal structure of MnPSe<sub>3</sub> monolayer is shown in Fig. 6.2(a). The magnetic ions (Mn) form a honeycomb lattice within each layer, and each of them is octahedrally coordinated by six Se atoms from its three neighboring (P<sub>2</sub>Se<sub>6</sub>) ligands, with the centers of the hexagons occupied by the P<sub>2</sub> groups. The Mn ions are in a half-filled *d*<sup>5</sup> state, making MnPSe<sub>3</sub> a strong antiferromagnet. We also find that the system has an easy axis along the *z*-direction, with the spins taking a Néel-type texture. The bilayer considered here is made of these monolayer units with a stacking order similar to the bulk form [see Fig. 6.2(b)]. There are two Mn atoms in each layer of the bilayer unit cell. In the top layer, while one Mn atom lies on top of an Mn atom in the bottom layer, the second Mn atom lies on top of the P atoms in bottom layer. The spins of the Mn ions from the two layers are antiferromagnetically coupled. It can be verified that bilayer MnPSe<sub>3</sub> has  $\mathcal{TI}$  symmetry, hence, no magneto-optic effect is allowed.

This  $\mathcal{TI}$  symmetry can be broken by a perpendicular electric field. We first look at the effect of such a field on the band structure of bilayer MnPSe<sub>3</sub>. Figure 6.2(c) shows the band structure in the absence of an electric field. Because of the presence of the  $\mathcal{TI}$  symmetry, the spin-up and spin-down bands are degenerate at each  $\mathbf{k}$  point, making the material magneto-optically inactive. However, upon the application of

a field (0.4 V/nm), the spin degeneracy of the bands is lifted, symptomatic of  $\mathcal{TI}$  symmetry breaking [see Fig. 6.2(d) and its insert].

Thus, on the application of a perpendicular electric field, we expect bilayer MnPSe<sub>3</sub> to become magneto-optically active. Figure 6.3(a)-(c) show the optical conductivity tensor obtained from the calculation of maximally localized Wannier functions [178–180]. We can see that  $\sigma_{xy}$  is zero when the field is zero (black curves). It becomes non-zero for a finite field (red curves), as expected. We have also verified that the reversal of the field reverses the sign of  $\sigma_{xy}$ . The longitudinal conductivity  $\sigma'_{xx}$ , on the other hand, is almost invariant under the application of a field [see Fig. 6.3(c)]. This is not surprising as  $\sigma'_{xx}$  measures the average absorption of right- and left-circularly polarized light [161].

To quantify the MOKE, we have calculated the complex polar Kerr angle. For simplicity, we assume that the incoming light is perpendicular to the surface, and the sample is placed on a wedged substrate such that there is no reflection from the substrate in the perpendicular direction. In the thin film limit the Kerr angles are given by [183, 184]

$$\theta_K + i\eta_K = \frac{2(Z_0 d \sigma_{xy})}{1 - (n_s + Z_0 d \sigma_{xx})^2}, \quad (6.5)$$

where  $\theta_K$  specifies the rotation angle of the major axis of the linearly polarized light,  $\eta_K$  specifies the ratio of the minor to the major axis of the light,  $n_s$  is the refractive index of the substrate,  $Z_0$  is the impedance of free space and  $d$  the thickness of bilayer MnPSe<sub>3</sub> (10.3 Å). The derivation is given in Appendix A.1. Figure 6.3(d) and (e) show the computed MOKE angles for a wedged SiO<sub>2</sub> substrate ( $n_s = 1.5$ ). For field strength of 0.4 V/nm,  $\theta_K$  can reach the order of a few mrad, which is well within the current detection limit [185, 186] and, in fact, comparable to conventional ferromagnets [187]. The generation of the MOKE in a magneto-optically inactive material using gate voltage is an important distinction from previous work [161].

### Monolayer MnPSe<sub>3</sub>

We have also studied the field-dependence of the MOKE in monolayer MnPSe<sub>3</sub> (see Fig. 6.4). Similar to bilayers, monolayer MnPSe<sub>3</sub> also has  $\mathcal{TI}$  symmetry. However, we find that the MOKE angle remains negligibly small in monolayers upon the application of an electric field of the same strength. This is due to the fact that in monolayer MnPSe<sub>3</sub>, the inversion symmetry breaking is realized by creating a potential difference between the top and bottom PSe<sub>3</sub> layers, which is “felt” by the Mn atom through the interaction between the Mn  $d$  orbitals and the Se  $p$  orbitals. This is a much weaker effect compared to the case of bilayers where the Mn atoms in different layers directly feel the effect of the electric field.

Our predicted gate-controllable MOKE has important implications in both fundamental research and practical applications. As the observed MOKE is very sensitive to the underlying magnetic order, it can be used to identify the magnetic ground

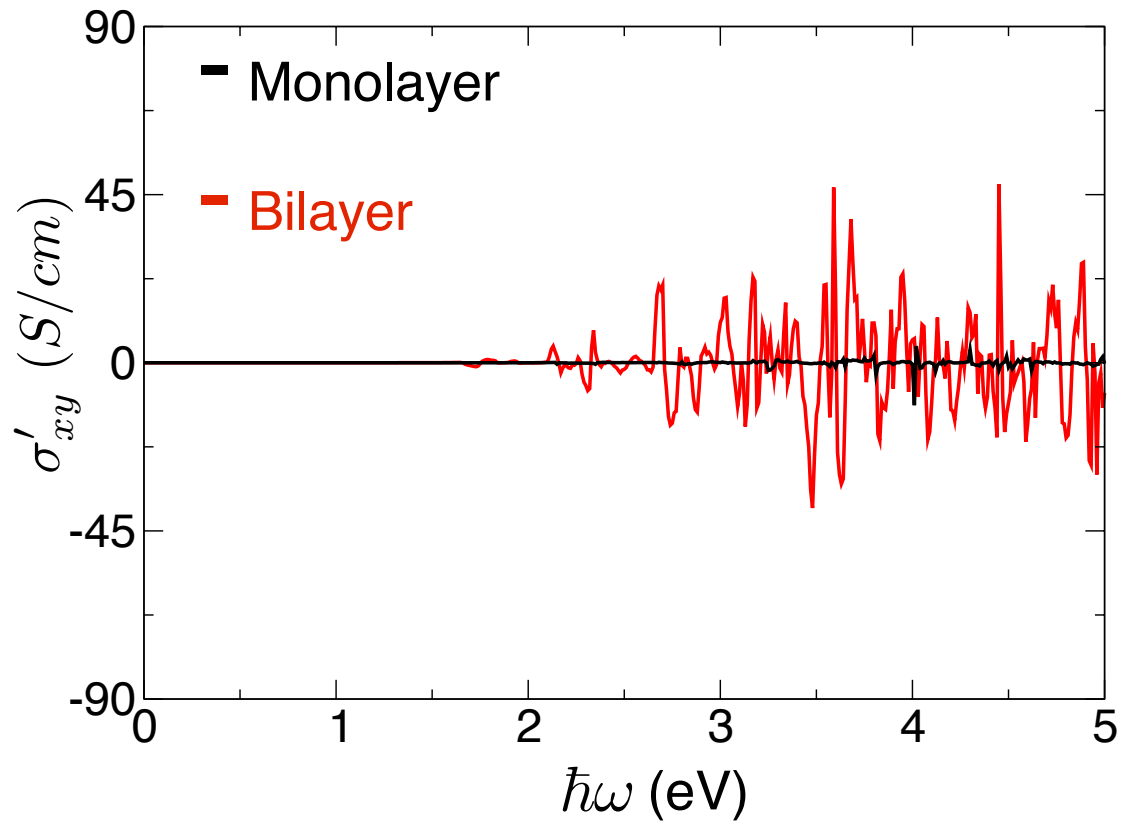


Figure 6.4:  $\sigma'_{xy}$  for monolayer (black) and bilayer (red) MnPSe<sub>3</sub> under an electric field of 0.4 V/nm. The electric field is ineffective in breaking the  $\mathcal{TI}$  symmetry for monolayer MnPSe<sub>3</sub>.

state. Not only can this method distinguish between ferromagnets and antiferromagnets, but it can be also used to distinguish among different antiferromagnetic orders, such as Néel, zigzag and stripy order on a honeycomb lattice [47], supplemented by symmetry analysis and band structure calculations. This is especially valuable for 2D materials since neutron scattering is ineffective for these materials due to the small scattering cross section. Furthermore, the sensitivity of the MOKE to the magnetic order can be exploited for magnetic information storage. For instance, the reversal of the Néel vector will result in a change of sign of the observed MOKE. Thus, the information encoded in the Néel vector can be extracted using this gate-controlled MOKE in antiferromagnets.

### 6.3 Summary

Using symmetry arguments and a tight-binding model, we show that for layered collinear antiferromagnets, magneto-optic effects can be generated and manipulated by controlling crystal symmetries through a gate voltage. This provides a promising route for electric field manipulation of the magneto-optic effects without modifying the underlying magnetic structure. We further demonstrate the gate control of magneto-optic Kerr effect (MOKE) in bilayer  $\text{MnPSe}_3$  using first-principles calculations. The field-induced inversion symmetry breaking effect leads to gate-controllable MOKE whose direction of rotation can be switched by the reversal of the gate voltage. The MOKE rotation can be as large as 4 mrad, comparable to conventional ferromagnets.

# Chapter 7

## Summary and Outlook

### 7.1 Summary

In this thesis, I have employed first-principles based calculations to study two-dimensional electronic systems. While, chapter 3 and 4 discusses 2DEG in transition metal oxides, chapter 5 and 6 discusses transition metal trichalcogenides (TMTC) as 2D magnetic material.

Our calculations on STO (111) surfaces discussed in chapter 3, investigated the origin of thickness-dependent carrier density along the polar surfaces. We also analyzed the thermodynamic stability of different stoichiometric and non-stoichiometric terminations. Our main finding is that for the Ti-terminated slabs, it is indeed possible to create a two-dimensional electron gas (2DEG). However, the carrier density of the 2DEG displays strong thickness dependence due to the competition between electronic reconstruction and polar distortions. As expected, having a surface oxygen atom at the Ti termination can stabilize the system, eliminating any electronic reconstruction, thereby making the system insulating. An analysis of the surface thermodynamic stability suggests that the Ti-terminated (111) surface should be experimentally realizable. Some of these findings were verified experimentally recently [188].

Chapter 4 discusses the origin of the mid-gap level in scanning tunneling spectroscopy experiments on STO (001) surfaces. We calculated the formation energy of charged vacancies on different terminations. By looking at the formation energies, not only did we get information regarding the stability of different vacancies, but also the transition between different vacancies represents measurable experimental features. For the SrO termination, we predict a donor level, i.e. (0/+) transition level, in approximate agreement with our experimental observations. Using configuration coordinate diagrams, we were able to further calculate the actual position of this feature. Further, for the TiO<sub>2</sub> termination we predict a donor level that is resonant with the conduction band, in agreement with prior theory and experiment, which we believe is responsible for the formation of 2DEG on TiO<sub>2</sub> terminated surfaces. By

analyzing the nature of the wavefunction, we were also able to explain the absence of certain levels in the spectrum.

Layered transition-metal trichalcogenides with the chemical formula  $ABX_3$  have attracted recent interest as potential candidates for two-dimensional magnets. In chapter 5, using first-principles calculations within density functional theory, we investigate the magnetic ground states of monolayers of Mn- and Cr-based semiconducting trichalcogenides. We show that the second and third nearest-neighbor exchange interactions ( $J_2$  and  $J_3$ ) between magnetic ions, which have been largely overlooked in previous theoretical studies, are crucial in determining the magnetic ground state. Specifically, we find that monolayer  $\text{CrSiTe}_3$  is an antiferromagnet with a zigzag spin texture due to the significant contribution from  $J_3$ , whereas  $\text{CrGeTe}_3$  is a ferromagnet with a Curie temperature of 106 K. Monolayers of Mn compounds ( $\text{MnPS}_3$  and  $\text{MnPSe}_3$ ) always show antiferromagnetic Néel order. We identify the physical origin of various exchange interactions and demonstrate that strain can be an effective knob for tuning the magnetic properties. Possible magnetic ordering in the bulk is also discussed. Our study suggests that  $ABX_3$  can be a promising platform to explore two-dimensional magnetic phenomena.

In chapter 6, using symmetry arguments and a tight-binding model, we show that for layered collinear antiferromagnets, magneto-optic effects can be generated and manipulated by controlling crystal symmetries through a gate voltage. This provides a promising route for electric field manipulation of the magneto-optic effects without modifying the underlying magnetic structure. We further demonstrate the gate control of magneto-optic Kerr effect (MOKE) in bilayer  $\text{MnPSe}_3$  using first-principles calculations. The field-induced inversion symmetry breaking effect leads to gate-controllable MOKE whose direction of rotation can be switched by the reversal of the gate voltage. The MOKE rotation can be as large as 4 mrad, comparable to conventional ferromagnets. Our predicted gate-controllable MOKE has important implications in both fundamental research and practical applications. As the observed MOKE is very sensitive to the underlying magnetic order, it can be used to identify the magnetic ground state.

## 7.2 Outlook

One of the biggest challenges we face in today's world is how to efficiently store and access information in an ever-shrinking bit area. This is a very complicated problem to tackle head-on. One approach would be to break it up into coupled, but individually tractable smaller issues. The smaller issues might have other subproblems, which upon addressing will give the necessary weapons for tackling the bigger problems. Thus, by improving each individual aspect we get closer to the collective goal.

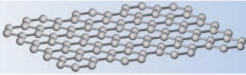
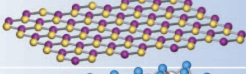
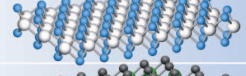
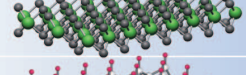
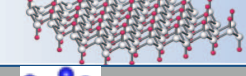
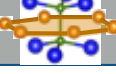
Ideally, one would like to start from a microscopic model Hamiltonian demonstrating specific properties. The end goal is to find real materials that can be successfully described by the model Hamiltonian along with the desired functionalities. Materials

by design aims at achieving this. Chapter 6 gives one illustration of how to construct model Hamiltonians with desired functionalities, and then, finding realistic materials demonstrating the effects. The challenge is to have the intuition to write down a model Hamiltonian with the desired properties, and also to be able to translate that into an algorithm for searching materials. *Ab initio* methods such as those employed in this thesis provide a good starting point for studying of material properties. Coupling it with Wannier interpolation approach [178–180] not only gives us a certain degree of intuition into the microscopic picture but also is computationally less expensive in the post-processing steps. The search step has to start with identifying the symmetries of the Hamiltonian. Here are two other examples, within the context of the thesis where this approach could prove to be effective.

The transition metal oxides bilayers and heterostructure along the (111) orientation have been a topic of immense interest, especially in the context of topological insulators [80–83]. In chapter 3, we discussed the electronic structure of the 2DEG in STO (111) surfaces.  $\text{KTaO}_3$  (KTO) is another transition metal oxide with the perovskite structure that is polar along the (111) direction. But the polarization is much stronger in KTO compared to STO. Besides, the presence of the heavier Ta atom provides these materials with very large spin-orbit coupling. The 2DEG obtained in KTO using Angle-resolved photoemission spectroscopy (ARPES), and the Fermi surface topology [189] is qualitatively different from the 2DEG obtained in STO. To fully explain the results, a Wannier function based *ab initio* approach is needed.

Another example is from 2D magnets. Since our prediction of 2D magnetism in TMTC, both experimental and theoretical interests in finding new 2D magnets have spiked. Similar to the gate-controllable magneto-optic effects introduced in chapter 6, there are a lot of other interesting possibilities brought about by 2D magnets. Similar to the idea proposed by Geim *et al.* [2] we could now use the new 2D spin lego block along with all the existing 2D crystals (Fig. 7.2). Thus, incorporating these time-reversal symmetry breaking units into other conventional 2D heterostructures could pave the way for other novel quantum mechanical phenomena. To quantify the proximity induced magnetic coupling effects accurately and to understand the nature of these interactions, the Wannier function based *ab initio* approach will prove to be vital.

Adapted from  
Geim *et al.*, Nature **499**, 419 (2013)

	Graphene	
	hBN	
	MoS <sub>2</sub>	
	WSe <sub>2</sub>	
	Fluorographene	
	2D "Spin lego"	

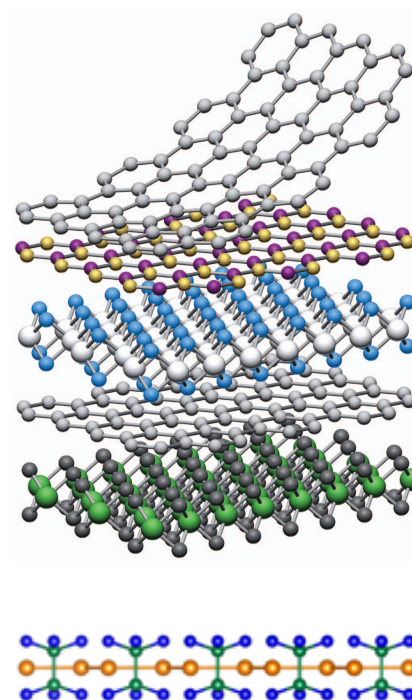


Figure 7.1: 2D lego blocks as proposed by Geim *et al.* [2], now modified to include 2D magnet lego blocks.

# Appendices

# Appendix A

## Magneto-optic effects

### A.1 Derivation of MOKE angle for 2D materials

For 2D materials, the MOKE angles can be calculated using the appropriated boundary conditions for the Maxwell's equations. Consider the setup as shown in Figure. A.1, where we have perpendicular incidence of light between air (labeled as  $I$ ), a substrate (grey, labeled as  $II$ ) with a thin sample (orange) in between. The thin film of the sample in the present case, is bilayer MnPSe<sub>3</sub>. The substrate considered here is very thick. One could also consider a wedged substrate. In either case, the reflection from the bottom of the substrate can be neglected. So, in the set up, we have an incident beam, a reflected beam and a transmitted beam with the boundary being  $z=0$ .

Let us assume that the light is monochromatic and the propagation direction is  $z$ . Thus, the incident electric field and magnetic field components of light can be written as

$$\mathbf{E}^i = E_0 \hat{\mathbf{x}} e^{i(k_I z - \omega t)}. \quad (\text{A.1})$$

Using the Maxwell's relation

$$\nabla \times \mathbf{E} = -\frac{\partial \mathbf{B}}{\partial t}, \quad (\text{A.2})$$

and the identity  $\mathbf{H} = \mathbf{B}/\mu$ , we can write

$$\mathbf{H}^i = \frac{E_0}{Z_0} \hat{\mathbf{y}} e^{i(k_I z - \omega t)}, \quad (\text{A.3})$$

where  $Z_0$  is the impedance of free space,  $\mu_0 c$  (376.6  $\Omega$ s),  $E_0$  is the amplitude of the electric field whose direction has been taken to be along the  $x$ -axis for simplicity,  $\omega$  the frequency of the light and  $k_I$  the wavenumber in medium  $I$ .

The appropriate boundary conditions describing the arrangement is:

$$\begin{aligned} \mathbf{E}^I &= \mathbf{E}^{II}, \\ \hat{\mathbf{k}} \times (\mathbf{H}^I - \mathbf{H}^{II}) &= \mathbf{J}_{free}, \end{aligned} \quad (\text{A.4})$$

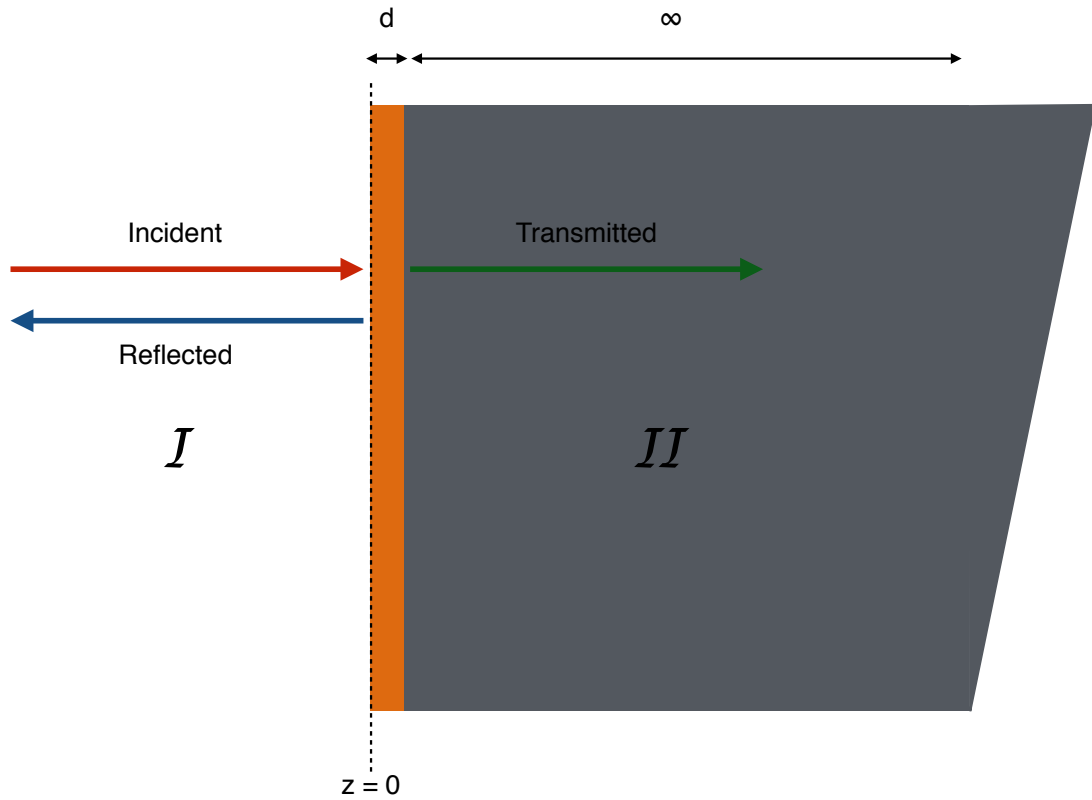


Figure A.1: A schematic of the MOKE setup. Assuming perpendicular incidence of a monochromatic light, we have an incident beam, a reflected beam and a transmitted beam. The thin sample (orange) of thickness  $d$  is kept on an infinite substrate (grey) labeled as  $II$ , which has a refractive index  $n$ . The air-sample is taken as  $z = 0$ .

where  $\mathbf{J}_{free}$  is the surface current density. The electric field component of the reflected and transmitted light can be written as,

$$\begin{aligned}\mathbf{E}^R &= E_0 R \hat{\mathbf{x}} e^{i(k_{II}z - \omega t)}, \\ \mathbf{E}^T &= E_0 T \hat{\mathbf{x}} e^{i(-k_{II}z - \omega t)},\end{aligned}\tag{A.5}$$

where  $R$  and  $T$  are reflection and transmission matrices, respectively, which has the form

$$R = \begin{pmatrix} r_{xx} & r_{xy} \\ -r_{xy} & r_{xx} \end{pmatrix}, T = \begin{pmatrix} t_{xx} & t_{xy} \\ -t_{xy} & t_{xx} \end{pmatrix}.\tag{A.6}$$

Similarly, the magnetic field component of the light can be written as,

$$\begin{aligned}\mathbf{H}^R &= \frac{E_0}{Z_0} R \hat{\mathbf{x}} e^{i(k_{II}z - \omega t)}, \\ \mathbf{H}^T &= -\frac{E_0}{Z_0} T \hat{\mathbf{x}} e^{i(-k_{II}z - \omega t)}.\end{aligned}\tag{A.7}$$

Substituting Eq. A.5 and A.7 in Eq. A.4 and using  $\mathbf{J}_{free} = \sigma \mathbf{E}^I d$  and  $k_{II} = nk_I$ , where  $n$  is the refractive index of medium  $II$ , we get,

$$\begin{aligned}1 + R &= T, \\ (1 - R - nT) &= \sigma d Z_0 (1 + R).\end{aligned}\tag{A.8}$$

For a 2D material, with higher than three-fold rotational symmetry,

$$\sigma = \begin{pmatrix} \sigma_{xx} & \sigma_{xy} \\ -\sigma_{xy} & \sigma_{xx} \end{pmatrix}.\tag{A.9}$$

Thus, Eq. A.8 can be further simplified to obtain the relations,

$$\begin{aligned}r_{xy} &= -\frac{2\sigma_{xy}Z_0d}{(1 + n + \sigma_{xx}Z_0d)^2 + \sigma_{xy}^2}, \\ r_{xx} &= \frac{1 - (n + \sigma_{xx}Z_0d)^2 - \sigma_{xy}^2}{(1 + n + \sigma_{xx}Z_0d)^2 + \sigma_{xy}^2}.\end{aligned}\tag{A.10}$$

From Eq. A.10, and using the definition of MOKE angle  $\theta_K + i\eta_K = r_{xy}/r_{xx}$  [183], we get

$$\theta_K + i\eta_K = -\frac{2\sigma_{xy}Z_0d}{1 - (n + \sigma_{xx}Z_0d)^2 - \sigma_{xy}^2}.\tag{A.11}$$

This expression matches Ref. [184], and is similar to the expression obtained with a different approach in Ref. [183], within the approximation  $\sigma_{xy} \ll \sigma_{xx}$ .

# Bibliography

- [1] K. Momma and F. Izumi. *J. Appl. Cryst.*, 44:1272, 2011.
- [2] A. K. Geim and I. V. Grigorieva. *Nature*, 499:419, 2013.
- [3] JOHN BARDEEN; BRATTAIN WALTER H. *US2524035*, 1950.
- [4] WILLIAM SHOCKLEY. *US2569347*, 1951.
- [5] A. Ohtomo and H. Y. Hwang. *Nature*, 427(6973):423, 2004.
- [6] H. Y. Hwang, Y. Iwasa, M. Kawasaki, B. Keimer, N. Nagaosa, and Y. Tokura. *Nat. Mater.*, 11:103, 2012.
- [7] S. S. A. Seo, W. S. Choi, H. N. Lee, L. Yu, K. W. Kim, C. Bernhard, and T. W. Noh. *Phys. Rev. Lett.*, 99:266801, Dec 2007.
- [8] N. Reyren, S. Thiel, A. D. Caviglia, L. Fitting Kourkoutis, G. Hammerl, C. Richter, C. W. Schneider, T. Kopp, A.-S. Rüetschi, D. Jaccard, M. Gabay, D. A. Muller, J.-M. Triscone, and J. Mannhart. *Science*, 317(5842):1196, 2007.
- [9] A. Brinkman, M. Huijben, M. van Zalk, J. Huijben, U. Zeitler, J. C. Maan, W. G. van der Wiel, G. Rijnders, D. H. A. Blank, and H. Hilgenkamp. *Nat. Mater.*, 6(7):493, 2007.
- [10] M. Ben Shalom, M. Sachs, D. Rakhmilevitch, A. Palevski, and Y. Dagan. *Phys. Rev. Lett.*, 104:126802, Mar 2010.
- [11] P. D. C. King, R. H. He, T. Eknapakul, P. Buaphet, S.-K. Mo, Y. Kaneko, S. Harashima, Y. Hikita, M. S. Bahramy, C. Bell, Z. Hussain, Y. Tokura, Z.-X. Shen, H. Y. Hwang, F. Baumberger, and W. Meevasana. *Phys. Rev. Lett.*, 108:117602, 2012.
- [12] S. Thiel, G. Hammerl, A. Schmehl, C. W. Schneider, and J. Mannhart. *Science*, 313(5795):1942, 2006.
- [13] C. Cen, S. Thiel, G. Hammerl, C. W. Schneider, K. E. Andersen, C. S. Hellberg, J. Mannhart, and J. Levy. *Nat Mater*, 7(4):298, 2008.

- [14] W. Meevasana, P. D. C. King, R. H. He, S. K. Mo, M. Hashimoto, A. Tamai, P. Songsiriritthigul, F. Baumberger, and Z. X. Shen. *Nat. Mater.*, 10(2):114, 2011.
- [15] J. Mannhart and D. G. Schlom. *Science*, 327:1607, 2010.
- [16] Elias Assmann, Peter Blaha, Robert Laskowski, Karsten Held, Satoshi Okamoto, and Giorgio Sangiovanni. *Phys. Rev. Lett.*, 110:078701, Feb 2013.
- [17] Lixin Zhang, Xiang-Feng Zhou, Hui-Tian Wang, Jing-Jun Xu, Jingbo Li, E. G. Wang, and Su-Huai Wei. *Phys. Rev. B*, 82:125412, Sep 2010.
- [18] Zhicheng Zhong, P. X. Xu, and Paul J. Kelly. *Phys. Rev. B*, 82:165127, Oct 2010.
- [19] N. C. Bristowe, P. B. Littlewood, and Emilio Artacho. *Phys. Rev. B*, 83:205405, May 2011.
- [20] P. R. Willmott, S. A. Pauli, R. Herger, C. M. Schlepütz, D. Martoccia, B. D. Patterson, B. Delley, R. Clarke, D. Kumah, C. Cionca, and Y. Yacoby. *Phys. Rev. Lett.*, 99:155502, Oct 2007.
- [21] Naoyuki Nakagawa, Harold Y. Hwang, and David A. Muller. *Nat. Mater.*, 5(3):204, 2006.
- [22] K. S. Novoselov, A. K. Geim, S. V. Morozov, D. Jiang, Y. Zhang, S. V. Dubonos, I. V. Grigorieva, and A. A. Firsov. *Science*, 306:666, 2004.
- [23] K. S. Novoselov, A. K. Geim, S. V. Morozov, D. Jiang, M. I. Katsnelson, I. V. Grigorieva, S. V. Dubonos, and A. A. Firsov. *Nature*, 438:197, 2005.
- [24] Y. Zhang, Yan-Wen Tan, Horst L. Stormer, and Philip Kim. *Nature*, 438:201, 2005.
- [25] A. K. Geim and K. S. Novoselov. *Nat. Mater.*, 6:183, 2007.
- [26] A. H. Castro Neto, F. Guinea, N. M. R. Peres, K. S. Novoselov, and A. K. Geim. *Rev. Mod. Phys.*, 81:109, 2009.
- [27] F. Schedin T. J. Booth V. V. Khotkevich S. V. Morozov K. S. Novoselov, D. Jiang and A. K. Geim. *PNAS*, 102:10451, 2005.
- [28] F. Withers, O. Del Pozo-Zamudio, A. Mishchenko, A. P. Rooney, A. Gholinia, K. Watanabe, T. Taniguchi, S. J. Haigh, A. K. Geim, A. I. Tartakovskii, and K. S. Novoselov. *Nat Mater*, 14(3):301–306, 03 2015.

- [29] Yuanbo Zhang, Tsung-Ta Tang, Caglar Girit, Zhao Hao, Michael C. Martin, Alex Zettl, Michael F. Crommie, Y. Ron Shen, and Feng Wang. *Nature*, 459 (7248):820–823, 06 2009.
- [30] Kin Fai Mak, Chun Hung Lui, Jie Shan, and Tony F. Heinz. *Phys. Rev. Lett.*, 102:256405, Jun 2009.
- [31] Sanfeng Wu, Jason S. Ross, Gui-Bin Liu, Grant Aivazian, Aaron Jones, Zaiyao Fei, Wenguang Zhu, Di Xiao, Wang Yao, David Cobden, and Xiaodong Xu. *Nat Phys*, 9(3):149–153, 03 2013.
- [32] Mengqiao Sui, Guorui Chen, Ligu Ma, Wen-Yu Shan, Dai Tian, Kenji Watanabe, Takashi Taniguchi, Xiaofeng Jin, Wang Yao, Di Xiao, and Yuanbo Zhang. *Nat Phys*, 11(12):1027–1031, 12 2015.
- [33] Y. Shimazaki, M. Yamamoto, I. V. Borzenets, K. Watanabe, T. Taniguchi, and S. Tarucha. *Nat Phys*, 11(12):1032–1036, 12 2015.
- [34] Xiaofeng Qian, Junwei Liu, Liang Fu, and Ju Li. *Science*, 346(6215):1344–1347, 2014. ISSN 0036-8075.
- [35] Wenbin Li and Ju Li. *Nat Commun*, 7:10843, 02 2016.
- [36] A. Splendiani, L. Sun, Y. Zhang, T. Li, J. Kim, C.-Y. Chim, G. Galli, and F. Wang. *Nano Lett.*, 10:1271, 2010.
- [37] Kin Fai Mak, Changgu Lee, James Hone, Jie Shan, and Tony F. Heinz. *Phys. Rev. Lett.*, 105:136805, Sep 2010.
- [38] B. Radisavljevic, A. Radenovic, J. Brivio, V. Giacometti, and A. Kis. *Nature Nanotech.*, 6:147, 2011.
- [39] Qing Hua Wang, Kouros Kalantar-Zadeh, Andras Kis, Jonathan N. Coleman, and Michael S. Strano. *Nature Nanotech.*, 7:699, 2012.
- [40] Z. Y. Zhu, Y. C. Cheng, and U. Schwingenschlögl. *Phys. Rev. B*, 84:153402, Oct 2011.
- [41] Di Xiao, Gui-Bin Liu, Wanxiang Feng, Xiaodong Xu, and Wang Yao. *Phys. Rev. Lett.*, 108:196802, May 2012.
- [42] Wanxiang Feng, Yugui Yao, Wenguang Zhu, Jinjian Zhou, Wang Yao, and Di Xiao. *Phys. Rev. B*, 86:165108, Oct 2012.
- [43] Wen-Yu Shan, Hai-Zhou Lu, and Di Xiao. *Phys. Rev. B*, 88:125301, Sep 2013.
- [44] Xiaodong Xu, Wang Yao, Di Xiao, and Tony F. Heinz. *Nat Phys*, 10:343, 2014.

- [45] N. Sivadas, H. Dixit, Valentino R. Cooper, and Di Xiao. *Phys. Rev. B*, 89:075303, Feb 2014.
- [46] Wattaka Sitaputra, Nikhil Sivadas, Marek Skowronski, Di Xiao, and Randall M. Feenstra. *Phys. Rev. B*, 91:205408, May 2015.
- [47] Nikhil Sivadas, Matthew W. Daniels, Robert H. Swendsen, Satoshi Okamoto, and Di Xiao. *Phys. Rev. B*, 91:235425, 2015.
- [48] Nikhil Sivadas, Satoshi Okamoto, and Di Xiao. *arXiv:1607.02156*, 2016.
- [49] R. Martin. Cambridge University Press, 2004.
- [50] Gabriele Giuliani and Giovanni Vignale. Cambridge University Press, 2005.
- [51] M. Born and J. R. Oppenheimer. *Ann. Phys.*, 84(4):457–484, 1927.
- [52] P. Hohenberg and W. Kohn. *Phys. Rev.*, 136:B864–B871, Nov 1964.
- [53] W. Kohn. North Holland, NY, 1985.
- [54] W. Kohn and L. J. Sham. *Phys. Rev.*, 140:A1133–A1138, 1965.
- [55] Michael P. Marder. Wiley, 2000.
- [56] D. M. Ceperley and B. J. Alder. *Phys. Rev. Lett.*, 45:566–569, Aug 1980.
- [57] J. P. Perdew and A. Zunger. *Phys. Rev. B*, 23:5048–5079, 1981.
- [58] John P. Perdew and Yue Wang. *Phys. Rev. B*, 33(12):8800, Jun 1986.
- [59] J. P. Perdew and Y. Wang. *Phys. Rev. B*, 45(23):13244–13249, 1992.
- [60] G. Kresse and J. Furthmüller. *Phys. Rev. B*, 54:11169, 1996.
- [61] Paolo Giannozzi, Stefano Baroni<sup>1</sup>, Nicola Bonini, Matteo Calandra, Roberto Car, Carlo Cavazzoni, Davide Ceresoli, Guido L Chiarotti, Matteo Cococcioni, Ismaila Dabo, Andrea Dal Corso, Stefano de Gironcoli, Stefano Fabris, Guido Fratesi, Ralph Gebauer, Uwe Gerstmann, Christos Gougoussis, Anton Kokalj, Michele Lazzeri, Layla Martin-Samos, Nicola Marzari, Francesco Mauri, Riccardo Mazzarello, Stefano Paolini, Alfredo Pasquarello, Lorenzo Paulatto, Carlo Sbraccia, Sandro Scandolo, Gabriele Sclauzero, Ari P Seitsonen, Alexander Smogunov, Paolo Umari, and Renata M Wentzcovitch. *J. Phys.: Cond. Matt.*, 21(39):395502, 2009.
- [62] Wolter Siemons, Gertjan Koster, Hideki Yamamoto, Walter A. Harrison, Gerald Lucovsky, Theodore H. Geballe, Dave H. A. Blank, and Malcolm R. Beasley. *Phys. Rev. Lett.*, 98:196802, May 2007.

- [63] Rossitza Pentcheva and Warren E. Pickett. *Phys. Rev. Lett.*, 102(10):107602, Mar 2009.
- [64] N. C. Bristowe, Emilio Artacho, and P. B. Littlewood. *Phys. Rev. B*, 80(4):045425, Jul 2009.
- [65] Massimiliano Stengel and David Vanderbilt. *Phys. Rev. B*, 80(24):241103, Dec 2009.
- [66] N. C. Bristowe, P. B. Littlewood, and Emilio Artacho. *Journal of Physics: Condensed Matter*, 23(8):081001, Feb 2011.
- [67] Massimiliano Stengel. *Phys. Rev. B*, 84(20):205432, Nov 2011.
- [68] Satoshi Okamoto and Andrew J. Millis. *Nature*, 428(6983):630, 2004.
- [69] D. R. Hamann, D. A. Muller, and H. Y. Hwang. *Phys. Rev. B*, 73:195403, May 2006.
- [70] Satoshi Okamoto, Andrew J. Millis, and Nicola A. Spaldin. *Phys. Rev. Lett.*, 97:056802, Jul 2006.
- [71] V. R. Cooper. *Phys. Rev. B*, 85:235109, 2012.
- [72] M. Takizawa, S. Tsuda, T. Susaki, H. Y. Hwang, and A. Fujimori. *Phys. Rev. B*, 84:245124, Dec 2011.
- [73] Claudia Cantoni, Jaume Gazquez, Fabio Miletto Granozio, Mark P. Oxley, Maria Varela, Andrew R. Lupini, Stephen J. Pennycook, Carmela Aruta, Umberto Scotti di Uccio, Paolo Perna, and Davide Maccariello. *Adv. Mater.*, 24(29):3952, AUG 2 2012.
- [74] Yong Wang, Manish K. Niranjana, S. S. Jaswal, and Evgeny Y. Tsymbal. *Phys. Rev. B*, 80:165130, Oct 2009.
- [75] Massimiliano Stengel. *Phys. Rev. B*, 106(13):136803, Dec 2011.
- [76] A. Biswas, P. B. Rossen, C.-H. Yang, W. Siemons, M.-H. Jung, I. K. Yang, R. Ramesh, and Y. H. Jeong. *Appl. Phys. Lett.*, 98(5):051904, 2011.
- [77] G. Herranz, F. Sánchez, N. Dix, M. Scigaj, and J. Fontcuberta. *Sci. Rep.*, 2:758, 2012.
- [78] A. Annadi, Q. Zhang, X. Renshaw Wang, N. Tuzla, K. Gopinadhan, W. M. Lü, A. Roy Barman, Z. Q. Liu, A. Srivastava, S. Saha, Y. L. Zhao, S. W. Zeng, S. Dhar, E. Olsson, B. Gu, S. Yunoki, S. Maekawa, H. Hilgenkamp, T. Venkatesan, and Ariando. *Nat. Commun.*, 4:1838, 2013.

- [79] M. Rzchowski and C.-B. Eom (private communications).
- [80] Di Xiao, Wenguang Zhu, Ying Ran, Naoto Nagaosa, and Satoshi Okamoto. *Nat. Commun.*, 2:596, 2011.
- [81] Kai-Yu Yang, Wenguang Zhu, Di Xiao, Satoshi Okamoto, Ziqiang Wang, and Ying Ran. *Phys. Rev. B*, 84:201104, Nov 2011.
- [82] Andreas Rüegg and Gregory A. Fiete. *Phys. Rev. B*, 84:201103, 2011.
- [83] Satoshi Okamoto. *Phys. Rev. Lett.*, 110:066403, 2013.
- [84] David Vanderbilt. *Phys. Rev. B*, 41:7892–7895, Apr 1990.
- [85] V. I. Anisimov, J. Zaanen, and O. K. Andersen. *Phys. Rev. B*, 44(3):943, 1991.
- [86] L. Bengtsson. *Phys. Rev. B*, 59:12301–4, 1999.
- [87] B. Meyer and D. Vanderbilt. *Phys. Rev. B*, 63:205426 1–10, 2001.
- [88] F. Bottin, Fabio Finocchi, and Claudine Noguera. *Phys. Rev. B*, 68:035418, Jul 2003.
- [89] A Pojani, F Finocchi, and C Noguera. *Appl. Surf. Sc.*, 142:177, 1999.
- [90] Ariana Pojani, Fabio Finocchi, and Claudine Noguera. *Surf. Sci.*, 442(2):179, 1999.
- [91] R. I. Eglitis. In Y. N. Shunin and A. E. Kiv, editors, *Nanodevices and Nanomaterials for Ecological Security*, page 125. Springer Science+Business Media, Dordrecht, 2012.
- [92] A. F. Santander-Syro, O. Copie, T. Kondo, F. Fortuna, S. Pailhes, R. Weht, X. G. Qiu, F. Bertran, A. Nicolaou, A. Taleb-Ibrahimi, P. Le Fevre, G. Herranz, M. Bibes, N. Reyren, Y. Apertet, P. Lecoeur, A. Barthelemy, and M. J. Rozenberg. *Nature*, 469(7329):189, 2011.
- [93] R. Di Capua, M. Radovic, G. M. De Luca, I. Maggio-Aprile, F. Miletto Granozio, N. C. Plumb, Z. Ristic, U. Scotti di Uccio, R. Vaglio, and M. Salluzzo. *Phys. Rev. B*, 86:155425, Oct 2012.
- [94] Y Aiura, I Hase, H Bando, T Yasue, T Saitoh, and D.S Dessau. *Surface Science*, 515(1):61 – 74, 2002. ISSN 0039-6028.
- [95] Y. Haruyama, S. Kodaira, Y. Aiura, H. Bando, Y. Nishihara, T. Maruyama, Y. Sakisaka, and H. Kato. *Phys. Rev. B*, 53:8032–8035, Mar 1996.

- [96] Richard C. Hatch, Kurt D. Fredrickson, Miri Choi, Chungwei Lin, Hosung Seo, Agham B. Posadas, and Alexander A. Demkov. *Journal of Applied Physics*, 114(10):103710, 2013.
- [97] Chungwei Lin and Alexander A. Demkov. *Phys. Rev. Lett.*, 111:217601, Nov 2013.
- [98] R. Courths, B. Cord, and H. Saalfeld. *Solid State Communications*, 70(11):1047 – 1051, 1989. ISSN 0038-1098.
- [99] P. Mårtensson and R. M. Feenstra. *Phys. Rev. B*, 39:7744–7753, Apr 1989.
- [100] R. M. Feenstra. *Phys. Rev. B*, 50:4561–4570, Aug 1994.
- [101] Anderson Janotti, Joel B. Varley, Minseok Choi, and Chris G. Van de Walle. *Phys. Rev. B*, 90:085202, Aug 2014.
- [102] Meng-Qiu Cai, Yong-Jun Zhang, Guo-Wei Yang, Zhen Yin, Ming-Sheng Zhang, Wang-Yu Hu, and Yan-Guo Wang. *The Journal of Chemical Physics*, 124(17): 174701, 2006.
- [103] E. A. Kotomin, V. Alexandrov, D. Gryaznov, R. A. Evarestov, and J. Maier. *Phys. Chem. Chem. Phys.*, 13:923–926, 2011.
- [104] Yu.F. Zhukovskii, E.A. Kotomin, S. Piskunov, and D.E. Ellis. *Solid State Communications*, 149(33–34):1359 – 1362, 2009. ISSN 0038-1098.
- [105] Yuri F. Zhukovskii, Eugene A. Kotomin, Robert A. Evarestov, and Donald E. Ellis. *International Journal of Quantum Chemistry*, 107(14):2956–2985, 2007. ISSN 1097-461X.
- [106] Paolo Giannozzi, Stefano Baroni, Nicola Bonini, Matteo Calandra, Roberto Car, Carlo Cavazzoni, Davide Ceresoli, Guido L Chiarotti, Matteo Cococcioni, Ismaila Dabo, Andrea Dal Corso, Stefano de Gironcoli, Stefano Fabris, Guido Fratesi, Ralph Gebauer, Uwe Gerstmann, Christos Gougoussis, Anton Kokalj, Michele Lazzeri, Layla Martin-Samos, Nicola Marzari, Francesco Mauri, Riccardo Mazzarello, Stefano Paolini, Alfredo Pasquarello, Lorenzo Paulatto, Carlo Sbraccia, Sandro Scandolo, Gabriele Sclauzero, Ari P Seitsonen, Alexander Smogunov, Paolo Umari, and Renata M Wentzcovitch. *Journal of Physics: Condensed Matter*, 21(39):395502, 2009.
- [107] N. Pavlenko, T. Kopp, and J. Mannhart. *Phys. Rev. B*, 88:201104, Nov 2013.
- [108] T. Saitoh, A. E. Bocquet, T. Mizokawa, and A. Fujimori. *Phys. Rev. B*, 52: 7934–7938, Sep 1995.

- [109] Do Duc Cuong, Bora Lee, Kyeong Mi Choi, Hyo-Shin Ahn, Seungwu Han, and Jaichan Lee. *Phys. Rev. Lett.*, 98:115503, Mar 2007.
- [110] Anderson Janotti and Chris G. Van de Walle. *Phys. Rev. B*, 76:165202, Oct 2007.
- [111] C. G. Van de Walle and J. Neugebauer. *J. Appl. Phys.*, 95:3851, 2004.
- [112] G. Markov and M. C. Payne. *Phys. Rev. B*, 51:4014, 1995.
- [113] Stephan Lany and Alex Zunger. *Phys. Rev. B*, 78:235104, 2008.
- [114] Su-Huai Wei and S. B. Zhang. *Phys. Rev. B*, 66:155211, 2002.
- [115] Hannu-Pekka Komsa and Alfredo Pasquarello. *Phys. Rev. Lett.*, 110:095505, 2013.
- [116] Clas Persson, Yu-Jun Zhao, Stephan Lany, and Alex Zunger. *Phys. Rev. B*, 72:035211, Jul 2005.
- [117] Stephan Lany and Alex Zunger. *Phys. Rev. B*, 72:035215, Jul 2005.
- [118] Anderson Janotti and Chris G. Van de Walle. *Applied Physics Letters*, 87(12):122102, 2005.
- [119] Ph. Ebert, L. Ivanova, and H. Eisele. *Phys. Rev. B*, 80:085316, Aug 2009.
- [120] R. M. Feenstra and P. Mårtensson. *Phys. Rev. Lett.*, 61:447–450, Jul 1988.
- [121] Maria Grazia Betti, V. Corradini, G. Bertoni, P. Casarini, Carlo Mariani, and A. Abramo. *Phys. Rev. B*, 63:155315, Mar 2001.
- [122] P. D. C. King, T. D. Veal, D. J. Payne, A. Bourlange, R. G. Egdell, and C. F. McConville. *Phys. Rev. Lett.*, 101:116808, Sep 2008.
- [123] M. Noguchi, K. Hirakawa, and T. Ikoma. *Phys. Rev. Lett.*, 66:2243–2246, Apr 1991.
- [124] I. Mahboob, T. D. Veal, C. F. McConville, H. Lu, and W. J. Schaff. *Phys. Rev. Lett.*, 92:036804, Jan 2004.
- [125] D. C. Tsui. *Phys. Rev. Lett.*, 24:303–306, Feb 1970.
- [126] D. C. Tsui. *Phys. Rev. B*, 4:4438–4449, Dec 1971.
- [127] T. D. Veal, L. F. J. Piper, M. R. Phillips, M. H. Zareie, Hai Lu, W. J. Schaff, and C. F. McConville. *physica status solidi (a)*, 204(2):536–542, 2007. ISSN 1862-6319.

- [128] Audrius Alkauskas, John L. Lyons, Daniel Steiauf, and Chris G. Van de Walle. *Phys. Rev. Lett.*, 109:267401, Dec 2012.
- [129] Jun Zhang, S. Walsh, C. Brooks, D. G. Schlom, and L. J. Brillson. *J. Vac. Sci. Technol. B*, 26(4):1466, 2008.
- [130] Ashwin Ramasubramaniam and Doron Naveh. *Phys. Rev. B*, 87:195201, May 2013.
- [131] M. A. H. Vozmediano, M. P. López-Sancho, T. Stauber, and F. Guinea. *Phys. Rev. B*, 72:155121, Oct 2005.
- [132] A. R. Wildes, B. Roessli, B. Lebech, and K. W. Godfrey. *J. Phys.: Condens. Matter*, 10:6417, 1998.
- [133] A. Wiedenmann, J. Rossat-Mignod, A. Louisy, R. Brec, and J. Rouxel. *Solid State Commun.*, 40:1067, 1981.
- [134] R. Brec. *Solid State Ionics*, 22:3, 1986.
- [135] P. A. Joy and S. Vasudevan. *Phys. Rev. B*, 46:5425–5433, Sep 1992.
- [136] Y Takano, N Arai, A Arai, Y Takahashi, K Takase, and K Sekizawa. *J. of Mag. and Mag. Mater.*, 272:E593, 2004.
- [137] B. Siberchicot, S. Jobic, V. Carteaux, P. Gressier, and G. Ouvrard. *J. Phys. Chem.*, 100:5863, 1996.
- [138] A. R. Wildes, K. C. Rule, R. I. Bewley, M. Enderle, and T. J. Hicks. *J. Phys.: Condens. Matter*, 24:416004, 2012.
- [139] P. Jeevanandam and S. Vasudevan. *J. Phys.: Condens. Matter*, 11:3563, 1999.
- [140] Xiao Li, Ting Cao, Qian Niu, Junren Shi, and Ji Feng. *Proc. Natl. Acad. Sci.*, 110:3738, 2013.
- [141] V. Carteaux, F. Moussa, and M. Spiesser. *Europhys. Lett.*, 29:251, 1995.
- [142] L. Casto, A. Clune, M. Yokosuk, J. Musfeldt, T. Williams, H. L. Zhuang, M. W. Lin, K. Xiao, R. G. Hennig, B. Sales, J. Yan, and D. Mandrus. *APL Materials*, page in print, 2015.
- [143] V. Carteaux, D. Brunet, G. Ouvrard, and G. Andre. *J. Phys.: Condens. Matter*, 7:69, 1995.
- [144] Xingxing Li and Jinlong Yang. *J. Mater. Chem. C.*, 2:7071, 2014.
- [145] Xiaofang Chen, Jingshan Qi, and Daning Shi. *Phys. Lett. A*, 379:60, 2015.

- [146] Xingxing Li, Xiaojun Wu, and Jinlong Yang. *J. Am. Chem. Soc.*, 136:11065, 2014.
- [147] P. E. Blöchl. *Phys. Rev. B*, 50:17953–17979, Dec 1994.
- [148] G. Kresse and D. Joubert. *Phys. Rev. B*, 59:1758–1775, 1999.
- [149] John P. Perdew, Kieron Burke, and Matthias Ernzerhof. *Phys. Rev. Lett.*, 77:3865, 1996.
- [150] John P. Perdew, Kieron Burke, and Matthias Ernzerhof. *Phys. Rev. Lett.*, 78:1396–1396, Feb 1997.
- [151] Lei Wang, Thomas Maxisch, and Gerbrand Ceder. *Phys. Rev. B*, 73:195107, May 2006.
- [152] C. Franchini, R. Podloucky, J. Paier, M. Marsman, and G. Kresse. *Phys. Rev. B*, 75:195128, May 2007.
- [153] S. L. Dudarev, G. A. Botton, S. Y. Savrasov, C. J. Humphreys, and A. P. Sutton. *Phys. Rev. B*, 57:1505–1509, Jan 1998.
- [154] *Using  $J_1$ ,  $J_2$ , and  $J_3$  hopping energies determined from DFT, we conducted a Monte Carlo simulation of an Ising model on the 2D honeycomb lattice with periodic boundary conditions. The calculations proceeded according to the standard Metropolis algorithm. The system was annealed from a uniformly random spin distribution at 400K down to absolute zero in half Kelvin steps. Size effects were accounted for by repeating trials on systems from 16 atomic sites up to 256 atomic sites. Textbook histogram methods were then used to determine the critical temperature of the various parameterizations listed in Table I.*
- [155] A. Ushakov, D. Kukusta, A. Yaresko, and D. Khomskii. *Phys. Rev. B*, 87:014418, Jan 2013.
- [156] J. B. Goodenough. *Phys. Rev.*, 100:564, 1955.
- [157] J. B. Goodenough. *J. Phys. Chem. Solids.*, 6:287, 1958.
- [158] V. V. Mazurenko, S. L. Skornyakov, A. V. Kozhevnikov, F. Mila, and V. I. Anisimov. *Phys. Rev. B.*, 75:224408, 2007.
- [159] Hyun-Joo Koo, Hongjun Xiang, Changhoon Lee, and Myung-Hwan Whangbo. *Inorganic Chemistry*, 48(19):9051–9053, 2009. PMID: 19719142.
- [160] Houria Kabbour, Rénaud David, Alain Pautrat, Hyun-Joo Koo, Myung-Hwan Whangbo, Gilles André, and Olivier Mentré. *Angewandte Chemie*, 124(47):11915–11919, 2012. ISSN 1521-3757.

- [161] Wanxiang Feng, Guang-Yu Guo, Jian Zhou, Yugui Yao, and Qian Niu. *Phys. Rev. B*, 92:144426, Oct 2015.
- [162] Hua Chen, Qian Niu, and A. H. MacDonald. *Phys. Rev. Lett.*, 112:017205, 2014.
- [163] J. Kübler and C. Felser. *EPL (Europhysics Letters)*, 108:67001, 2014.
- [164] T. Jungwirth, X. Marti, P. Wadley, and J. Wunderlich. *Nature Nanotech.*, 11: 231–241, 2016.
- [165] L. D. Casto, A. J. Clune, M. O. Yokosuk, J. L. Musfeldt, T. J. Williams, H. L. Zhuang, M.-W. Lin, K. Xiao, R. G. Hennig, B. C. Sales, J.-Q. Yan, and D. Mandrus. *APL Mater.*, 3(4):041515, 2015.
- [166] T. J. Williams, A. A. Aczel, M. D. Lumsden, S. E. Nagler, M. B. Stone, J.-Q. Yan, and D. Mandrus. *Phys. Rev. B*, 92:144404, Oct 2015.
- [167] Michael A. McGuire, Hemant Dixit, Valentino R. Cooper, and Brian C. Sales. *Chem. Mater.*, 27:612, 2015.
- [168] Ming-Wei Lin, Houlong L. Zhuang, Jiaqiang Yan, Thomas Zac Ward, Alexander A. Puretzky, Christopher M. Rouleau, Zheng Gai, Liangbo Liang, Vincent Meunier, Bobby G. Sumpter, and et al. *J. Mater. Chem. C*, 4:315–322, 2016.
- [169] V V Eremenko, N F Kharchenko, Yu G Litvinenko, and V M Naumenko. Springer-Verlag, New York, 1992.
- [170] Stephan Rachel and Karyn Le Hur. *Phys. Rev. B*, 82:075106, 2010.
- [171] M. Hohenadler, T. C. Lang, and F. F. Assaad. *Phys. Rev. Lett*, 106:100403, 2011.
- [172] C. L. Kane and E. J. Mele. *Phys. Rev. Lett.*, 95:146802, 2005.
- [173] Yugui Yao, Leonard Kleinman, A. H. MacDonald, Jairo Sinova, T. Jungwirth, Ding-sheng Wang, Enge Wang, and Qian Niu. *Phys. Rev. Lett.*, 92:037204, 2004.
- [174] H Ebert. *Reports on Progress in Physics*, 59(12):1665, 1996.
- [175] J. Neugebauer and M. Scheffler. *Phys. Rev. B*, 46:16067–16084, 1992.
- [176] G. Makov and M. C. Payne. *Phys. Rev. B*, 51:4014–4022, 1995.
- [177] Peter J. Feibelman. *Phys. Rev. B*, 64:125403, Sep 2001.

- [178] Arash Mostofi, Jonathan Yates, Lee Young-See, Ivo Souza, David Vanderbilt, and Nicola Marzari. *Comp. Phys. Commun.*, 178:685, 2008.
- [179] Nicola Marzari and David Vanderbilt. *Phys. Rev. B*, 56:12847–12865, Nov 1997.
- [180] Ivo Souza, Nicola Marzari, and David Vanderbilt. *Phys. Rev. B.*, 65:035109, 2001.
- [181] Xinjie Wang, Jonathan R. Yates, Ivo Souza, and David Vanderbilt. *Phys. Rev. B*, 74:195118, Nov 2006.
- [182] Jonathan R. Yates, Xinjie Wang, David Vanderbilt, and Ivo Souza. *Phys. Rev. B*, 75:195121, May 2007.
- [183] M.-H. Kim, G. Acbas, M.-H. Yang, I. Ohkubo, H. Christen, D. Mandrus, M. A. Scarpulla, O. D. Dubon, Z. Schlesinger, P. Khalifah, and J. Cerne. *Phys. Rev. B*, 75:214416, Jun 2007.
- [184] R. Valdés Aguilar, A. V. Stier, W. Liu, L. S. Bilbro, D. K. George, N. Bansal, L. Wu, J. Cerne, A. G. Markelz, S. Oh, and N. P. Armitage. *Phys. Rev. Lett.*, 108:087403, Feb 2012.
- [185] Y. K. Kato, R. C. Myers, A. C. Gossard, and D. D. Awschalom. *Science*, 306 (5703):1910–1913, 12 2004.
- [186] Jieun Lee, Kin Fai Mak, and Jie Shan. *Nat Nano*, 11(5):421–425, 05 2016.
- [187] K. Shinagawa. volume 128 of *Springer Series in Solid-State Sciences*. Springer Berlin Heidelberg, 2000.
- [188] S. McKeown Walker, A. de la Torre, F. Y. Bruno, A. Tamai, T. K. Kim, M. Hoesch, M. Shi, M. S. Bahramy, P. D. C. King, and F. Baumberger. *Phys. Rev. Lett.*, 113:177601, Oct 2014.
- [189] F. Y. Bruno. *Private communications*.